POLITECNICO
MILANO 1863

SCUOLA DI INGEGNERIA INDUSTRIALE
E DELL'INFORMAZIONE

Numerical Investigation of the Aerodynamic Interactions between a Tip-Mounted Propeller and a Wing with deflected Flap using the Mid-Fidelity Solver DUST

Tesi di Laurea Magistrale in
Aeronautical Engineering - Ingegneria Aeronautica

Author: **Claudio Niro**

Student ID: 971100
Advisor: Prof. Alex Zanotti
Co-advisors: Ing. Alessandro Cocco, Ing. Alberto Savino
Academic Year: 2021-22

Alla mia famiglia

Abstract

Electric Vertical Takeoff and Landing (eVTOL) aircraft have great potential to revolutionize urban and regional air mobility. However, due to the complex aerodynamic interactions introduced by multi-rotor and multi-wing architectures, it can be challenging to simulate and predict their performance accurately. To address this challenge, mid-fidelity tools have emerged as an optimal trade-off between computational cost and desired accuracy, particularly in the early stages of design. *The objective of this research is to investigate the capability of a vortex particle-based mid-fidelity code, specifically the DUST solver developed at Politecnico di Milano, in capturing the aerodynamic interaction and flowfield between a wingtip-mounted propeller and a wing with a* 25% *chord flap and a nacelle, in the context of a maneuver scenario.* The wing and propeller model considered in this work was widely investigated in literature, both by experiments and high-fidelity CFD simulations, and represents a perfect benchmark case for this kind of aerodynamic study of tiltrotors and electrical distributed propulsion aircraft configurations. The present numerical activity showed the capabilities of mid-fidelity aerodynamic solver, such as DUST, to capture the aerodynamic interactional effects of the installed propeller on the wing by a direct comparison of wing pressure coefficient distributions, propeller airloads and flowfield with both experimental data and high-fidelity CFD simulations. Analyses on the upstream and downstream effects on the propeller and wing performance showed that the benefits arising from the installation of a wingtip-mounted propeller can be correctly predicted. The analyses showed that this configuration results in a significant lift and propeller performance enhancement, which was accurately captured by the DUST solver. Overall the DUST model reduced the computational effort while maintaining accuracy, with no significant errors or discrepancies introduced. The validation campaign conducted demonstrates good agreement in both the prediction of the time-dependent solutions and the time-averaged (integral) quantities, with only a slight overestimation observed for propeller thrust and a slight underestimation of the system lift coefficient.

Keywords: Mid-fidelity, Tiltrotor, Rotor-wing interaction, DUST

Abstract in lingua italiana

I velivoli elettrici a decollo e atterraggio verticale (eVTOL) hanno un grande potenziale e sono destinati a rivoluzionare la mobilità aerea urbana e a breve raggio. Tuttavia, a causa delle complesse interazioni aerodinamiche introdotte dalle architetture multi rotore e multi ala, risulta difficile simulare e prevedere con precisione le loro prestazioni. Per affrontare questa criticità, recentemente sono emersi numerosi metodi Mid-Fidelity, un compromesso ottimale tra costo computazionale e accuratezza desiderata, in particolare nelle prime fasi di progettazione. *L'obiettivo di questa tesi è studiare la capacità del codice Mid-Fidelity a particelle vorticose sviluppato al Politecnico di Milano: DUST, di catturare l'interazione aerodinamica e il campo di flusso tra un'elica montata all'estremità di un'ala con un flap al* 25% *della corda e una gondola motore, nel contesto di uno scenario di manovra.* I modelli di ala ed elica considerati in questo lavoro sono stati ampiamente studiati in letteratura, sia con esperimenti sia con simulazioni CFD e rappresentano un perfetto modello di riferimento per questa tipologia di studio aerodinamico. La presente attività numerica ha dimostrato le capacità di solutori aerodinamici Mid-Fidelity, come DUST, di catturare gli effetti aerodinamici di interazione tra l'elica installata sull'ala e l'ala stessa, attraverso un confronto diretto delle distribuzioni di pressione, dei carichi dell'elica e del campo di flusso con i dati sperimentali e simulazioni CFD. L'analisi degli effetti del flusso non uniforme sulle prestazioni dell'elica e dell'ala ha dimostrato che è possibile prevedere correttamente i benefici derivanti dall'installazione di un motore ad elica all'estremità alare. L'analisi ha evidenziato come questa configurazione comporti un significativo aumento della portanza e delle prestazioni dell'elica. Il modello DUST ha ridotto lo sforzo computazionale mantenendo una buona accuratezza, non sono stati introdotti errori o difformità significative. La validazione condotta dimostra un buon accordo sia nella predizione delle quantità tempo-dipendenti sia in quelle mediate nel tempo (integrali), presenta solo una lieve sovrastima per la spinta dell'elica e una leggera sottostima della portanza totale dovuta alle limitazioni modellistiche di DUST per la gondola motore.

Parole chiave: Mid-fidelity, Convertilano, Interazione rotore-ala, DUST

Contents

1 | Introduction

Tiltrotors are a type of aircraft that has been developed to address the limitations of traditional helicopters, specifically their slow speed and limited range. These aircraft are designed to combine the vertical takeoff and landing capabilities of a helicopter with the speed and range of a fixed-wing aircraft, making them an ideal choice for a variety of missions.

Unlike traditional helicopters, tiltrotors have rotors that are oriented so that the plane of rotation is horizontal, providing lift in the same manner as a typical helicopter rotor. However, as the aircraft acquires speed, the rotors gradually tilt forward until the plane of rotation becomes vertical. In this way, the rotors act as a propeller, while the airfoil of the fixed wing provides lift, allowing the aircraft to fly like a conventional airplane.

Tiltrotors offer a number of advantages over traditional helicopters, including their ability to take off and land vertically in confined spaces and remote locations. They are also capable of flying at high speeds over long distances, making them ideal for a wide range of missions. However, they are complex aircraft with a large number of moving parts, which can make them expensive to operate and maintain. Additionally, they may be limited in their ability to hover in high-altitude and high-temperature environments, which can impact their effectiveness in certain missions.

Overall, tiltrotors represent a promising technology that has the potential to revolutionize aviation in a number of ways. As further research and development is conducted, it is likely that these aircraft will become increasingly versatile and efficient, opening up new possibilities for military, commercial, and civil use.

1.1. Historical background

Tiltrotors have been in development since the late 1940s, but it wasn't until the 1980s that the first successful tiltrotor flew: the V-22 Osprey, a multiservice, multimission tilt rotor aircraft suitable for military missions and commercial roles. It is the culmination of over 30 years of prototype and technology development which ranged from the Bell XV-3 tilt

rotor and the Boeing Vertol VZ-2 tilt wing of the 1950's to the successful demonstration of an advanced, mature tiltrotor technology embodied by the Bell XV-15 starting in the late 1970s [33]

In 1951, the US Army and US Air Force jointly initiated a program to develop new Vertical Takeoff and Landing (VTOL) aircraft, which resulted in a Request for Proposal for convertible aircraft. Bell Aircraft Corporation responded with its Model 200 tilt-rotor, later designated as XV-3, after extensive research and development led by Larry Bell and Robert Lichten.

The XV-3 underwent extensive ground testing before its initial hover trial in August 1955. While the aircraft showed satisfactory characteristics during the beginning of the flight, high vibrations in hover due to dynamic instability of the proprotor-pylon assembly were observed in subsequent test flights. In October 1956, a nearly fatal crash occurred, prompting Bell engineers to ground the XV-3 and conduct research activities and tiedown tests to solve and better understand the problem.

Figure 1.1: Bell XV-3. [22]

At the time, analysis capabilities were limited, and dynamicists had to rely mainly on physical testing to understand the causes of the dynamic instability. Despite these setbacks, the XV-3 program continued, and the aircraft ultimately achieved full tilt rotor conversion in December 1958, demonstrating the fundamental feasibility of the tilt-rotor concept. However, evaluations at Bell and military facilities revealed that the aircraft was underpowered and had poor performance in both hover and higher speeds. Handling qualities and structural stability were also deficient.

Despite these shortcomings, the XV-3 represented a significant achievement at the time, as it demonstrated the feasibility of the tilt-rotor concept and its ability to safely perform in-flight conversion between airplane and helicopter modes. This paved the way for further development of tilt-rotor aircraft. [22].

While interest in tilt-wing aircraft was apparently lost, the achievements of the XV-3 program had succeeded in convincing the aeronautical world of tilt-rotors unique potential.

After conducting extensive development in the 1960s, Bell initiated the preliminary design of a tiltrotor, the model 300. Later, when NASA and the Army released an RFP for the Tiltrotor Research Aircraft Program, the design was altered to create the model 301, also known as the XV-15. This model integrated the crucial aeromechanical characteristics learned from the XV-3 that facilitated a smooth and stable transition to high-speed forward flight. [10]

During the late 1970s, the Navy demonstrated a significant interest in tiltrotor technology and provided a substantial portion of the funding for the XV-15 project. Following this, the Navy released the JVX requirement, and throughout the 1980s and 1990s, Bell and Boeing Helicopters collaborated to develop what eventually became the V-22. [10]

Even though XV-15 has remained a prototype, its design's success cleared the path for future development The Bell-Boeing V-22 Osprey has been the first tilt-rotor aircraft to achieve fully operational military status, and currently stands as the only convertiplane actually in service.

In 1981, the Department of Defense launched the Joint-Service Vertical Take-Off/Landing Experimental (JVX) program to meet the demand for vertical lift, speed, and range. In partnership with Boeing Vertol, Bell submitted a proposal based on an expanded version of the XV-15 for the program, which ultimately resulted in the creation of the Bell Boeing V-22 Osprey (shown in Fig. 1.2). The V-22 Osprey was the first tiltrotor aircraft to enter operational service and to be produced on a large scale. [8] Various experimental and numerical investigations were conducted on the V-22 Osprey, which yielded insights into a range of physical phenomena related to the aerodynamic interaction between the wing and rotor. For example, the research uncovered the download effect in hover, which is the vertical force that arises on the wing in the opposite direction to the rotor thrust when the rotor wake strikes it. [23, 52] Moreover, researchers examined the rotor-rotor interaction at the aircraft symmetry plane and discovered the fountain effect, which had a detrimental impact on the aircraft's performance. Numerical computations showed the same results when a half-model and symmetry requirements were applied to the aircraft symmetry plane. [32]

Figure 1.2: Bell-Boeing V22 Osprey, first production tiltrotor aircraft in hover.

Since the success of the V-22 Osprey, tiltrotors have continued to be developed and improved upon. Other notable tiltrotor aircraft include the Leonardo AW609 (see Fig. 1.3), which is designed for civil use, and the evolution of the V-22 Osprey: the Bell V-280 Valor , which is being developed for the United States Army's Future Vertical Lift (FVL) program.

Over the past decade, Leonardo has been engaged in the development of the AW609 tiltrotor, which is specifically designed for the commercial transport market. Initially a collaboration between Bell Helicopter and AgustaWestland, the Leonardo AW609 made its maiden flight in March 2003. The American Institute of Aeronautics and Astronautics published a technical paper highlighting the advanced aerodynamic and structural designs of the Leonardo AW609 that allow it to achieve high speeds and maneuverability while maintaining efficiency and stability. [19] The paper also emphasizes the aircraft's advanced avionics, fly-by-wire flight controls, and state-of-the-art safety features that make it an attractive option for various applications. Despite significant engineering development and financial commitment to the project. The aircraft is notable for being the first pressurized rotorcraft to seek certification, which presents several complex implications, given that no new helicopter category has been certified since 1946. This is just one of the many reasons why the Leonardo AW609 is not yet fully operational. [3]

Figure 1.3: Leonardo AW609 in cruise https://www.leonardo.com/it/.

There are several future developments of tiltrotors in the US that are currently in progress or planned. One of the most notable is the Future Vertical Lift (FVL) program, which aims to replace aging military helicopters with next-generation aircraft. The FVL program includes the development of a new tiltrotor aircraft, the V-280 Valor, by Bell and Lockheed-Martin. The V-280 has completed several successful flight tests and is currently undergoing further testing and evaluation, it is an evolution of the V22 Osprey and it is intended to replace the Sikorsky UH-60 Black Hawk.

In 2014, the Clean Sky 2 Joint Undertaking (CSJU) was established in Europe, which is a partnership between the European Commission and the European aeronautics industry aimed at achieving environmental performance goals. As part of the Clean Sky 2 Fast Rotorcraft Innovative Aircraft Demonstrator Platform (IADP), the EU is providing funding for two high-speed rotorcraft projects: the Airbus RACER compound helicopter (shown in Figure 1.5) and the Leonardo Next-Generation Civil Tiltrotor (NGCTR) (shown in Figure 1.4). [8] Airbus plans to commence flight demonstrations for the RACER aircraft in 2020 and will concentrate on evaluating key performance objectives such as speed, handling qualities, stability, and aerodynamics. [7]

Figure 1.4: Leonardo Next-Generation Civil Tiltrotor. https://www.leonardo.com/it/

Figure 1.5: Airbus RACER. https://www.airbus.com/en/

As tiltrotor technology continues to advance, the potential for its application beyond traditional military and tactical contexts is becoming increasingly apparent. In particular, many small companies are now exploring the possibility of using tiltrotors for urban air mobility, a field that is rapidly gaining traction as cities around the world look for more efficient and sustainable transportation solutions.

By combining the vertical takeoff and landing capabilities of helicopters with the speed and efficiency of fixed-wing aircraft, tiltrotors have the potential to greatly enhance urban transportation, particularly in crowded areas where traditional modes of transportation are often slow and inefficient. With the ability to take off and land vertically, tiltrotors

can bypass many of the limitations of traditional airports and runways, allowing them to operate in a wider range of environments.

However, the challenges of developing and certifying tiltrotors for urban air mobility should not be underestimated. Issues such as noise, safety, and regulatory approval will all need to be addressed before tiltrotors can become a practical and widely adopted mode of urban transportation. Nonetheless, the potential benefits of tiltrotor technology for urban air mobility are significant, and continued research and development in this area are likely to yield exciting new advances in the near future.

1.2. eVTOL - the importance of Mid-Fidelity codes

Electric vertical takeoff and landing (eVTOL) aircraft have emerged as a new and promising category of aerial vehicles. These aircraft utilize multiple rotors powered by electric battery technology, enabling vertical takeoff and landing and reducing dependence on traditional infrastructure such as runways. As a result, eVTOLs are expected to revolutionize urban and regional air mobility and become a major mode of transportation in the future. [2, 11, 34] This new aircraft category is a promising technology that is projected to become a 1.5 $ trillion industry in urban air mobility by the year 2040. [4]

Figure 1.6: Archer midnight eVTOL. https://www.archer.com/midnight.

The design of eVTOLs is driven by mission and safety requirements, resulting in the

use of multi-rotor and multi-wing architectures. However, the aerodynamics of these configurations are dominated by intricate rotor-rotor, wing-rotor, and rotor-wing-airframe interactions that are difficult to simulate and predict. To address this challenge, mid-fidelity tools have emerged as an optimal trade-off between computational cost and desired accuracy, particularly in the early stages of design. While computational fluid dynamics (CFD) methods can analyze these unsteady interactions, the resolution of wake dynamics in conventional CFD tools requires high-order numerical schemes and mesh resolutions that are computationally expensive, making them unsuitable for design space exploration.

Time-accurate RANS simulations of eVTOL aircraft are still computationally demanding and require significant resources. Therefore, high-fidelity CFD tools are often limited to a small number of detailed analyses and are unsuitable for use in designing new eVTOL aircraft due to the large number of required aerodynamic simulations. As a result, a mid-fidelity numerical approach that combines different models is the preferred choice for designers of novel eVTOL aircraft.

Academia and industry have therefore turned their attention to mid-fidelity codes to predict complex aerodynamic interactions. Numerous codes have been developed in recent years, offering a promising approach for eVTOL design and enabling the exploration of large design spaces while maintaining reasonable computational costs. For example, DLR's UPM [53] is an unsteady panel and free-wake code that was originally designed for aeroacoustic simulations of helicopters but has since been applied to complex configurations like compound rotorcraft. [50] To capture the aerodynamic characteristics of rotors and rotor-airframe interactions better, the vortex particle method (VPM) has been widely used. [51] The VPM is a Lagrangian method that solves the Navier-Stokes equations in their vorticity-velocity form and is well-suited to resolving wake dynamics over long distances with minimal computational effort. There are various solvers, such as DUST, GENUVP, FLOWUnsteady, and RCAS-VPM, that model the wake through particles, with the aim of capturing fully resolved rotor-rotor, rotor-wing, wing-rotor, and wing-wing interactions. Recent studies have shown the effectiveness of the VPM in rotorcraft simulations, such as Su et al.'s analysis of the aerodynamic characteristics of an electrically controlled rotor using a viscous VPM-based model. [21] Extensive validation studies need to be conducted in order to verify to which extent and in which flight conditions the mid-fidelity can be used and gives good useful results.

1.3. The eVTOL concept and challenges

At high speed, the main rotor of a helicopter faces the problems of low velocity flow condition on the retreating blade and high velocity conditions on the advancing blade. The first problem leads to large reverse flow regions and high angle of attack, causing high drag due to flow separations. The second one goes along with compressibility effects, increasing noise and wave drag. These problems aggravate with rising cruise speed and disc loading. For a conventional helicopter, the disc loading results from the requirement to provide the necessary lift force to keep the aircraft in the air as well as the thrust component to overcome the resulting drag force of the aircraft.

While tiltrotors have shown great promise as an aviation technology, there are still several limitations and challenges that must be addressed before they can be widely adopted for commercial and military use. Some of the main limitations and challenges for eVTOLs as of today include:

1. **Costs**: eVTOL are complex aircraft with a large number of moving parts, which can make them expensive to operate and maintain. This can be a significant barrier to overcome, particularly for commercial applications where cost-effectiveness is a key consideration.

2. **Noise**: Because of the high rotational speed of their rotors, eVTOL aircraft generate a lot of noise, which might be a significant issue for urban air transportation. In heavily crowded locations, noise may restrict their use.

3. **Range**: While tiltrotors are capable of flying at high speeds over long distances, eVTOL are generally limited in their range compared to them or worse to fixed-wing aircraft. The biggest disadvantage is their reliance on batteries, which can only give a limited range of flight. As a result, eVTOL aircraft may be unable to travel great distances or carry large payloads

4. **Regulations**: Since eVTOL is a new concept, there are no clear regulations for its operation. Governments and aviation authorities must set eVTOL aircraft safety standards, certification processes, and air traffic control systems.

5. **Infrastructures**: In order to function, eVTOLs require particular infrastructure such as vertiports, charging stations, and air traffic management systems. Building this infrastructure will be a big challenge for the future and will need substantial investments.

6. **Safety**: Tiltrotors and eVTOL are still a relatively new, and there are concerns

about their safety. While the V-22 Osprey has had a relatively good safety record, there have been a few accidents [9, 20] that have raised concerns about the safety of these aircraft.

Overall, while tiltrotors and eVTOL have the potential to revolutionize aviation in a number of ways, there are still several limitations and challenges that must be addressed before they can be widely adopted for commercial and military use. As further research and development is conducted, it is likely that these challenges will be addressed, paving the way for wider adoption of this promising technology.

1.3.1. Opportunities and challenges of propeller integration

As anticipated, there has been a recent focus over the complex rotor-rotor, wing-rotor, and rotor-wing-airframe interactions which occurs when a propeller is installed on an aircraft. When a propulsion system is mounted onto an aircraft's airframe, it locally influences the aerodynamic forces acting on the airframe due to the flowfield generated by the propulsor. At the same time, the airframe modifies the flowfield that is experienced by the propulsor. This mutual interaction between the propulsor and airframe exists in all aircraft, altough to various degrees. Even in the early days of aviation, it was known that careful placement of the propulsion system relative to the airframe, particularly near the lifting surfaces and drag-producing bodies, could theoretically increase the efficiency of the propulsor and airframe compared to their isolated performances. [45]

As aircraft design advanced, the importance of considering the propulsor and airframe as an integrated system rather than separate components became evident. The careful installation of a propeller to achieve a performance benefit is known as beneficial propeller integration and it is sketched in Fig. 1.7. The significance of this integration comes from the fact that the propulsor and airframe are mutually dependent, and their individual performances can only be optimized when considered together as a system.

In addition, modern advances in Mid fidelity codes (DUST, RCAS-VPM, FLOWUnsteady, GENUVP...) enabled the study of this kind of aerodynamic interaction in a more affordable manner in comparison to the CFD or experimental studies. This advantage is extremely useful in the preliminary stage of the design. Overall, the interaction between the propulsor and airframe is a critical consideration in aircraft design, and proper integration can result in significant performance gains. As aircraft designs continue to evolve, ongoing research in this area will undoubtedly lead to further improvements in the integration of propulsion systems with airframes.

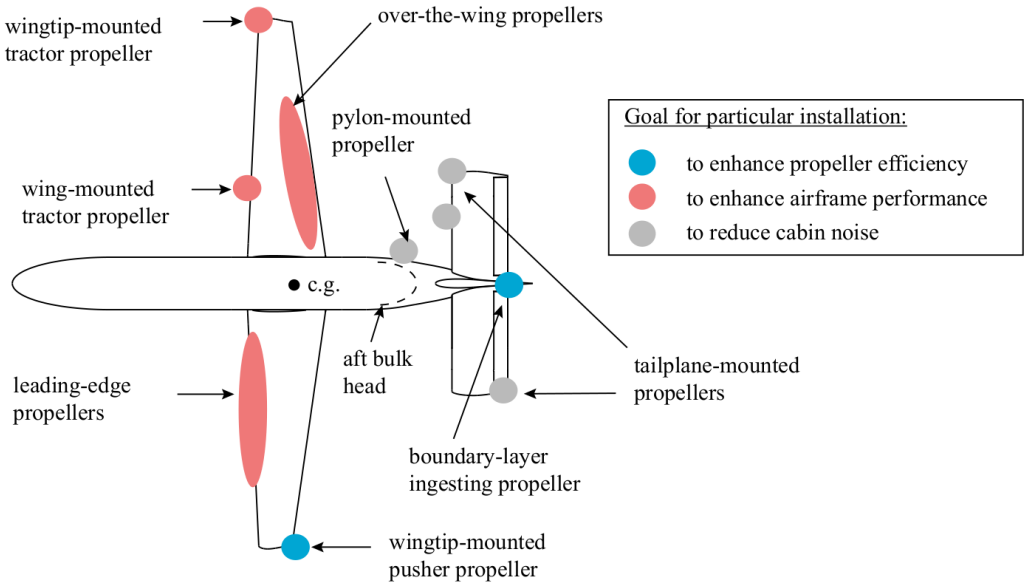

Figure 1.7: Propeller integration options. [45]

In this work a tip-mounted configuration is taken into consideration, maintaining a great applicative flexibility. It can in fact be employed both as a tailplane-mounted tractor propeller or a wingtip-mounted tractor propeller.

1.3.2. Tip-mounted configuration

Traditionally, the standard arrangement for mounting propellers on wings is in a tractor configuration, where the propeller is situated on the inboard part of the wing. The aerodynamic impacts of this arrangement have been extensively researched in studies [45, 48] and can be classified into upstream and downstream effects. however with the increased design flexibility offered by new electrical propulsion systems, new approaches in positioning the propellers on the aircraft began to exist. An example is the wingtip-mounted propeller, which has been thoroughly studied since the 1960s. Snyder and Zumwalt [42] demonstrated that wingtip-mounted tractor propellers can decrease wing drag while improving the wing's maximum lift coefficient and effective aspect ratio. These aerodynamic advantages are achieved by rotating the propeller in the opposite direction to the wingtip vortex, attenuating the vortex and thereby reducing the downstream swirl. Furthermore, modifying the wingtip vortex can also reduce wing induced drag. Subsequent experimental and numerical investigations have confirmed the effectiveness of this approach. [40]

However, there are challenges to implementing wingtip-mounted propellers due to adverse aeroelastic effects caused by the large weight of an engine at the tip of a wing, high wing mass due to inertia loads, and the large yawing-moment arm of the thrust vector in the case of a one-engine-inoperative condition. [45]

In addition to the wingtip-mounted configuration, other concepts exist, such as pylon-mounted propellers and propellers installed at the tip of the horizontal tailplane, which have similar interactions (see Fig. 1.8).

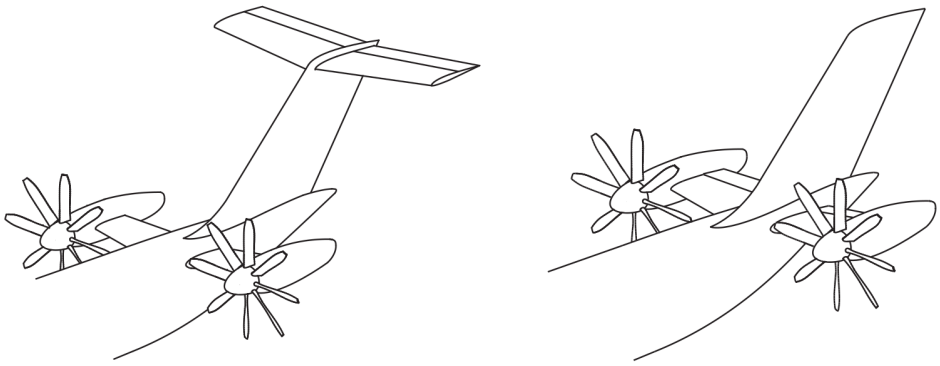

(a) Pylon mounted. (b) Horizontal-tailplane mounted.

Figure 1.8: Tip-mounted propeller configurations. [40]

Noise and Unsteady Aerodynamic Loads

When using a tractor-propeller configuration, the wing or pylon support is partially immersed in the slipstream generated by the propeller. As a result, there are aerodynamic interaction phenomena. [15] The presence of the wing alters the flowfield experienced by the propeller, resulting in unsteady blade loads, noise, and vibrations (upstream effect). Simultaneously, the increased dynamic pressure and swirl in the propeller slipstream modify the inflow to the wing, affecting its lift distribution (downstream effect).

Techniques aimed at achieving high energy efficiency in aircraft integration can lead to additional noise due to non-uniform inflow to the rotor, which can contain high turbulence levels. One disadvantage of unducted propellers is increased cabin noise, especially for flight Mach numbers above 0.6, caused by an additional aerodynamic contribution due to the unsteady pressure field induced by rotating blades and a structure-borne contribution due to vibrations from the engines. Despite successful reductions in noise pollution by various techniques, the cabin noise levels of current turboprops remain several decibels

higher than turbofan-driven aircraft.

Compared to state-of-the-art turbofan engines with the same thrust level, turboprops are inherently noisier due to the absence of a nacelle that acts as a noise shield. Today's aircraft with wing-mounted tractor propellers produce the highest sound pressure levels on the fuselage outer surface within ±30 degrees from the propeller rotation plane. [48]

(a) Embraer Energia Family. (b) Eviaion Alice.

Figure 1.9: Examples of rear-mounted propeller configurations that are in development.

However, mounting the propeller propulsion system to the tailplane or to a pylon, which was proposed in the 1980s [13, 24] and analyzed in this thesis, could significantly reduce the perceived airborne and structure-borne noise. Recently, Embraer announced the Energia Family with either propellers mounted to the vertical tailplane or to pylons mounted to the rear part of the fuselage, shown in Fig. 1.9a. Embraer noted the significant (cabin) noise reductions of this particular layout as a key driver. Moreover, the aft-mounted layout enables a relatively compact integration of alternative fuels, such as hydrogen, compared to a wing-mounted installation. A similar layout has been proposed by the company Eviation for the Alice aircraft, shown in Fig. 1.9b.

1.4. State of the art of wingtip-mounted propeller analysis

Tu Delft University of Technology has always demonstrated significant interest in rotor-wing interaction. In 2005, Veldhuis published his doctoral dissertation [48], which remains one of the most comprehensive articles on the subject, contributing significantly to the advancement of the field. Over the last 5 years great interest shifted towards the aero-

dynamic interaction between wing-tip mounted propellers and lifting surfaces, especially with the growing popularity of eVTOL technology. Over the years, the university has conducted several studies to understand the physical behavior of this complex phenomenon, ranging from experimental studies in their low-speed wind tunnel to high fidelity CFD RANS and LES equations.

One of the earliest experimental studies on this topic was conducted by Sinnige et al. [39, 40], it addresses one of the main problem of this propeller configuration, its impracticability due to aeroelastic problems, high wing tip inertia and insufficient control power. However, with the emergence of more electric aircraft configurations, this design became a feasible option for future aircraft. Sinnige et al.'s study aimed to address the lack of comprehensive analyses of the aerodynamic interaction effects by providing a detailed aerodynamic analysis of the wingtip-mounted configuration. The study involved integral and local force measurements and comprehensive flow field evaluations through an experimental approach. This study was the first to provide such comprehensive data, and its results, along with subsequent CFD studies, were used to validate numerical tools for the analysis conducted in this thesis.

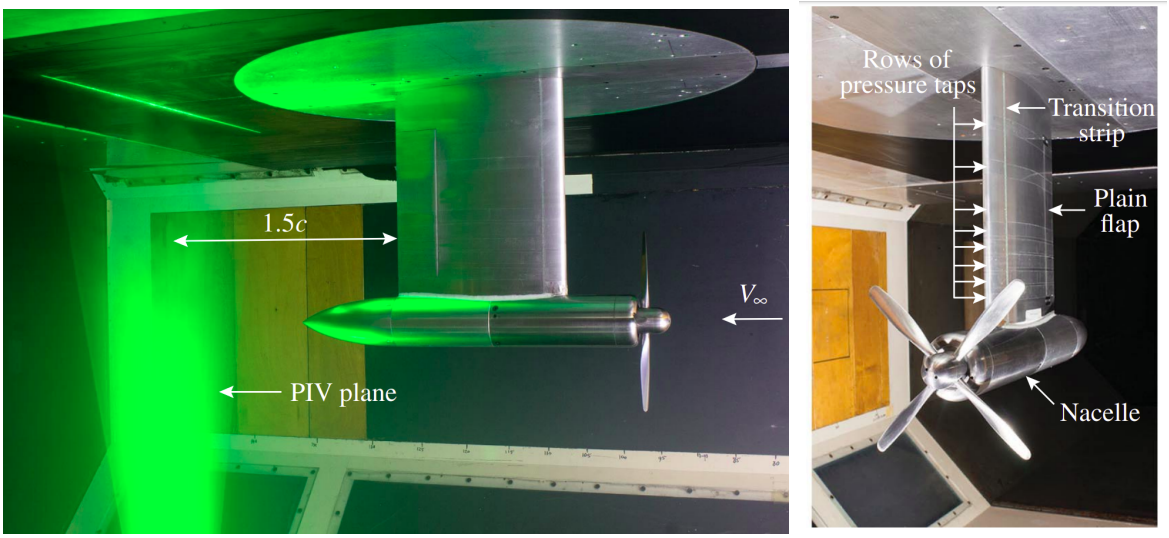

Figure 1.10: Tip-mounted propeller setup installed in the Low-Turbulence Tunnel at TU Delft University of Technology. [40]

Recently, Stokkermans et al. [43] explored the use of commercial RANS solvers for simulating wingtip-mounted propellers with the goal of reducing computational costs while accurately capturing propeller-wing interactions. Previous research had shown that while RANS CFD could predict wingtip vortices with sufficient detail, the large gradients in flow variables required locally dense grids. Additionally, conventional wing-mounted trac-

tor propellers had been adequately captured by RANS CFD, but when the propeller was moved to the wingtip, the complexity of the flow field increased due to the interaction of the propeller-blade vortices and wingtip vortex. To address this issue, they evaluated the accuracy of RANS simulations for this particular configuration and explored the use of actuator-disk (AD) and actuator-line (AL) models. These models replaced propeller blades with distributions of momentum and energy sources along lines or disks, respectively. By comparing full-blade simulations with experimental data from a wind-tunnel test done by Sinnige et al. in [40], Stokkermans was able to investigate the capability of the RANS solver for simulating wingtip-mounted propellers and demonstrated that AD and AL models can accurately represent the propeller for this type of problem, thus reducing computational costs.

Last year, Van Arnhem in his doctoral dissertation [45, 47] exploited the effects of a wing tip mounted propeller mounted on a tailplane but also with the complete aircraft, giving this topic a more complete outlook. This study is significant because of its recent publication and comprehensive validation campaign, making it an excellent reference for subsequent mid-fidelity investigations.

Over the last years, Politecnico di Milano has also made a significant contribution to the study of rotor-wing interaction, with special regards to addressing the noise issue and the computational cost necessary to study of this configuration. The university's involvement in the WIPP program has led to great results, Zanotti A., Savino A. and Cocco A. investigated the WIPP model validating the DUST code with CFD and studying the noise produced by the rotor-wing interaction. [36] Guardone A. and Morelli M. published a scientific article in which they conducted high-fidelity RANS simulations on the TU Delft PROWIM configuration to investigate propeller slipstream interaction and identify key noise generation mechanisms. This study provides valuable insights into the phenomenon and can serve as a reference for future research. [27]

In addition, great progress has been done in the mid-fidelity field where this thesis seeks to make its contribution. Politecnico di Milano has been one of the main players in developing a new open-source program called DUST [1] in collaboration with A^3 Airbus LLC which can reduce the computational effort in studying this complex interaction and that can be extremely useful in initial design stages. DUST has shown great robustness and has given good results with a small computational cost if compared to TU Delft studies. It has been extensively used to study rotor-wing interaction, with works by Molini D. [25] and Piccinini R. [30] serving as excellent examples of its capabilities.

1.5. Scope of the thesis

The primary aim of this research is to investigate the capability of a mid-fidelity code in capturing the aerodynamic interaction and flowfield between a tip-mounted propeller and a wing with a 25%-chord flap and a nacelle, in the context of a maneuver scenario. The analyses will be supported and validated extensively through experimental and CFD data obtained from previous studies published by researchers at Tu Delft University of Technology. The main research questions addressed in this thesis are:

1. What is the potential of a mid-fidelity code in predicting the aerodynamic interaction of a propeller mounted on a wing that has a deflected flap?
2. What aerodynamic interactional aspects need to be captured by a mid fidelity method to ensure accurate estimation of propeller and wing loading?
3. How well does a mid-fidelity solver capture the downstream and upstream effects following the installation of a wing-tip mounted propeller?
4. What are the limitations associated with using a mid-fidelity approach to assess these aerodynamic interactions?
5. What are the advantages, in terms of computational effort and resources, of analyzing this kind of aerodynamic interactions with a mid-fidelity code instead of CFD or experimental studies?

To answer this questions a robust numerical approach is utilized in order to correctly predict this interaction, the mid-fidelity code used for the analysis is the open-source software developed by Politecnico di Milano in collaboration with A^3 by Airbus LLC: DUST (https://www.dust-project.org/). [1] These questions remain unanswered in the context of DUST and other mid-fidelity codes, primarily due to the rapidly evolving eVTOL landscape. As these codes offer a novel approach to the initial phases of eVTOL design, validation studies such as this one are crucial for their development.

1.6. Thesis outline

The numerical simulations conducted in the next chapters are compared with experimental data and CFD studies to demonstrate to what extent the goal of the particular simulation can be met, either qualitatively or quantitatively. The research can be divided into three main parts, the following simulated cases are validated, with increasing level of integration:

1. In section 3.1 focuses on the isolated propeller. This stage is crucial for establishing a baseline to study the aerodynamic interaction between the propeller and the rest of the model. A thorough analysis of the uninstalled propeller is carried out to accurately compare the forces acting on the propeller with experimental and CFD data.

2. The second part involves modeling the isolated wing and studying its flow field, with a focus on flap deflection and loading distributions.

3. At the end, in Chapter 4, here the combined setup of the wing and nacelle with the wing-tip-mounted propeller is modeled, analyzed and validated. This validation study demonstrates the capability of simulating the interaction of the slipstream with a lifting surface by comparing load distributions and the associated flowfields with high fidelity and experimental results.

The flowchart below provides a schematic representation of the organization and development of the work presented in this thesis.

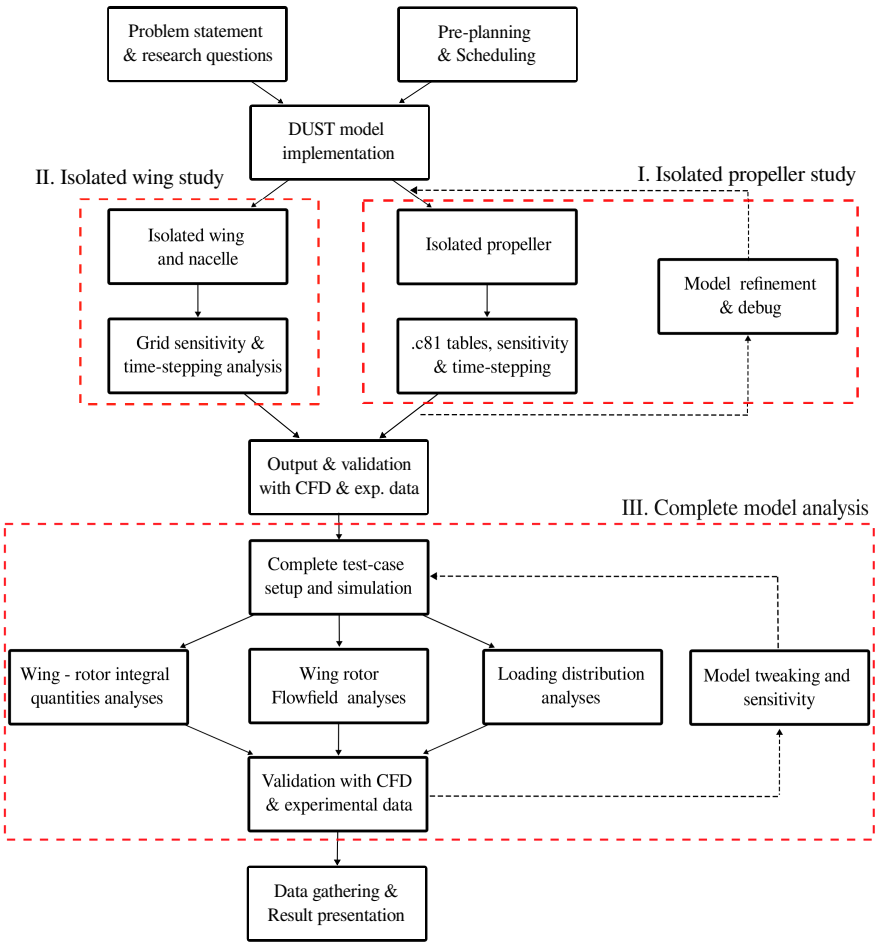

Figure 1.11: Flowchart indicating the steps followed in this thesis.

2 | Methodology

2.1. Aerodynamic tool: DUST

There has been a rising interest in developing a new concept of short-range personal aviation as a viable solution to tackle the issue of overcrowded urban areas and ground transportation. As a result, there has been a substantial increase in development efforts focused on the design of novel VTOL aircraft. However, these aircrafts are characterized by complicated aerodynamic interactions between the rotor wake and wing, which pose significant challenges for their design and analysis. Recent developments in high-performance computing have enabled the use of high-fidelity Computational Fluid Dynamics (CFD) for an in-depth analysis of the complex aerodynamic interactions that distinguish tiltrotor systems. Nonetheless, a significant amount of computational work is still required for time-accurate URANS simulations of tiltrotor aircraft designs, which limits their use in the early stages of the design process.

To address this issue, A^3 by Airbus LLC and Politecnico di Milano have collaborated to develop a new flexible mid-fidelity computational tool called DUST. [1] DUST is an open-source software that uses a variety of aerodynamic modeling approaches, including surface panels, thin vortex lattices, lifting lines for solid bodies, as well as vortex particles for modeling the wake. This tool provides a quick and accurate numerical simulation of complicated rotorcraft configurations, such as eVTOL aircraft, with minimal computational effort.

DUST has been used to model the aerodynamics of the whole Vahana vehicle [26], which features two rows of four rotors arranged in tandem, and the results showed a firm agreement with the flight test data and the high-fidelity CFD results. In a recent study, Tugnoli et al. [44] compared the results of a half-span tilt-wing tiltrotor model and an eVTOL multi-rotor tilt-wing aircraft, both in hover and forward flight mode, obtained with the novel DUST code with experimental data and CFD results. The comparisons showed that DUST produces results that are as accurate as the results obtained with CFD, except for massively separated conditions, at a computational cost order of magnitude lower. There-

fore, highlighting the effectiveness of this approach for the preliminary design of a vehicle and the preliminary study of the flow physics related to the aerodynamic interactions between rotor wake and solid bodies such as wings.

Moreover, in the work by Zanotti et al. [54], the accuracy of the mid-fidelity approach implemented in DUST for the simulation of tiltrotor aerodynamics with respect to CFD has been assessed. The results showed a reasonably good agreement between the mid-fidelity solver based on vortex particle methods and the CFD results obtained over the various analyzed flight conditions, suggesting that the code is suitable for investigating the primary interactional flow features that characterize tiltrotor aerodynamics. Overall, the DUST tool offers a promising approach for the preliminary design and analysis of innovative rotary-wing aircraft, which can help to reduce development costs and accelerate the time-to-market for these advanced aerial vehicles.

2.1.1. Structure and formulation of the DUST code

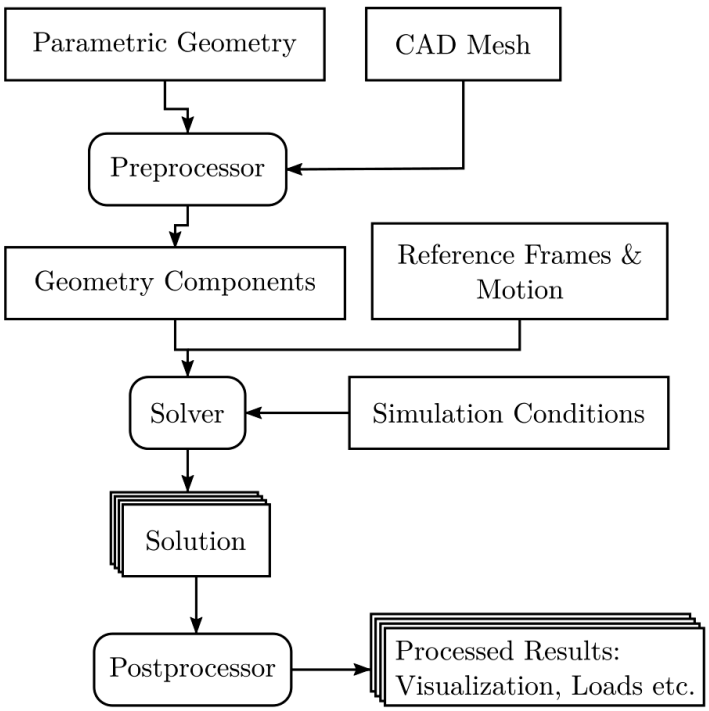

Figure 2.1: Workflow of DUST. [44]

The program is divided into three parts: pre-processing, solving, and post-processing. Figure 2.1 shows the typical workflow. The pre-processor allows the user to import components from pre-existing mesh files or generate parametric components by specifying the

geometry in the input files. The solver's mathematical formulation is limited to rigid bodies, and flexible components cannot be simulated. The solid bodies are modeled as a surface distribution of singularities, and different aerodynamic models ranging from one-dimensional lifting lines and actuator disks to three-dimensional surface panels are available in DUST. The intensity of the singularities is determined by solving the boundary value problem for the potential part of the velocity vector, which is supplied with the non-penetration boundary condition. The components are positioned in space and set in motion by defining a hierarchy of reference frames.

The inputs to the solver include the geometry and mesh of each component, reference frames, simulation conditions, and solver parameters. The solver evolves the simulation in time for a specified number of steps and writes the solution to screen or files as specified by the user. The Kutta condition is enforced by shedding wake from the trailing edges of the lifting bodies, which are automatically detected by the solver using the geometry.

The code is based on the assumption of incompressible potential flow, although compressibility effects can be considered for steady aerodynamic loads on surfaces by applying a Prandtl-Glauert correction for surface panels and vortex lattice elements while using Mach-dependent tabulated data for lifting lines elements. The code is written using the latest Fortran standards, exploiting object-oriented capabilities to achieve flexibility while maintaining high computational performance, aided by an extensive OpenMP parallelization. [44]

The mathematical formulation of the aerodynamic solver is based on the Helmholtz's decomposition of the velocity field and a Lagrangian description of the vorticity field, founded on the vorticity-velocity formulation of the aerodynamic problem (for more detailed informations see [28]). According to the Helmholtz's decomposition of the velocity field, the velocity field $\vec{u}(\vec{r},t)$ can be expressed as the sum of an irrotational field, the potential velocity $\vec{u}_\phi = \nabla\phi$, which will be bound to the potential-based elements, and a solenoidal field, the rotational velocity $\vec{u}_{\vec{\psi}} = \nabla \times \vec{\psi}$, which will be bound to the particle wake.

$$\vec{u}(\vec{r},t) = \vec{u}_\phi(\vec{r},t) + \vec{u}_{\vec{\psi}}(\vec{r},t) \tag{2.1}$$

The incompressibility condition and the Helmholtz decomposition give rise to two problems that pertain to the potential velocity ϕ and the vector potential $\vec{\psi}$. The solution is advanced in time using a time-stepping algorithm that alternates the solution of a three dimensional boundary element method for $\vec{u}_\phi$ and the Lagrangian evolution in time of the rotational part of the velocity $\vec{u}_{\vec{\psi}}$. Only the surface mesh of the model is necessary, and various aerodynamic components, such as lifting line elements, zero-thickness lifting

surfaces, and surface panels, allow for varying levels of model accuracy. A Morino-like formulation for the velocity potential associates surface panels with a piecewise-uniform distribution of doublets and sources. [29]

Lifting line method

High aspect ratio lifting bodies, such as rotor blades, can be effectively modeled using one-dimensional lifting line elements, which incorporate viscous effects modeling based on tabulated aerodynamic performance of two-dimensional sections of the body. Each lifting line element includes a vortex ring, along with its trailing vortices, and the last line vortex is released in the wake in the spanwise direction. According to Helmholtz's vorticity theorem, a vortex filament cannot end in a fluid. As a result, two free-trailing vortex filaments must continue to infinity, ultimately creating what is known as the "Horseshoe Vortex," as depicted in Fig. 2.2.

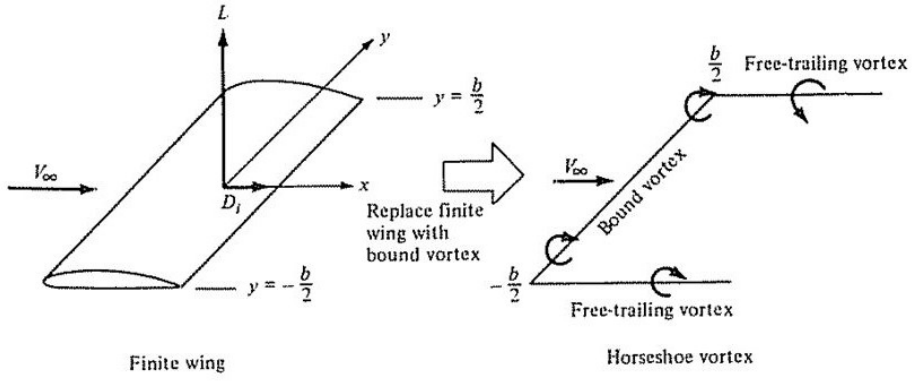

Figure 2.2: Representation of an high AR wing through a single Bound vortex ring. [6]

However, approximating a lifting body with just a single horseshoe vortex produces a constant spanwise circulation $\Gamma(y)$ that fails to accurately represent the actual body circulation. To more accurately capture the non-constant spanwise aerodynamic characteristics of a lifting body, a large number of horseshoe vortices are used. These vortices have all bound vortices coincident along a single line, known as the "Lifting Line".

The discrete representation involves subdividing into a series of uniform-circulation lifting line elements, which model a vortex ring that is as wide as the lifting line segment and as long as the airfoil chord. This vortex ring of intensity Γ_{i_l} consists of the lifting line segment along with its trailing vortices and the last line vortex released in the wake aligned with the spanwise direction. The vortex ring is equivalent to a uniform surface doublet panel, $\mu_{i_l} = \Gamma_{i_l}$. The set of these lifting line rings form the surface S_l. [44]

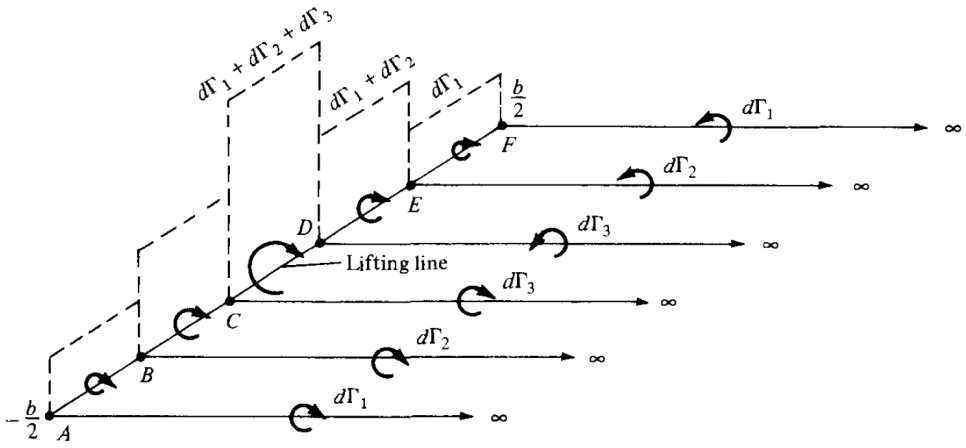

Figure 2.3: Schematic representation of a superposition of a finite number horseshoe vortices along a lifting line. [6]

The intensity of the vortex ring (Γ) and hence the lifting line is calculated using a fixed point algorithm that solves a nonlinear problem, connecting the lifting line intensity to the tabulated aerodynamic coefficients of the lifting sections. To achieve this, the formulation employed in DUST uses two solvers, a loosely-coupled Γ-method [12] and an α-method. [31] The Γ-method is based on the equivalence of the semi-empirical equation for sectional lift with its analytical expression from the Kutta-Joukowski theorem. The lift curve $C_l(\alpha)$ is calculated from the incidence angle α and the relative velocity U_{rel}, which are evaluated at the control point of the i^{th} lifting line. When the lifting line element is located at 1/4 of the chord, the control point is evaluated at 3/4 of the chord. [12, 31]

In the α-method, the incidence angle resulting from the velocity field induced by all of the wake elements, including particles and all the different lifting line elements, is considered as the input to find the corresponding aerodynamic coefficients in the two-dimensional tabulated aerodynamic data. The nonlinear problem of computing the loads on lifting lines is solved through an iterative procedure that takes into account their mutual interference by using the Kutta-Joukowski theorem to evaluate the circulations of the elements from their lift.

Vortex-Lattice method

The non-penetration boundary condition for thin lifting bodies can be modeled using a zero-thickness, two-dimensional vortex sheet, denoted as S_v.

$$\hat{\boldsymbol{n}} \cdot \boldsymbol{u}_{\phi} = \hat{\boldsymbol{n}} \cdot (\boldsymbol{u}_{\boldsymbol{b}} - \boldsymbol{U}_{\infty} - \boldsymbol{u}_{\psi}) \triangleq \sigma \qquad \text{on } S_v, \tag{2.2}$$

To give a discrete representation of the mean surface of thin lifting bodies modeled as a vortex sheet S_v, the vortex lattice method is employed to give the aerodynamic elements. These elements consist of a sheet of vortex rings with intensity Γ_{i_v}, equivalent to a piecewise-uniform surface doublet distribution with the same intensity $\mu_{i_v} = \Gamma_{i_v}$, where $i_v = 1, ..., N_v$. At each panel collocation point, the boundary condition eq. 2.2 is applied and the contribution to the velocity due to all singular elements is made explicit. This leads to the formulation of the equation 2.3.

$$\begin{aligned} \sum_{K_s=1}^{N_s} C_{i_v k_s} \mu_{k_s} + \sum_{K_v=1}^{N_v} C_{i_v k_v} \mu_{k_v} + \sum_{K_l=1}^{N_l} C_{i_v k_l} \mu_{k_l} + \sum_{K_s=1}^{N_s} D_{i_v k_s} \sigma_{k_s} + \\ + \sum_{K_w=1}^{N_w} C_{i_v k_w} \mu_{k_w} = \sigma_{i_v}, \qquad \forall i_v = 1, ..., N_v, \end{aligned} \tag{2.3}$$

where C_{ik} and D_{ik} represents the induced velocity of the k^{th} doublet and source panel at the point of interest.

$$\begin{aligned} C_{ik} &= -\hat{\boldsymbol{n}}_{\boldsymbol{i}} \cdot \boldsymbol{\nabla} \int_{S_k} \hat{\boldsymbol{n}}_{\boldsymbol{k}} \cdot \boldsymbol{\nabla}_{\mathbf{0}} G(\boldsymbol{r_0}, \boldsymbol{r_i}) dS(\boldsymbol{r_0}) \\ D_{ik} &= -\hat{\boldsymbol{n}}_{\boldsymbol{i}} \cdot \boldsymbol{\nabla} \int_{S_k} G(\boldsymbol{r_0}, \boldsymbol{r_i}) dS(\boldsymbol{r_0}) \end{aligned} \tag{2.4}$$

To enforce the Kutta condition, a wake panel is released at each time step in the flow direction from the trailing edge panels, with an intensity equal to that of the trailing edge panel itself.

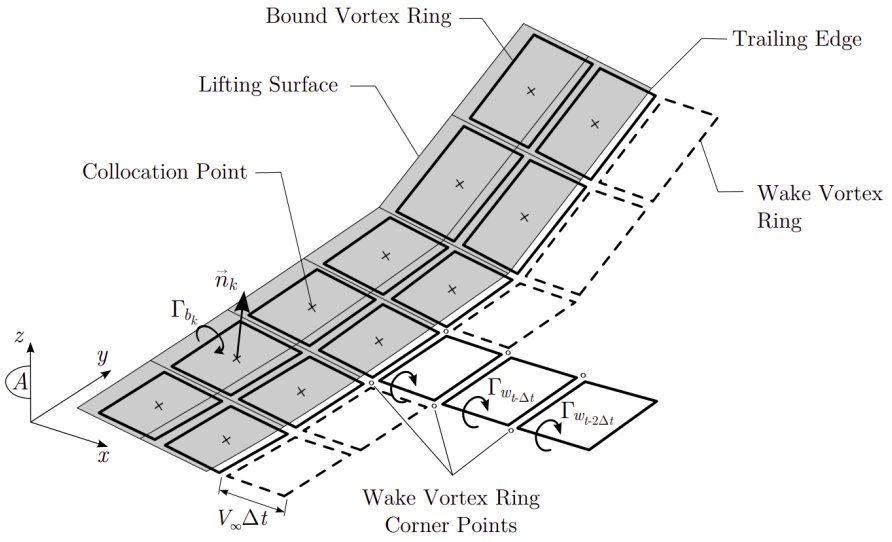

Figure 2.4: Unsteady vortex Lattice Method (UVLM). [14]

For the entire wing shown in Figure 2.4, the velocity induced by all vortices at any arbitrary control point can be calculated using Biot-Savart's law. The tangential flow direction condition is then applied to all control points, resulting in a linear system of equations from which the unknown vorticities Γ_{i_v} can be determined [6]. Once the circulation strengths are known, the Kutta-Joukowsky theorem can be used to calculate the resulting aerodynamic forces.

It is important to note that the vortex-lattice method is a popular and widely used approach for predicting the aerodynamic behavior of lifting surfaces, but it has some limitations. For example, it assumes that the flow is two-dimensional and that the wing is infinitely long. This assumption may not be accurate for short wings or wings with significant taper. Additionally, the method does not account for viscous effects, which can be important in certain conditions such as low Reynolds number flows.

Panel method

The unsteady linearised compressible potential equation describes the flow of an inviscid fluid in a steady state. It can be derived from the full potential equation, considering the complete potential as the sum of the potential of the uniform flow $U_\infty x$ (independent from time) plus a time-dependent perturbed potential ϕ.

$$\Phi(x, y, z, t) = U_\infty x + \phi(x, y, z, t) \tag{2.5}$$

The equation for the linearised potential is written as follows:

$$(1 - M_\infty)\frac{\partial^2 \phi}{\partial x^2} + \frac{\partial^2 \phi}{\partial y^2} + \frac{\partial^2 \phi}{\partial z^2} = \frac{1}{c_\infty^2}\left(\frac{\partial^2 \phi}{\partial t^2} + 2U_\infty \frac{\partial^2 \phi}{\partial t \partial x}\right) \tag{2.6}$$

where ϕ is the perturbed potential function, c_∞ is the speed of sound of the unperturbed flow. This equation describes how disturbances in the potential propagate through the fluid. The first term on the left-hand side, $\nabla^2\phi$, describes the diffusive behavior of the fluid, while the second term, $\frac{1}{c^2}\frac{\partial^2 \phi}{\partial t^2}$, describes the wave behavior. It cannot be used in transonic flows where the non linearities are not negligible anymore.

In the stationary case the linearised potential just reduces to:

$$(1 - M_\infty)\frac{\partial^2 \phi}{\partial x^2} + \frac{\partial^2 \phi}{\partial y^2} + \frac{\partial^2 \phi}{\partial z^2} = 0 \tag{2.7}$$

Through a Prandtl-Glauert transormation we can convert this equation into an elliptic

equation, in so doing reducing it into the Laplace equation for the perturbed potential:

$$\nabla^2 \phi(\boldsymbol{x}) = 0 \tag{2.8}$$

where $\phi(\boldsymbol{x})$ is the perturbation potential and it is the gradient of the velocity, ∇^2 is the Laplacian operator. To find the solution $u(\boldsymbol{x})$ to this partial differential equation (PDE), we can use a boundary integral equation. First, we need to find the Green's function $G(\boldsymbol{x}, \boldsymbol{y})$ for the Laplacian operator, which satisfies the equation:

$$\nabla^2 G(\boldsymbol{x}, \boldsymbol{y}) = \delta(\boldsymbol{x} - \boldsymbol{y}) \tag{2.9}$$

where $\delta(\boldsymbol{x} - \boldsymbol{y})$ is the Dirac delta function.

Once we have found the Green's function, we can use it to find the solution to the PDE by convolution with the known function $f(\boldsymbol{x})$:

$$\phi(\boldsymbol{x}) = \int_{\Omega} G(\boldsymbol{x}, \boldsymbol{y}) f(\boldsymbol{y}) d\boldsymbol{y} \tag{2.10}$$

where Ω is the domain of the PDE and the integral is taken over the entire domain. This is the general form of the Morino equation for the Laplacian of the velocity. To turn this into a boundary integral equation, we evaluate the above integral only over the boundary of the domain and write:

$$\phi(\boldsymbol{y}) = \int_{\partial\Omega} G(\boldsymbol{x}, \boldsymbol{y}) \frac{\partial \phi(\boldsymbol{x})}{\partial n} dS + \int_{\partial\Omega} \frac{\partial G(\boldsymbol{x}, \boldsymbol{y})}{\partial n} \phi(\boldsymbol{x}) dS \tag{2.11}$$

where $\partial\Omega$ is the boundary of the domain, dS is the surface area element at $\boldsymbol{y}$, and $\frac{\partial}{\partial n}$ denotes the derivative in the normal direction to the boundary at $\boldsymbol{x}$.

This is the general form of the Neumann-Neumann boundary integral equation, which relates the values of the solution $u(\boldsymbol{x})$ to the values of the solution and its normal derivative on the boundary of the domain. To differentiate the boundaries in body and wake, we first need to identify the boundaries in our problem. Let S_b be the boundary of the body and S_w be the boundary of the wake. Then, we can write the Neumann-Neumann boundary integral equation as:

$$\begin{aligned} \phi(\boldsymbol{y}) = &\int_{S_b} G(\boldsymbol{x}, \boldsymbol{y}) \frac{\partial \phi(\boldsymbol{x})}{\partial n} dS_b + \int_{S_b} \frac{\partial G(\boldsymbol{x}, \boldsymbol{y})}{\partial n} \phi(\boldsymbol{x}) dS_b + \\ &+ \int_{S_w} \frac{\partial G(\boldsymbol{x}, \boldsymbol{y})}{\partial n_w} \phi(\boldsymbol{x}) dS_w + \int_{S_b} G(\boldsymbol{x}, \boldsymbol{y}) \frac{\partial \phi(\boldsymbol{x})}{\partial n_w} dS_w \end{aligned} \tag{2.12}$$

where ∂n and ∂n_w are the normal derivatives on the body and wake boundaries, respectively.

This equation separates the contributions to the solution from the body and wake boundaries, allowing us to solve for the velocity field in the presence of both types of boundaries. To solve this equation numerically, we can discretise the boundaries and use numerical methods, such as the boundary element method (BEM) or panels method, to evaluate the integrals and find the solution.

Let's focus on the wake integrals. The second integral cancels out because of the boundary condition on the wake that imposes that the normal component of the velocity on the upper and lower part of the wake are equal hence no fluid can come across the wake. As far as the first term goes it can be manipulated, in fact the wake is often considered as a region of separated flow, where the fluid is moving in different tangential directions on the upper and lower parts of the wake. The upper and lower parts of the wake are often denoted as ϕ_u and ϕ_l, respectively. The velocity potential in the wake can therefore be written as:

$$\phi(\boldsymbol{x}, t) = \phi_u(\boldsymbol{x}, t) + \phi_l(\boldsymbol{x}, t) \tag{2.13}$$

Knowing this, we can separate the terms for ϕ_u and ϕ_l:

$$\int_{S_w} \frac{\partial G(\boldsymbol{x}, \boldsymbol{y})}{\partial n_w} \phi(\boldsymbol{x}) dS_w = \int_{S_w} \frac{\partial G(\boldsymbol{x}, \boldsymbol{y})}{\partial n_w^u} \phi_u(\boldsymbol{x}, t) dS_w + \int_{S_w} \frac{\partial G(\boldsymbol{x}, \boldsymbol{y})}{\partial n_w^l} \phi_l(\boldsymbol{x}, t) dS_w \tag{2.14}$$

And since $\frac{\partial}{\partial n_w^u} = -\frac{\partial}{\partial n_w^l}$ this expression is equivalent to:

$$\int_{S_w} (\phi_u(\boldsymbol{x}, t) - \phi_l(\boldsymbol{x}, t)) \frac{\partial G(\boldsymbol{x}, \boldsymbol{y})}{\partial n_w} dS_w = \int_{S_w} \Delta\phi(\boldsymbol{x}, t) \frac{\partial G(\boldsymbol{x}, \boldsymbol{y})}{\partial n_w} dS_w \tag{2.15}$$

Introducing then the Domain function $E(\boldsymbol{x})$ which is a linear operator that maps the velocity field to the perturbation potential we retrieve the Morino integral formulation:

$$\begin{aligned} E(\boldsymbol{x})\phi(\boldsymbol{y}, t) = & \\ &= \int_{S_b} \left(\phi(\boldsymbol{x}, t) \frac{\partial G(\boldsymbol{x}, \boldsymbol{y})}{\partial n} - G(\boldsymbol{x}, \boldsymbol{y}) \frac{\partial \phi(\boldsymbol{x}, t)}{\partial n} \right) dS_b + \\ &+ \int_{S_w} \Delta\phi(\boldsymbol{x}, t) \frac{\partial G(\boldsymbol{x}, \boldsymbol{y})}{\partial n_w} dS_w \end{aligned} \tag{2.16}$$

The equation is a boundary integral equation, it relates the values of the solution $\phi(\boldsymbol{y}, t)$ of the partial differential equation (PDE) at a single point $\boldsymbol{y}$ to the values of the solution and its normal derivative on the boundary of the domain.

To solve this equation numerically, we discretize the propeller and wake surface into quadrilateral panels. The equation expresses the potential on the boundary of the domain as the superposition of the potentials induced by a continuous source distribution, G, on the surface, S_b, and a continuous dipole distribution, $\frac{\partial G(\boldsymbol{x},\boldsymbol{y})}{\partial n}$, on the surface S_b and its wake S_w. The strength of this method is that it can be used to solve for the solution $\phi(\boldsymbol{y}, t)$ at a single point $\boldsymbol{y}$ by numerically evaluating the integrals over the boundary of the domain. $\Delta\phi$ is the potential jump across the wake sheet. In the case of unbounded three-dimensional fluid domain the Green's function $\mathrm{G}(\boldsymbol{x}, \boldsymbol{y}) = -\dfrac{1}{4\pi r(\boldsymbol{x}, \boldsymbol{y})}$, with $r(\boldsymbol{x}, \boldsymbol{y}) = ||\boldsymbol{x} - \boldsymbol{y}||$ being the distance between the source and the receiver position,

Vortex particle method

In the field of aerodynamics, a technique called vortex particle numerical modeling has been developed to accurately simulate the wake generated by lifting bodies at their trailing edges. This approach has proven particularly useful for studying the complex aerodynamics of advanced aircraft configurations, including rotorcraft. The VPM is a Lagrangian grid-free method that employs material vortex particles to approximate the vorticity field, describing the wake's evolution through the rotational component of the velocity field $\vec{u}_{\vec{\psi}}$.

When advected downstream, the panel wake is converted into vortex particles in order to obtain a more robust wake formulation that is suitable for the representation of the interactional aerodynamics of both rotorcraft and complex aircraft configurations. Previous studies have demonstrated the effectiveness of this method in providing a more robust representation of the wake interactional aerodynamics. [44] As such, the VPM can be a valuable tool for investigating the aerodynamics of advanced aircraft configurations, while the panel wake shares the same spatial discretisation that is used to model the lifting bodies and the same formulation as vortex lattice elements in terms of geometry and singularity distribution.

2.1.2. Hinged surfaces

A crucial aspect of simulating aircraft maneuvers is accurately modeling the deflection of control surfaces. Recently, DUST has introduced the capability to include control surfaces in the aerodynamic mesh. For the sake of simplicity. In the following, the description of the implemented model for hinged surfaces in DUST is introduced with a two-dimensional example first, and then extended to three-dimensional deformable components.

In a two-dimensional problem, the control surface can be defined in the local reference frame of the component, using the hinge axis position H, the chord-wise direction ξ, and

a blending region [-u,u] to avoid mesh irregularities as the surface rotates by an angle θ (2.5, left). In this model, the rotation axis $\hat{\boldsymbol{h}}$ is assumed to be orthogonal to the plane of the airfoil. An orthonormal reference frame for the hinge is defined with its origin at H and axes $\hat{\boldsymbol{\xi}}, \hat{\boldsymbol{\eta}} = \hat{\boldsymbol{h}} \times \hat{\boldsymbol{\xi}}$, as shown in 2.5. The position of a point relative to this reference frame is given by:

$$\mathbf{r} = \xi\hat{\boldsymbol{\xi}} + \eta\hat{\boldsymbol{\eta}} + h\hat{\boldsymbol{h}} \tag{2.17}$$

Three regions are defined using the coordinates based on this reference frame:

1. $\xi \leq -u$: no influence of the control surface rotation;
2. $\xi \geq u$: rigid rotation about the hinge:

$$\Delta\boldsymbol{r} = \sin\theta\hat{\boldsymbol{h}} \times \boldsymbol{r} + (1 - \cos\theta)\,\hat{\boldsymbol{h}} \times \hat{\boldsymbol{h}} \times \boldsymbol{r} \tag{2.18}$$

3. $-u \leq \xi \geq u$:blending region to avoid irregularities, defined as an arc of a circle whose center is located at point C and whose radius is:

$$\overline{CC'} = \frac{\overline{C'H}}{tan\dfrac{\theta}{2}} \qquad \text{where} \quad \overline{C'H} = u \tag{2.19}$$

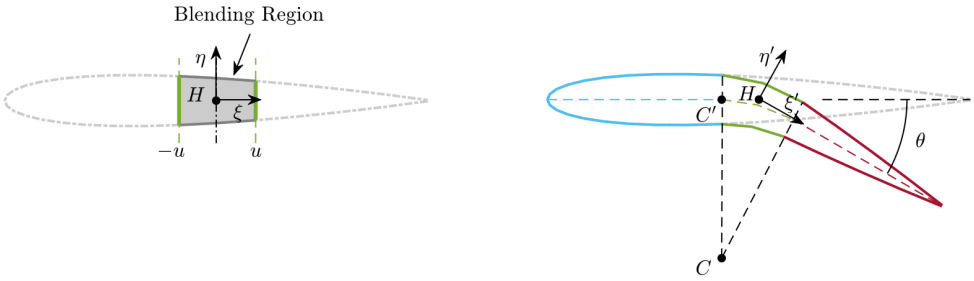

Figure 2.5: Scheme of two-dimensional hinged surface configuration.[35]

In a three-dimensional problem, the reference configuration of a control surface for a generic swept wing is defined in the wind axis reference frame of the component, as shown in 2.6.

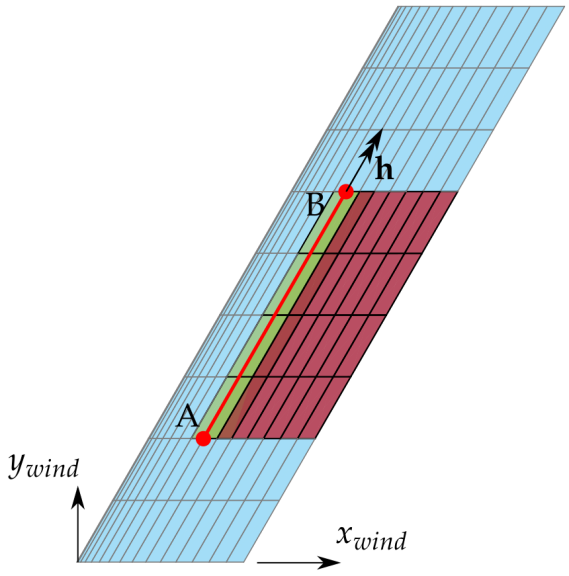

Figure 2.6: Hinge reference system for a swept wing. [35]

To achieve control surface deflection in a swept wing, the aerodynamic sections that satisfy the condition $y(A) < y(P) < y(B)$ are involved, where $y(P)$ represents the ordinate of the $P_i - th$ aerodynamic mesh point expressed in the wind reference system. In the case of a 2D model, each stripe identified at the previous point can be defined in three regions. The y coordinate of the sectional reference frame's origin is determined by linear interpolation between points A and B.

If the movable surface is coupled with a structural component in MBDyn solver, the orientation of the hinge in DUST nodes comes from the MBDyn model's node orientation. The rotation axis is defined as $\hat{\boldsymbol{h}} = \dfrac{(B-A)}{\|B-A\|}$. To obtain kinematic variables for each movable surface point, the point is linked to the hinge nodes, and a weighted average of the motion induced by the hinge nodes' rotation is calculated. The weights w_{ph} are determined by considering only the h components of the vectors connecting the control surface points to the hinge nodes. [35]

3 | Aerodynamic Model

Characterizing the aerodynamic interaction between the propeller and airframe requires a comprehensive understanding of the propeller-induced flowfield and propeller forces under various conditions. This section lies the foundation for this understanding by evaluating the propeller's performance in the absence of the wing and nacelle. Even an analysis of the isolated propeller provides insights into the potential impact of propeller installation at the aircraft level. Subsequently, when the airframe is included in the analyses, it becomes possible to distinguish between phenomena arising from the interaction between the propeller and airframe and those arising solely from the propeller itself.

3.1. Isolated Propeller Configuration

Thus, a thorough analysis of the uninstalled propeller is crucial to establishing a baseline for studying the aerodynamic interaction between the propeller and the rest of the model.

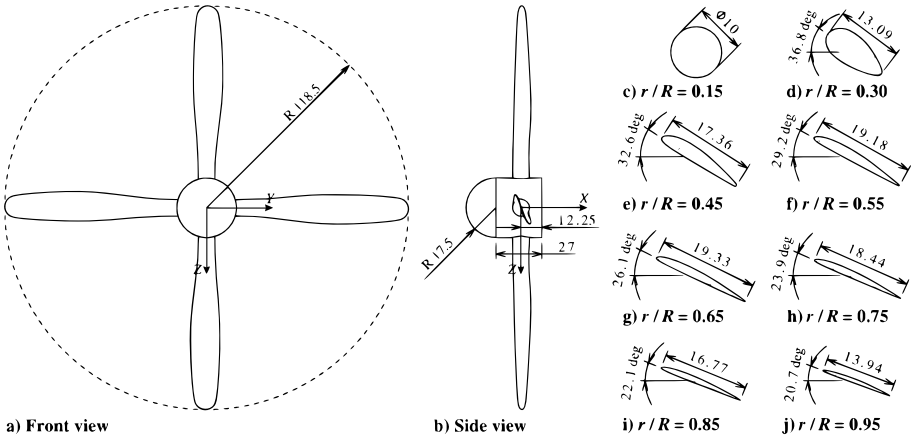

Figure 3.1: Technical drawing of the propeller geometry. [39]

The propeller geometry used in this study is the same as that of the original propeller on the de Havilland DHC-2 Beaver. The propeller is named "TU Delft TUD-PROWIM" and was selected as the most suitable option. The model is specifically designed for investigating propeller-wing interaction effects in low-speed wind tunnel tests and has been

extensively used in aerodynamic research. The availability of high-quality aerodynamic experimental measurements from Sinnige et al [40] and of extensive literature on this particular study case, including numerous CFD studies [41, 43] made the PROWIM model a preferred choice.

It features a four-bladed propeller with a rotor radius R of 0.1185 m and a pitch of 23.9° at 0.75 of the radius (see fig. 3.1). The straight blade design with a twist distribution enhances the efficiency of the propeller and reduces aerodynamic noise.

3.1.1. DUST model

To obtain a detailed blade geometry, a 3D scanning process was utilized, with CAD software used to retrieve the blade's surface from the complete model. This approach allowed for high precision and accuracy in obtaining the blade geometry. Detailed analysis of the aerodynamic profiles was performed, with 17 stations extrapolated along the radial direction. From this procedure it was possible to retrieve the sweep, dihedral and angle of attack of each of the 17 blade's section, reproducing the correct geometry of the blade.

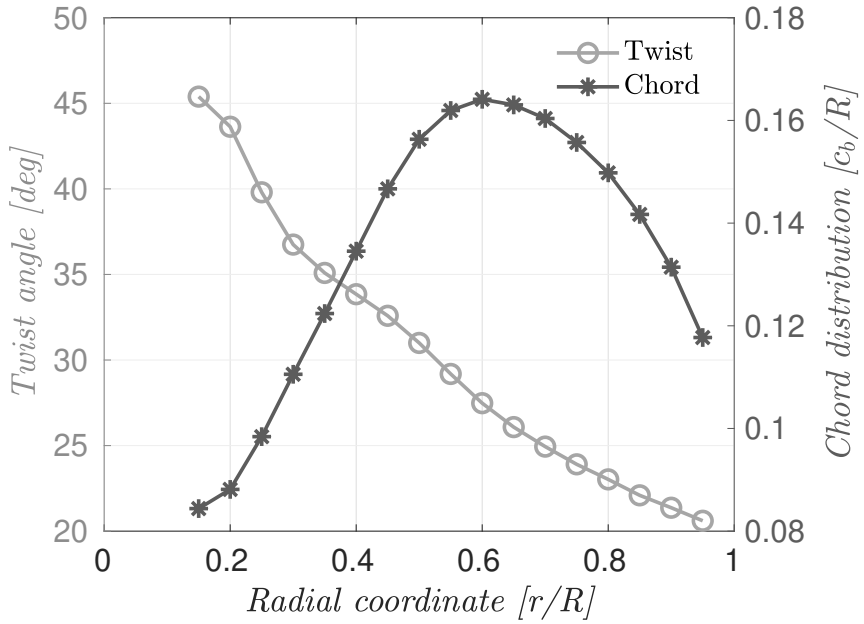

Figure 3.2: Radial distributions of the propeller blade chord and pitch angle.

For the implementation in DUST, after a grid sensitivity analysis, the propeller blades were modeled using 34 equally spaced lifting lines in the radial direction. As described in section 2.1.1, this numerical approach requires defining tables in .c81 format for each station of the propeller.

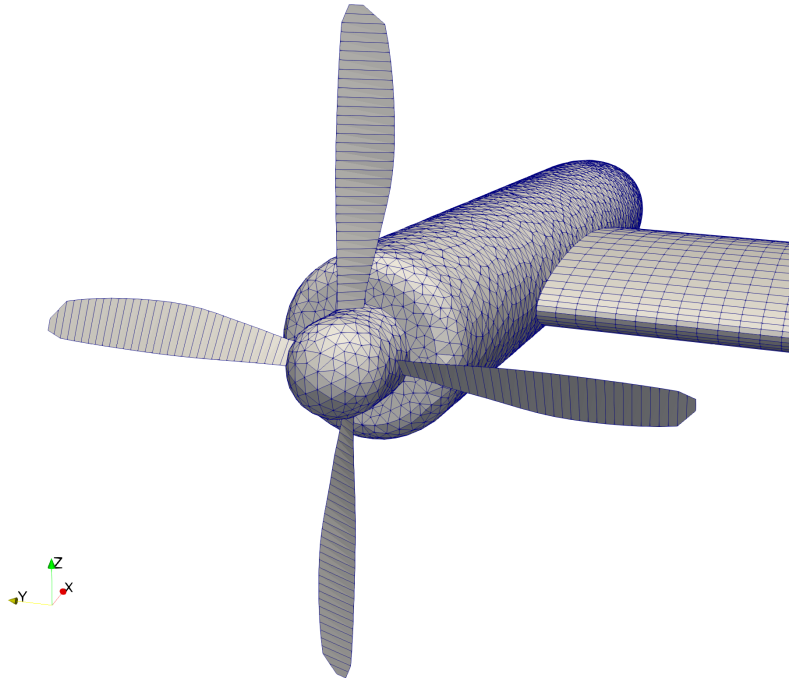

Figure 3.3: Propeller mesh in DUST made by 34 radial lifting lines that are equally spaced in the radial direction.

The .c81 table contains information about the lift, drag, and moment coefficients at various Mach and Reynolds numbers. By using interpolation based on this dataset, a complete aerodynamic description of the propeller can be obtained. This allows for accurate modeling of the propeller's performance and its impact on the overall aerodynamics of the aircraft. As the original profiles for the 17 stations were not available in literature, a set of 10 different NACA airfoil profiles was selected to properly model the rotor blades (see table 3.1). The selection of NACA profiles was performed using airfoil recognition software, which analyzed the .dat file of the original propeller profiles to identify similar airfoils with comparable characteristics. By selecting appropriate airfoil profiles, the aerodynamic behavior of the rotor blades is preserved and can be accurately modeled in DUST.

TUD-PROWIM airfoils		
	from [%]	**to [%]**
NACA 0460	15	25
NACA 2246	30	30
NACA 4428	35	35
NACA 4424	40	40
NACA 4416	45	45
NACA 4413	50	50
NACA 4411	55	55
NACA 2411	60	60
NACA 2410	65	65
NACA 2409	70	70
NACA 2408	75	99.8

Table 3.1: TUD-PROWIM Blade airfoil distribution.

To obtain the necessary aerodynamic coefficients for the propeller, a series of simulations are performed using XFoil, a program developed by NASA that uses a panel method, thereby avoiding the need for a turbulence model. To prevent numerical convergence problems, the simulations are performed at null Mach number, and a Prandtl-Glauert compressibility correction is applied to lift, drag, and moment curves.

$$C_l = \frac{C_{l,0}}{\sqrt{1-M_\infty^2}} \qquad C_d = \frac{C_{d,0}}{\sqrt{1-M_\infty^2}} \qquad C_m = \frac{C_{m,0}}{\sqrt{1-M_\infty^2}} \tag{3.1}$$

However, it should be noted that XFoil has certain limitations, such as its inability to compute post-stall conditions, and it only provides accurate results in the linear region between approximately -10° and 15°. To gather the aerodynamic coefficients for the full range of blade angles (-180° to 180°), the Viterna approximation is employed, which takes into account reverse flow conditions. The approximation calculates the lift and drag coefficients as a weighted combination of trigonometric functions [49], with the weights obtained from the stall conditions and maximum drag coefficient from XFoil simulations. Finally, the moment coefficient is determined from the combination of lift and drag coefficients. A MATLAB algorithm has been developed, it combines the linear portion of Xfoil output with post-stall behavior obtained through a Viterna.m function. The algorithm then applies the Prandtl-Glauert transformation up to Mach 0.7 and iteratively processes

for various angles of attack. The algorithm then stores the outputs into a .c81 file format table. See 3.1 for a summary of the algorithm.

Algorithm 3.1 Viterna Algorithm

1: Give as input stall coefficients: α_s, C_{Ls}, C_{Ds} , AR
2: **for** $all - admissible - \alpha$ **do**
3: Compute drag coefficient at 90° $B_1 = 1.11 + 0.18AR$
4: Compute $A_1 = \dfrac{B_1}{2}$
5: Compute $A_2 = (C_{Ls} - B_1 \sin\alpha_s \cos\alpha_s)\left(\dfrac{\sin\alpha_s}{\cos^2\alpha}\right)$
6: Compute $B_2 = C_{Ds} - B_1 \sin\alpha_s^2 \cos\alpha_s$
7: Compute lift coefficient: $C_l = A_1 \sin 2\alpha + A_2\left(\dfrac{\cos^2\alpha}{\sin\alpha}\right)$
8: Compute drag coefficient: $C_d = B_1 \sin^2\alpha + B_2 \cos\alpha$
9: Compute moment coefficient: $C_m = C_{m,0} + C_{m/\alpha}\alpha$
10: **end for**

Time stepping

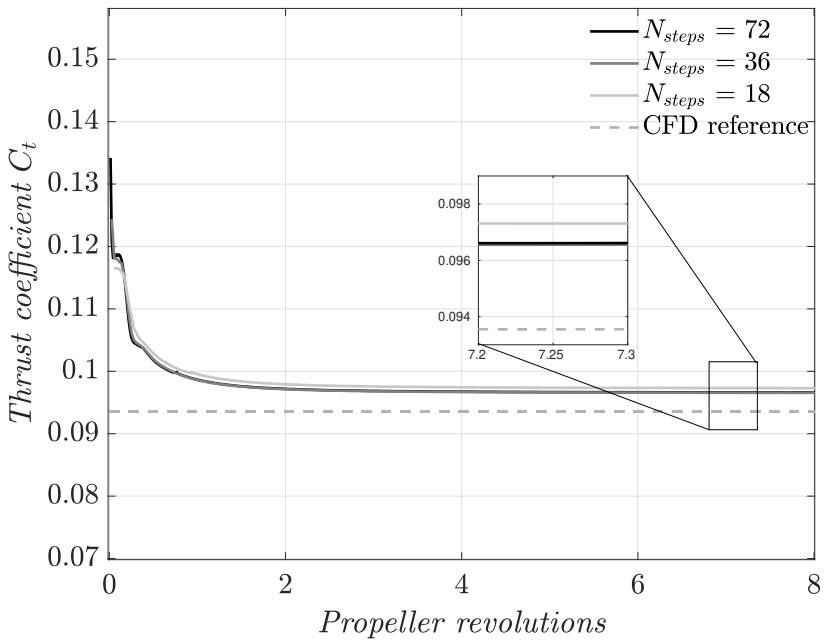

Figure 3.4: Lifting line time stepping convergence for the isolated propeller's thrust coefficient C_T at $J = 0.8$.

In the Dust.in file, the time discretization was set in order to have 72 time steps (N_{steps}) per each complete propeller revolution (equivalent to a vortex particle shed every 5°). To ensure that the time discretization does not influence the solution, a sensitivity analysis on the thrust coefficient C_T was conducted. Figure 3.4 shows that even considering $N_{steps} = 36$ can produce satisfactory results on the integral quantities. However, it was observed that this resolution was not sufficient to accurately capture the propeller wake development and its flow field. Although the temporal resolution used here is rather coarse, the results presented in the following chapters will demonstrate that $N_{steps} = 72$ is sufficient to fully resolve the wake in close proximity to the rotor. The integral results were averaged over the full eighth rotation in so doing considering a result at expired transient, this can be clearly seen in Fig. 3.4, increasing this value will only produce a rise in calculation time since the effective variation in the C_T would result to have less than 0.0003 decrement after one further complete propeller revolution.

Grid study

Grid independence tests were carried out in order to obtain results which are valid regardless the domain and the cells dimension. Different tests were done varying the number of spanwise lifting lines elements in the propeller blade till reaching a value that ensures a robust solution.

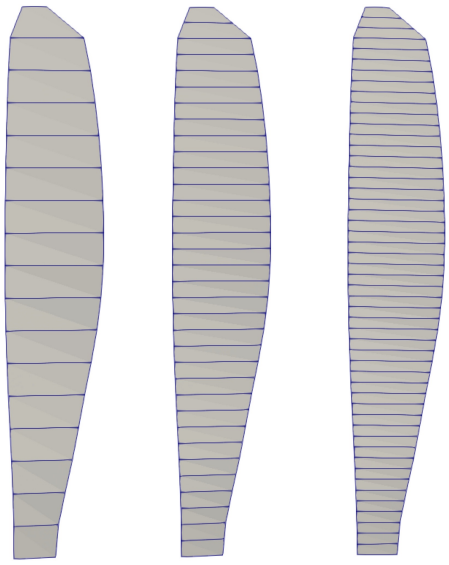

Figure 3.5: Three different mesh refinement cases: first 17 lifting lines, second 34 lifting lines and the third 51 lifting lines.

After, simulations were performed, each time increasing the refinement in order to verify the independence of the grid, see Fig. 3.5. The results are shown in Tab.3.2, here one

can see a series of simulations that were conducted enlarging each time the number of elements until the percentage variation of the C_T reached a confidence region that was set to be $\varepsilon_{C_T} \leq 3.0\%$ from the reference experimental value of Sinnige et Al. in [39].

$$\varepsilon_{C_T} = \frac{|C_{T,CFD} - C_{T,DUST}|}{C_{T,CFD}}\% \tag{3.2}$$

It is important to point out how the error decreases significantly when enlarging the number of lifting lines in the spanwise direction, however the sacrifice in computational time and energy consumption was not notably overcome by the superior amount of detail and definition that the finest case could deliver. So the second case, with 34 spanwise lifting line elements, was selected since it satisfies the criteria chosen and represents a good compromise in computational effort and accuracy of the simulation's outputs.

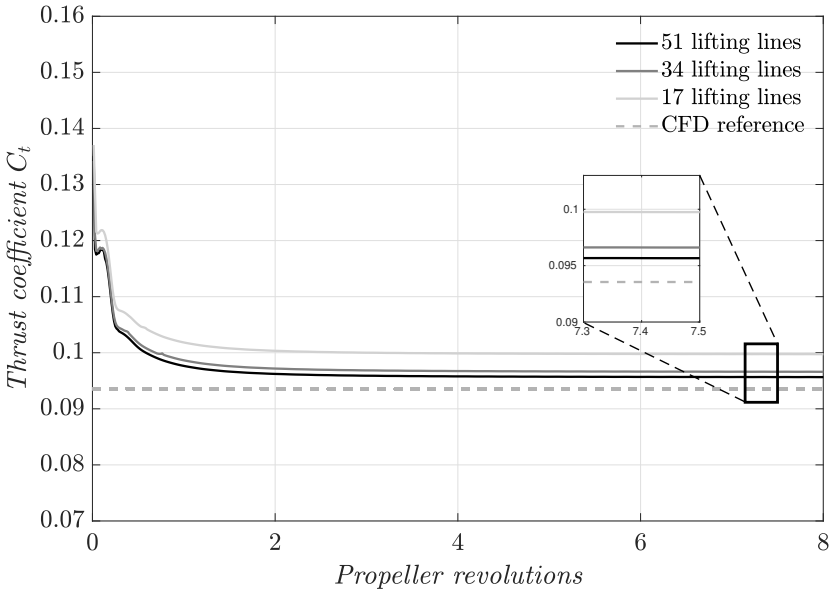

Figure 3.6: Lifting line grid sensitivity for the isolated propeller's thrust coefficient C_T.

Propeller Grid sensitivity				
Case [-]	Number of elements [-]	time [s]	C_T [-]	ε_{C_T} [%]
1	17	2081	0.0997	6.61
2	34	7362	0.0963	2.95
3	51	15266	0.0957	2.28

Table 3.2: Grid sensitivity results for the propeller, the error ε_{C_T} [%] is considered in modulus w.r.t. to the CFD LES value of $C_{T,LES} = 0.935$ [5], the time gives an estimation of how long has taken to complete 8 full revolutions.

3.1.2. Validation of the DUST model for the isolated propeller

To provide a comprehensive understanding of the flowfield characteristics, forces, and loading distributions, both experimental and computational fluid dynamics (CFD) data are used to compare with the output from the mid fidelity code DUST. The geometry of the propeller under consideration and the specific analysis methods used to obtain the experimental and CFD data are described in detail in Fig. 3.1. This allows for a thorough evaluation of the accuracy and reliability of the DUST output and provides a basis for further analysis of the propeller-airframe interaction. Here in the following table are reported the rotor parameters selected after the grid independence and sensitivity studies:

Rotor parameters					
Case	Number of elements	N_{steps}	N_{CRIT}	number of sections	time step dt
2	34	72	9	17	0.0000685

Table 3.3: Rotor parameters selected after the grid independency and sensitivity analysis, all the results are given as average over the eighth full rotor rotation, at expired transient.

Integral Forces

Propeller performance is typically characterized by a set of dimensionless coefficients reported in eq. 3.3, which provide a basis for comparing the performance of different propellers under various operating conditions. These coefficients are critical for maintaining similarity in the loading distributions and slipstream between different propellers, which is essential for ensuring accurate and reliable comparisons. The most important ones, largely used in this thesis are: the Thrust coefficient (C_T), Torque coefficient (C_q) and Power coefficient (C_p).

$$C_T = \frac{T}{\rho_\infty n^2 D_p^4} \qquad C_q = \frac{Q}{\rho_\infty n^2 D_p^5} \qquad C_p = \frac{P_s}{\rho_\infty n^3 D_p^5} \tag{3.3}$$

One of the most important parameters used to describe the operating condition of a propeller is the advance ratio (see eq. 3.4). This ratio is defined as the forward velocity of the aircraft relative to the rotational motion of the propeller. The advance ratio plays a critical role in determining the performance of the propeller, as it directly affects the efficiency and thrust generated by the propeller.

$$J = \frac{V_\infty}{nD_p} \tag{3.4}$$

Fig. 3.7 illustrates a comparison between the thrust and torque coefficients at different advance ratios obtained through DUST simulations and CFD data computed by Sinnige et al. [39]. The results show a high level of agreement for almost every value of advance ratio J. However, the DUST curve for small advance ratios shows a plateau due to the fact that as the rotor tip speed approaches transonic -or worse- sonic speeds at low advance ratios, the rotor blades may stall. It is important to note that DUST does not produce satisfactory results in cases of extreme non-linearities, so the focus of this analysis was on the advance ratio region depicted in Fig. 3.7.

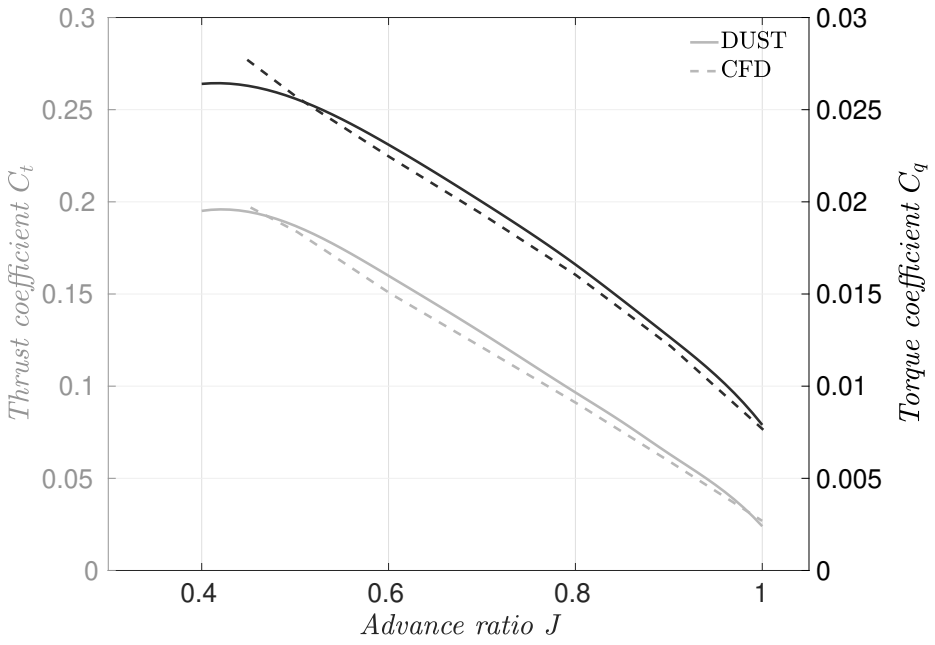

Figure 3.7: Thrust and torque coefficients for the isolated propeller configuration computed with DUST and compared with URANS simulations [39] at different advance ratios J.

Propeller efficiency

After obtaining a good agreement between DUST and CFD results for the thrust and torque coefficient comparison at different advance ratios, further validation of the propeller model was carried out by considering another performance parameter, the Power coefficient C_p, defined in Eq. 3.3. The propeller efficiency η_p was then computed using

Eq. 3.8. The results show a slight overestimation of the propeller efficiency compared to the URANS CFD results, which is expected and acceptable for a mid-fidelity code.

$$\eta_p = J\frac{C_T}{C_p} \tag{3.5}$$

It is worth emphasizing that the significance of the DUST model's accuracy is even more pronounced when compared to experimental data. In fact, the DUST output closely follows the curve of the experimental data, providing further evidence of the reliability of the code in predicting aerodynamic behavior.

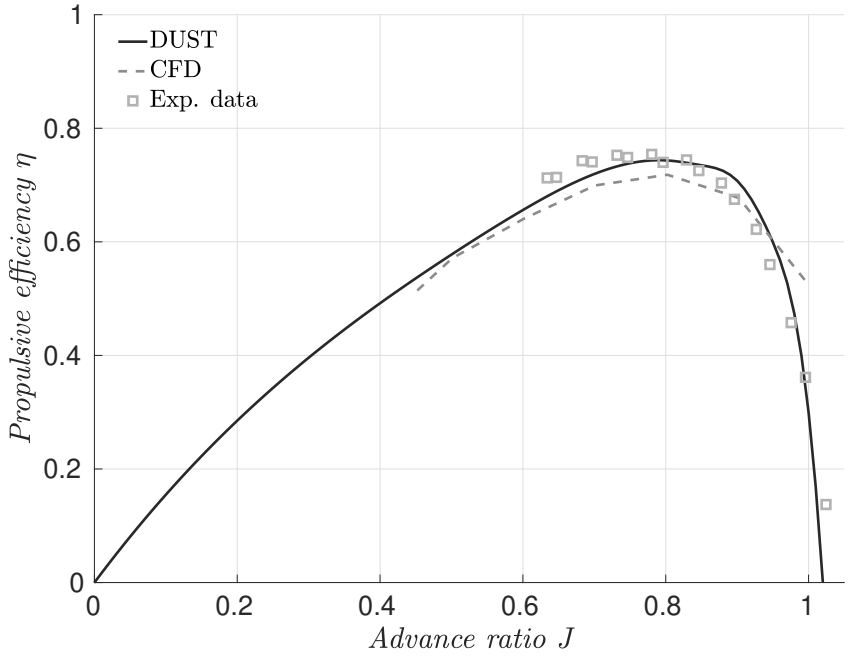

Figure 3.8: Comparison of Propulsive efficiency η with URANS simulations [39] and experimental data [40] at different Advance ratios J.

C_T - Isolated Propeller Configuration			
Configuration	**Model**	**C_T [-]**	**Error ε_{C_T} [%]**
Isolated propeller	DUST	0.096	2.9
	CFD	0.091	3.0
	Experimental	0.094	-

Table 3.4: Thrust coefficient C_T for the isolated propeller configuration. The error ε_{C_T} is computed in modulus w.r.t. the experimental data computed by Sinnige et al in [40].

Radial distributions

In addition to the comparison of performance indices, a more in-depth analysis of the DUST model was conducted by examining the thrust radial distribution normalized with the total thrust developed by the propeller, as shown in Fig. 3.9. It should be noted that DUST is limited in its ability to accurately predict outputs in regions where flow separation occurs. This limitation is particularly evident near the root of the propeller $r/R \leq 0.4$ where the circular blade root geometry induces local flow separation, resulting in expected inaccurate results. However, as the distance from the root increases, the flow becomes more attached and the accuracy of the DUST solver improves accordingly. This is significant because DUST is often used in initial design phases where the performance indices are crucial and the majority of the thrust is generated in the mid-span region. Therefore, the strong correlation between mid and high-fidelity outputs depicted in Fig. 3.9 indicates that those quantities are well-captured. There is an obvious trade-off with accuracy in the root or tip regions, particularly at high rotational speeds. The validation results obtained have demonstrated a high level of accuracy and agreement between the DUST model outputs and CFD and experimental data. These results provide strong evidence to continue using the propeller model for further study and analysis.

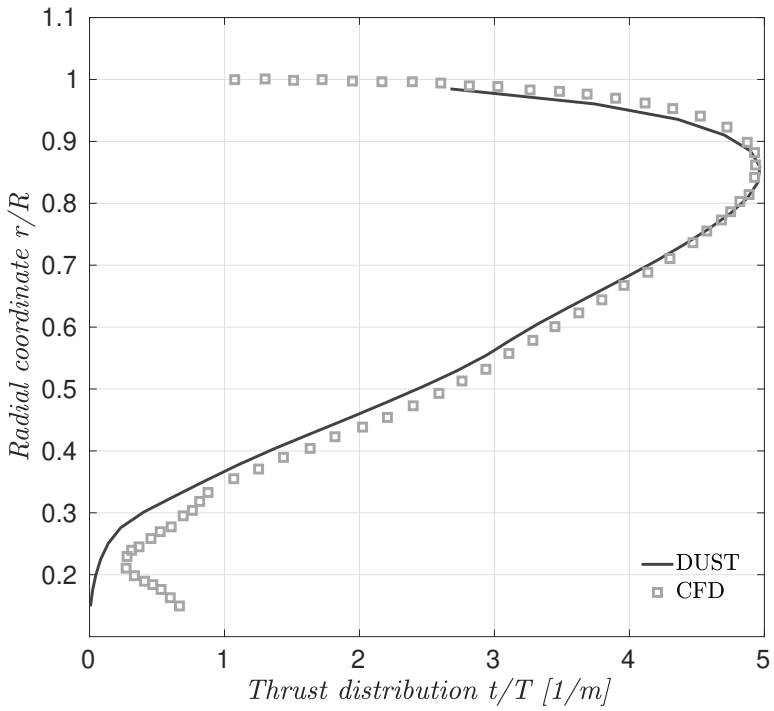

Figure 3.9: Propeller normalized thrust distribution at $J = 0.8$ compared with URANS CFD simulations [43].

3.2. Isolated Wing Configuration

The setup considered in this thesis consisted on a straight, untapered wing with a chord length of 0.240 m, a span of 0.292 m, and a symmetric NACA 64_2A015 profile. An integrated 25%-chord plain flap was also included. The wing had a low aspect ratio and combined with the high ratio of propeller diameter to wingspan, it creates a strong interaction between the propeller slipstream and the wing. This aided in the interpretation of the aerodynamic interaction mechanisms.

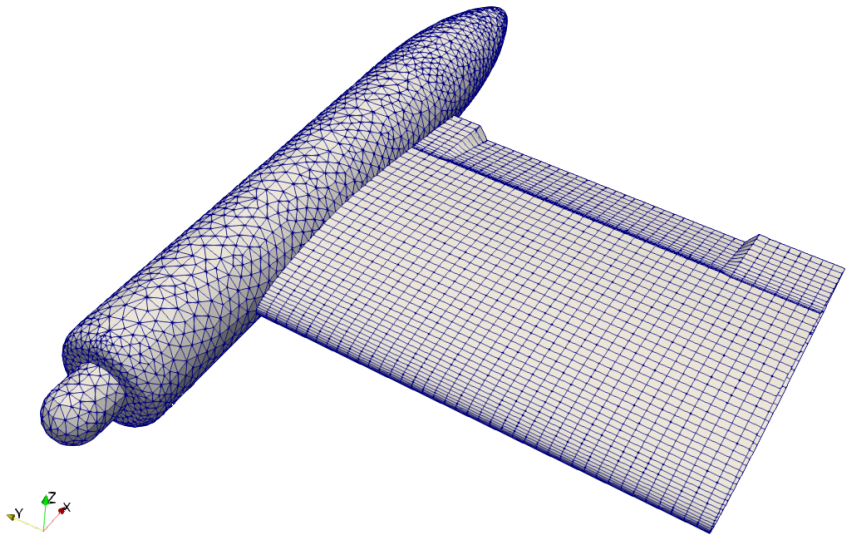

Figure 3.10: DUST model for the wing and nacelle.

It is worth noting that due to the limited spanwise extent of the flap, which only covered the region from $\eta = 0.18$ to $\eta = 0.81$, the resulting lift distribution may differ somewhat from that of a wing with an equal planform but cambered airfoil profile. Moreover, the vorticity shed from the flap side edges was found to cause a reduction in the circulation of the wingtip vortex in the presence of the flap.

3.2.1. DUST model

The first phase of the DUST modeling involved designing a symmetric NACA 64_2A015 profile and generating a .dat file containing the coordinates in Selig format. A 128 point file was created and extruded for the full span length of the model. The next step was to model the integrated 25%-chord flap, utilizing the hinged feature discussed in Sec. 2.1.2.

Various adjustments were made to properly set the "hinge offset" and "hinge spanwise bleeding" parameters to accurately represent the gap between the flap and the wing. Once the isolated wing had been modeled, the focus shifted to modeling the wall. The original test case run by [40], to which this thesis seeks to replicate, involved a wing-tip propeller mounted on a wing directly attached to the wind tunnel wall's balance. This created the need to model the wall and its contribution to the flowfield and loading modification induced on the model.

DUST does not provide a direct mean to model the presence of a wall. The wall was modeled by extending the wing span in the root direction so that the circulation would not decay to zero, but rather continue as if a wall were present (see Fig. 3.11).

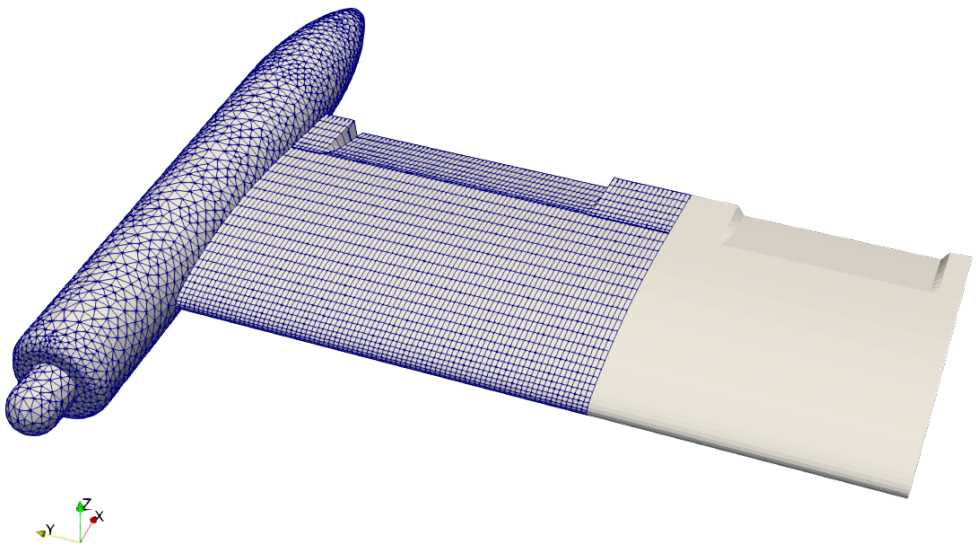

Figure 3.11: DUST model of the wing and nacelle (surface with edges) and extended portion of the wing necessary to model the wall.

The presence of a wall creates a plateau in the root region for the spanwise lift distribution since there the circulation does not go to zero, but remains almost constant to ensure compliance with the Helmholtz theorem discussed in Sec. 2.1.1. However, extending the wing did not yield satisfactory results at every angle of attack. At a null angle of attack, the airfoil's symmetrical shape does not generate lift, and therefore, the plateau would not be present. To address this issue and make the model more robust, another 25%-flap was introduced in the extended portion of the wing to simulate a cambered airfoil, which

could generate lift even at 0° angle of attack, correctly modeling the presence of the wall.

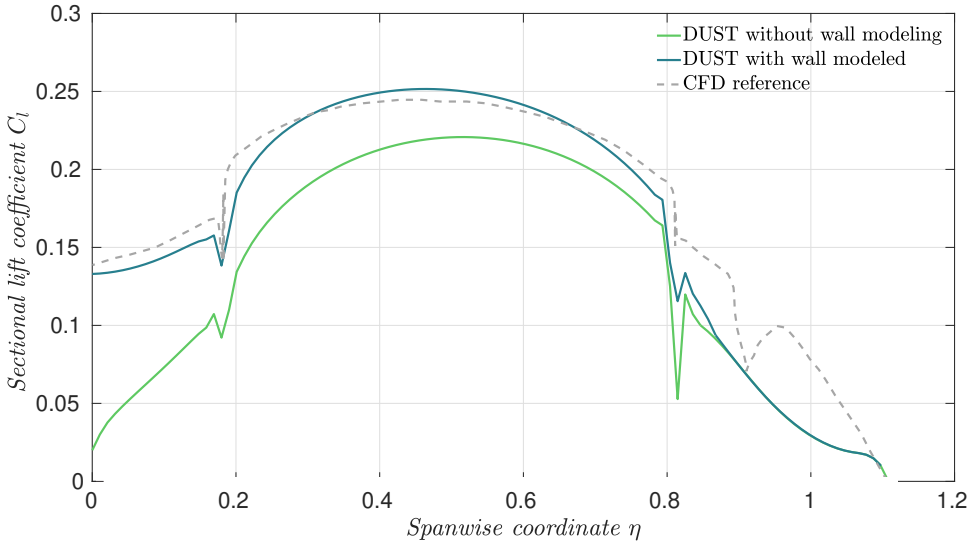

Figure 3.12: Wall effect on the sectional lift coefficient c_l computed at $\alpha = 0°$ and $\delta_e = 10°$. Wing with wall modeled is referred to the configuration depicted in Fig. 3.13a, whereas the wing without wall is depicted in Fig. 3.13b.

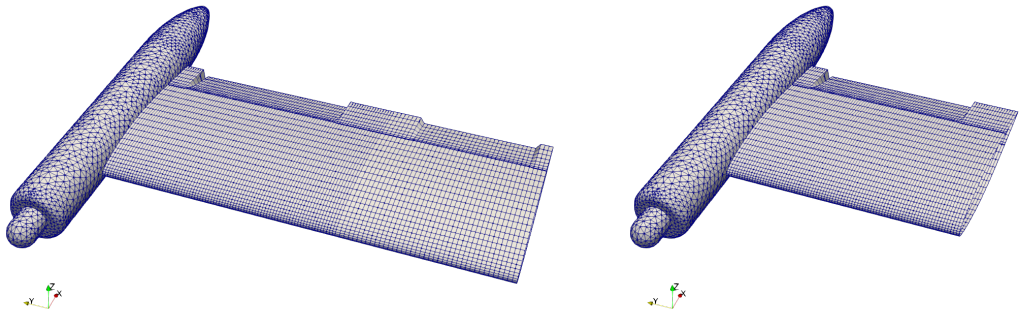

(a) Wing with wall modelling.

(b) Wing without wall modelling

Figure 3.13: Comparison between the DUST model with and without the wall modelling.

Finally, several adjustments and sensitivity analyses were conducted to ensure that the results obtained in the close vicinity of the wall matched those obtained from CFD test cases and experimental data. The model was continuously refined until satisfactory validation results were achieved, providing strong evidence to continue with the study using this wing model. The nacelle in this study was modeled using the mesh generator Pointwise ©, and an unstructured mesh composed of 4,126 elements was generated. The grid

parameters of the nacelle mesh are presented in Table 3.5. It is worth noting that the grid spacing was intentionally kept relatively loose since DUST is not capable of directly computing the aerodynamic loading on the nacelle itself. Instead, it can only compute the influence of the nacelle on the wing flowfield and loadings. As a result, an excessive refinement of the nacelle mesh would be unnecessary and computationally unfavorable. In the post-processing phase, the aerodynamic coefficients were extrapolated at five different sectional slices of the nacelle in Paraview through the "Integrate variables" feature, the C_p over this 5 slices is reported for clarity in Fig. 3.14.

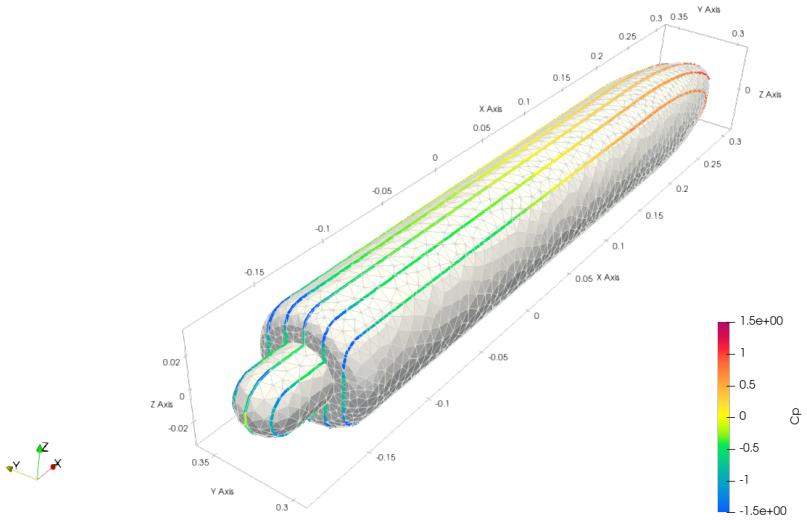

Figure 3.14: Pressure coefficient slices.

Nacelle parameters			
Type	Number of elements	Number of nodes	Grid spacing h
Unstructured	4126	2069	0.05

Table 3.5: Selected nacelle parameters.

Grid Sensitivity

Before diving into this study a necessary clarification has to be done, unlike other numerical techniques such as finite element or finite difference methods, the panel method does not have a real grid convergence study. This is due to the fact that the panel method does not solve the flow field in a physical domain, but instead on a mathematical surface. Hence, increasing the number of panels does not guarantee a more precise solution to the

physical problem but rather to the mathematical surface, which serves as a mere approximation to the physical problem. Another reason why grid convergence is not achieved in the panel method is that the sources and doublets used to represent the flow on each panel become progressively closer to each other as the number of panels increases. This proximity may cause numerical errors to accumulate, especially around sharp corners or edges on the aerodynamic body, leading to inaccuracies in the solution. Furthermore, the close vicinity of the sources and doublets may cause numerical instabilities to arise, thus affecting the accuracy of the solution even as the number of panels is increased. For these reasons, after developing the models for the wing and nacelle, a sensitivity analysis was conducted to ensure accurate integral and distributed loadings. The study was influenced by the need to obtain precise results for the propeller slipstream and flow field, which will be discussed in the next chapter. Initially, the analysis focused on the sectional lift coefficient in the spanwise direction, increasing the discretization from a minimum of 15 span panels to a maximum of 105, while keeping the chord discretization fixed at 40 panels.

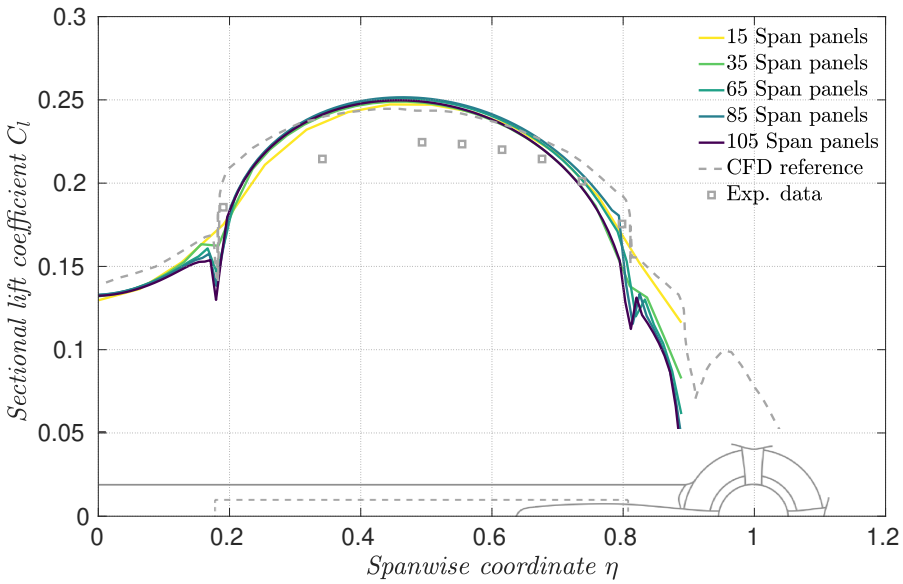

Figure 3.15: Sectional lift coefficient distribution c_l computed at $\alpha = 0°$ and $\delta_e = 10°$ varying the number of spanwise elements, from 15 to 105 elements while the chordwise discretization was kept fixed at 40 panels.

Fig. 3.15 clearly shows that there are some differences in the region where the nacelle is located, as this region is prone to viscous and non-linear flow behavior. However, the behavior between $0 \leq \eta \leq 0.8$ is accurately depicted, and DUST provides excellent results even with just 35 panels. Increasing the panelization over the span improves the transition between the plain section and the one with the flap. The vorticity shed from the flap side

edges ($\eta \approx 0.19$ and $\eta \approx 0.81$) causes a local steep reduction in the circulation of vortex shed, which was confirmed by the high fidelity CFD results. This phenomenon can be observed in Fig. 3.16.

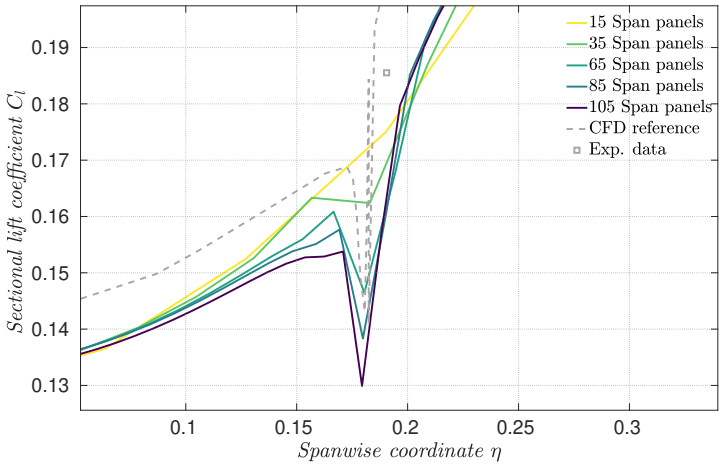

Figure 3.16: Zoom in the close vicinity region of the flap deflection.

As shown in Table 3.6, it is evident that panel methods do not always yield improved results when increasing the number of panels. This can be attributed to the mutual interaction between adjacent panels, leading to sources and doublets that may introduce numerical instabilities, in so doing compromising the solution accuracy despite an increase in panel count. Specifically, the error decreases with an increase in the number of spanwise panels up to 65, after which it begins to increase once again.

Wing Grid - Spanwise Sensitivity				
Case [-]	Spanwise elements [-]	time [s]	C_L [-]	ε_{C_L} [%]
1	15	1160	0.1963	1.85
2	25	1500	0.1969	1.55
3	35	1702	0.1965	1.75
4	45	2037	0.1968	1.60
5	65	2834	0.1985	0.75
6	85	4289	0.1984	0.80
7	105	5411	0.1977	1.15

Table 3.6: Grid sensitivity results for the spanwise elements of the wing. The time gives an estimation of how long has taken to reach convergence. The error ε_{C_L} [%] is considered in modulus w.r.t. the CFD value of $C_{L,CFD} = 0.200$ computed by Stokkermans et Al. [43].

Despite the possibility of selecting coarser panelization (for time-saving matters), 85 panels were chosen to ensure the flow field's accuracy and detail. This decision highlights the importance of prioritizing precision in the flow field, as it directly affects the propeller slipstream and flow field, which is essential in this study.

After having studied the spanwise case, the focus then turned to the chordwise elements of the wing. The chordwise panelization of the airfoil was analyzed in order to obtain a robust numerical model, with the chordwise pressure distribution and sectional loads serving as sensitivity indices. Figure 3.17 shows the pressure distribution at $\eta = 0.666$, indicating that increasing the number of panels improves the accuracy of the C_p pressure peaks corresponding to the flap deflection. Additionally, the two peaks show a tendency to shift towards the leading edge, resulting in a better approximation of the URANS CFD results of Stokkermans et al. in [43].

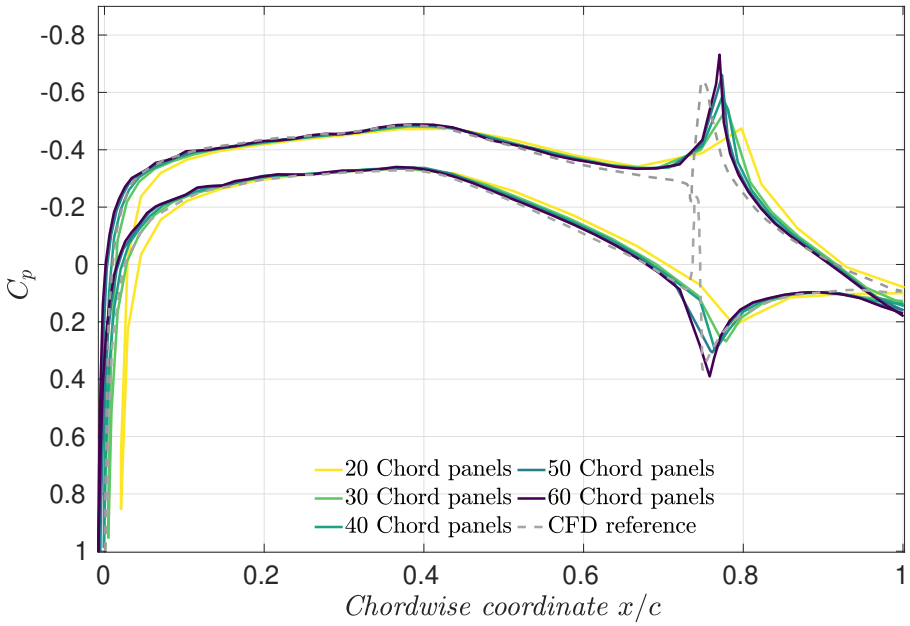

Figure 3.17: Pressure distribution at $\eta = 0.666$, $\alpha = 0°$ and $\delta_e = 10°$ with the propeller off - varying the chordwise elements, ranging from 20 to 60. The spanwise discretization was kept fixed at 30 panels. The URANS CFD reference was performed by Stokkermans et al. [43]

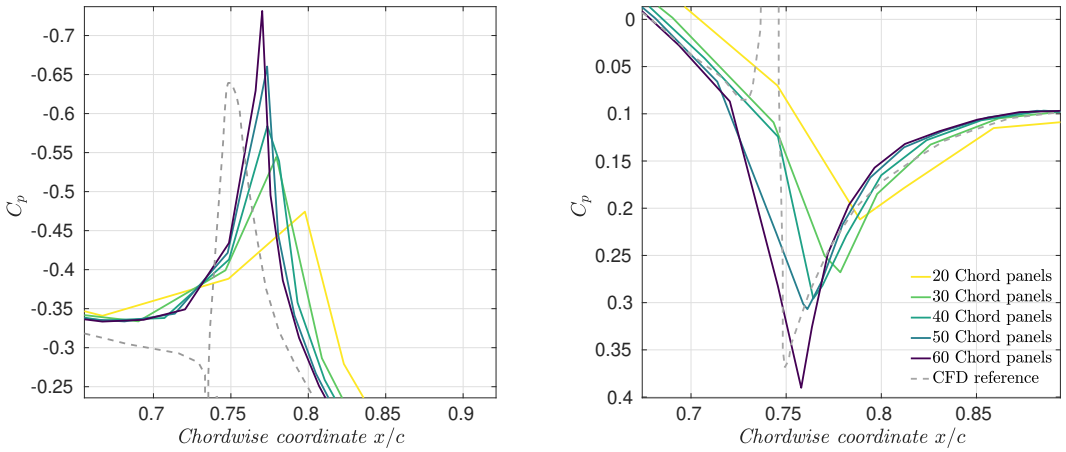

(a) Suction side peak (b) Pressure side peak

Figure 3.18: Zoom in the zones of interest - pressure coefficient distribution at $\eta = 0.666$, $\alpha = 0°$ and $\delta_e = 10°$ with the propeller off.

Based on the results presented in Table 3.7, it can be observed that the sectional lift coefficient at $\eta = 0.666$ is accurately computed with only 30 chord panels. Increasing the number of panels would result in improved accuracy in the flow field study and a more precise pressure peak in the flap deflection zone. However, this would also require a significant increase in computational effort.

Wing Grid - Chordwise Sensitivity				
Case [-]	Chordwise elements [-]	time [s]	$c_{l,666}$ [-]	$\varepsilon_{c_{l,666}}$ [%]
1	20	1407	0.1965	2.40
2	30	1835	0.1996	0.85
3	40	2258	0.1999	0.70
4	50	2726	0.2021	0.40
5	60	3799	0.2027	0.70

Table 3.7: Grid Sensitivity results for the chordwise elements of the wing, the $c_{l,666}$ is the sectional lift coefficient at $\eta = 0.666$. The time gives an estimation of how long each test case has taken to reach convergence. The error $\varepsilon_{c_{l,666}}$ [%] is considered in modulus w.r.t. experimental value of $c_{l,666} = 0.2013$ computed by Sinnige et Al. in [40].

However, it should be noted that excessive increase in the chordwise panel count can lead to nonphysical results, with the pressure peaks becoming increasingly similar to a Dirac delta function hence the increase in sectional loading (issue that is visible in Tab.3.7, where

after 40 elements the error start increasing again). This is attributed to the singularities in the region of the flap deflection, where adjacent panels show unbounded mutual interaction as they become progressively closer. Therefore, a balance between accurate positioning of the peak along the chord and a realistic pressure distribution was sought in determining the optimal chord panelization.

3.2.2. Validation of the DUST model for the isolated wing

After conducting a thorough study to optimize the panelization and model behavior, a brief validation has been performed to verify if the mutual aerodynamic influence between the nacelle and wing is correctly captured and to validate the wing loadings with CFD and experimental references.

The results depicted in Fig. 3.19 demonstrate that the sectional lift coefficient c_l is accurately predicted for $\eta \leq 0.8$, yielding good agreement with both experimental and CFD data from the works of Sinnige et al. [40] and Stokkermans et al. [43]. However, discrepancies in the nacelle region were expected due to the occurrence of large separations and complex flows, which are not appropriately captured by mid-fidelity codes such as DUST.

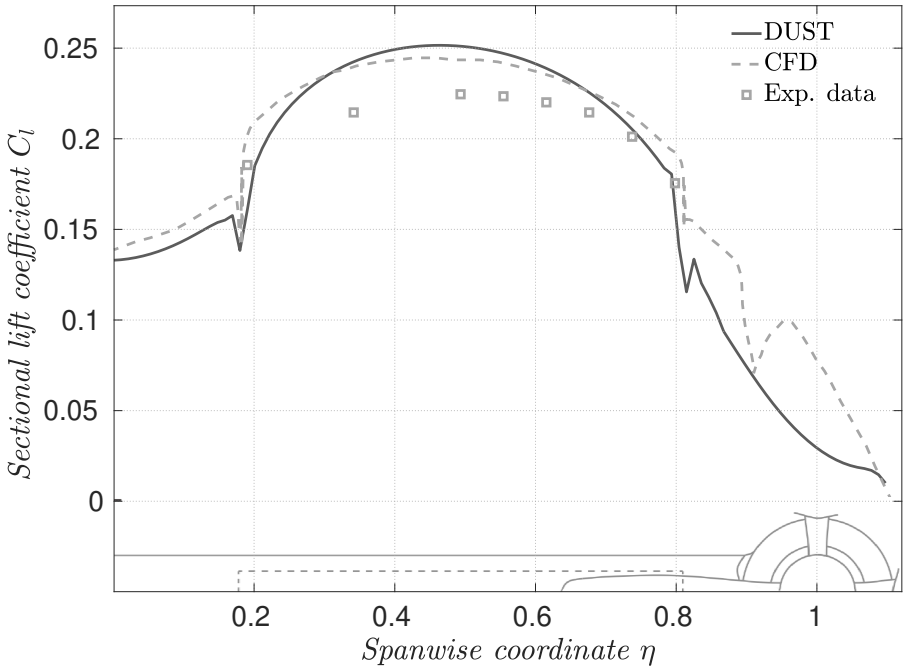

Figure 3.19: Sectional lift coefficient distribution at $\alpha = 0°$ and $\delta_e = 10°$ for the isolated wing with the propeller off.

It is crucial to emphasize that the influence of the nacelle on the wing + flap (and subsequently on the propeller) is of paramount importance for this study. Nonetheless, the primary objective was to obtain a satisfactory flow around bluff bodies where CFD codes or further tuning/tabulated data are necessary to achieve an accurate description. Continuing the analysis, the chordwise pressure distributions at two spanwise locations are presented: at the flap midspan and near the outboard flap edge, as shown in Fig. 3.20 and Fig. 3.21. The results demonstrate excellent agreement with experimental and CFD data along most of the profile's chord, with minor discrepancies observed in the trailing edge region where DUST predicts a lower pressure recovery. This outcome was expected since no turbulence model was implemented, and a flap deflection of $\delta_e = +10°$ inevitably leads to recirculation and separation. It is crucial to validate the results in areas that can be accurately captured by mid-fidelity codes and not to assume that they match the high-fidelity CFD output. Despite these limitations, the validation results are highly encouraging and provide further evidence that the DUST model accurately represents the test case. Therefore, it is regarded to be suitable for further studies.

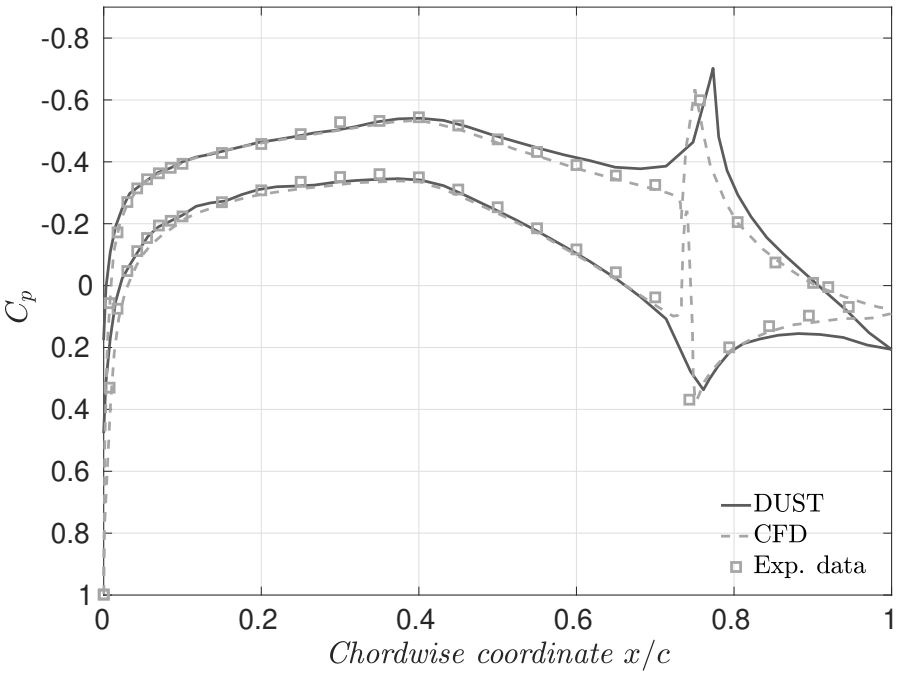

Figure 3.20: Pressure distribution at $\eta = 0.666$ (near the outboard flap edge) at $\alpha = 0°$ and $\delta_e = 10°$ for the isolated wing with the propeller off.

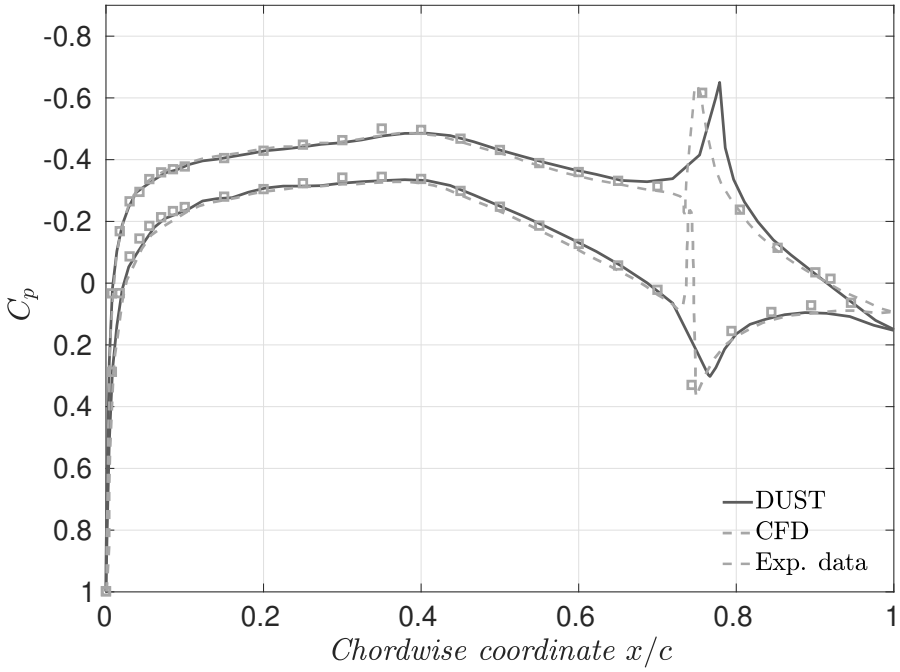

Figure 3.21: Pressure distribution at $\eta = 0.445$ (flap midspan) at $\alpha = 0°$ and $\delta_e = 10°$ for the isolated wing with the propeller off.

Tab. 3.8 presents the integral results, which are compared with CFD and experimental data. The results obtained with the DUST model are in great accordance with those obtained through CFD, with a relative error of only 1% between the two outputs. The more significant differences with the experimental results are due to the use of a transition strip at $x/c \approx 0.12$ in the experiments conducted by Sinnige et al. [40], which induced a forced transition.

C_L - Isolated wing configuration			
Configuration	**Model**	**C_L [-]**	**Error ε_{C_L} [%]**
Isolated wing	DUST	0.198	1.0
	CFD	0.200	-
	Experimental	0.189	5.5

Table 3.8: Lift coefficient C_L for the isolated wing configuration at $\alpha = 0°$ and $\delta_e = 10°$. The error ε_{C_L} is computed in modulus w.r.t. the CFD results computed by Stokkermans et al in [43].

4 | Results and discussion

4.1. Numerical setup

The simulations in this chapter were carried out using DUST, using the whole model including all of the components discussed and assessed in the previous chapter. The following parameters were utilized for these simulations:

Operating conditions						
α [°]	V_∞ $[m/s]$	J [-]	rps [rad/s]	δ_e [°]	time step dt [-]	Re [-]
0	40	0.8	1325	10	0.0000685	6.5×10^5

Table 4.1: Selected operating conditions.

The aerodynamic bodies in this study were modeled using a mesh of approximately 8000 elements composed of lifting lines for the propeller blades, panels for the wing with the flap, and TriElements for the nacelle's unstructured grid, as well as 50000 particles for the propeller and wing wakes. Grid independence studies for the wing were carried out in Section 3.2.1 resulting in the selection of 85 spanwise and 45 chordwise elements, for a total of 3400 elements. A grid refinement was applied at the beginning of the deflection to capture the flow surrounding the sudden fluctuation in flap deflection. The total number of panels was slightly larger than indicated due to the panelization of the wing extension required for modeling the wall. The mesh for this part, on the other hand, was kept relatively coarse because merely its effect upon the real model's was necessary, and great precision was not required. The mesh for the wing-tip propeller and nacelle is shown in the table below:

Grid resolution				
Wing elements	Propeller elements	Nacelle elements	Wake particles	Wake panels
3825	34	4126	50000	3

Table 4.2: Grid resolution.

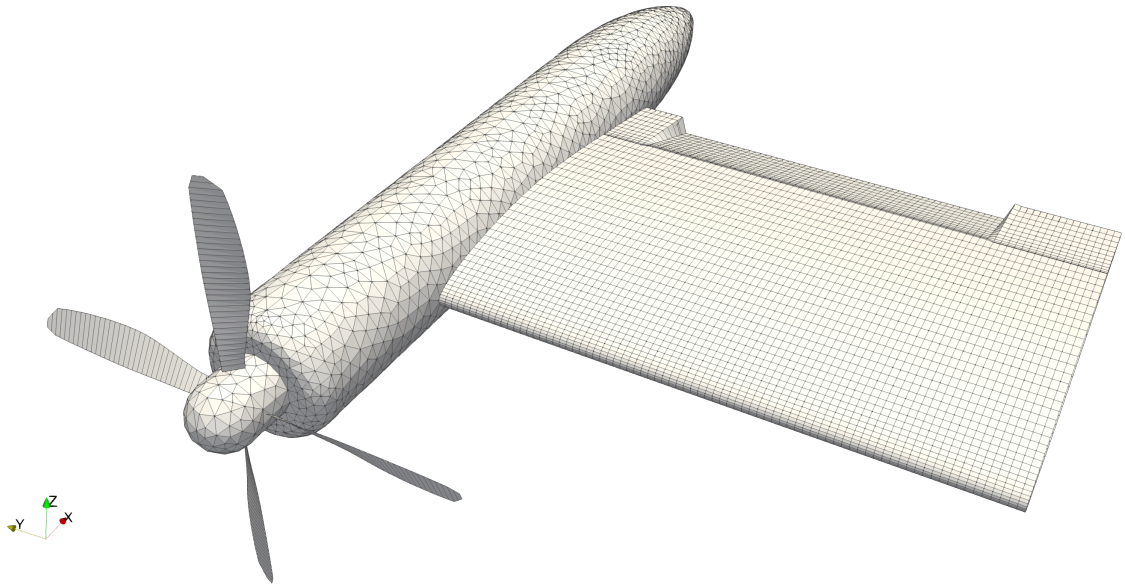

Figure 4.1: Visualization of the DUST mesh for the complete model.

The findings presented in this chapter are based on the extensive research conducted by Nando Van Arnhen, Tomas Sinnige, Tom C. A. Stokkermans, and Leo Veldhuis, as documented in their published works [40, 41, 43, 46]. These researchers conducted a comprehensive analysis of the test case using high-fidelity CFD simulations and experimental wind tunnel testing, providing a solid foundation for the validation of the results.

4.2. Propeller slipstream flow characteristics

The accurate description of the interactive flow phenomena around a propeller wing configuration requires a detailed understanding of the slipstream characteristics in the presence of the nacelle and mounted wing. In this regard, after the investigation of the propeller's individual characteristics and validation in Section 3.1, here the propeller is mounted on the complete model and a comprehensive study is performed on some of the most significant flow quantities characterizing the propeller slipstream, such as:

1. axial velocity profile
2. swirl velocity profile
3. swirl angle
4. vorticity distribution

5. vortex development

The local velocity vector in the three-dimensional space is composed of three components, $\vec{u} = (u, v, w)^t$, in a Cartesian coordinate system. In the current investigation, the propeller's direction is aligned with the streamwise x-direction, and thus the x-component u represents the axial velocity. Due to the non-uniform radial loading, a strong gradient exists in the blade's spanwise direction, with a maximum found near the 3/4 R location. The lower u-value near the blade root is a result of the relative low blade loading due to the reduced velocity experienced by the propeller in this region, leading to a more complex flow development characterized by large separation and turbulent motion.

From Figure 4.2 and Figure 4.3 it is clear that DUST offers good physical results in the slipstream region of the propeller, correctly capturing the expansion zones of the nacelles and its influence over the high energized flow in the propeller slipstream.

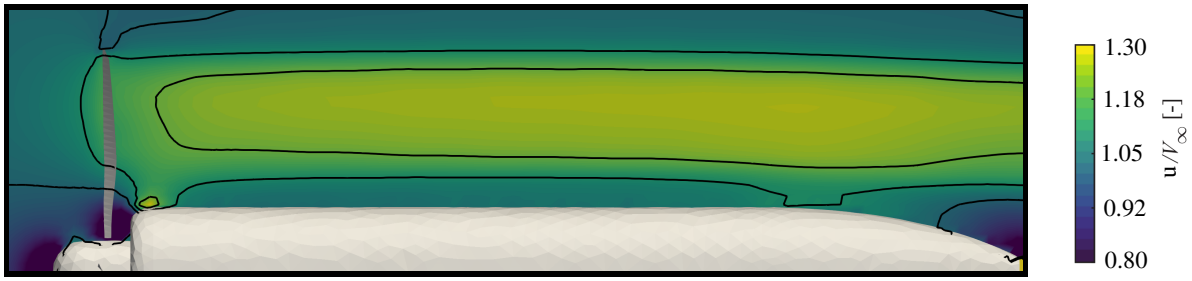

Figure 4.2: Time-averaged normalized axial velocity flowfield with contours of velocity.

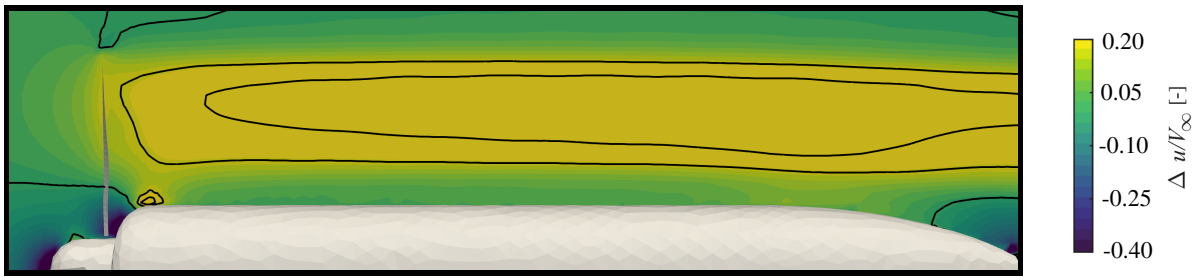

Figure 4.3: Time-averaged normalized delta-axial velocity flowfield with contours of velocity.

To understand the distribution of the propeller-induced tangential velocity component :

$$v_t = \sqrt{(v^2 + w^2)} \tag{4.1}$$

Is important to consider some key assumptions; Firstly, it is assumed that the propeller has an infinite number of blades, and therefore, the slipstream behind it is filled with

streamlines. Based on this model, it is found that the bound vortices, which are attached to the propeller blades, do not induce any axial velocity in the slipstream, and these vortex lines have equal magnitudes but opposite directions. By considering the effects of all vortex pairs that make up the complete bound vortex system, it can be concluded that the axial induced flow velocity results from only the free trailing vortex lines in the slipstream. However, the tangential velocity induced by the bound vortices attached to the propeller blades at a given point P inside the slipstream is different but has the same direction. This means that the tangential velocity has the same direction as the propeller's sense of rotation and is often referred to as the "swirl velocity."

Figure 4.4 displays a cross-section of the region where the maximum swirl velocity occurs. The results are presented alongside with the corresponding ones obtained from CFD simulations which are exploited in [43]. The results demonstrate a good level of agreement with some differences noted in the root and tip regions. Despite these discrepancies, they are negligible in magnitude, thus the primary goal of obtaining comparable behaviour is achieved.

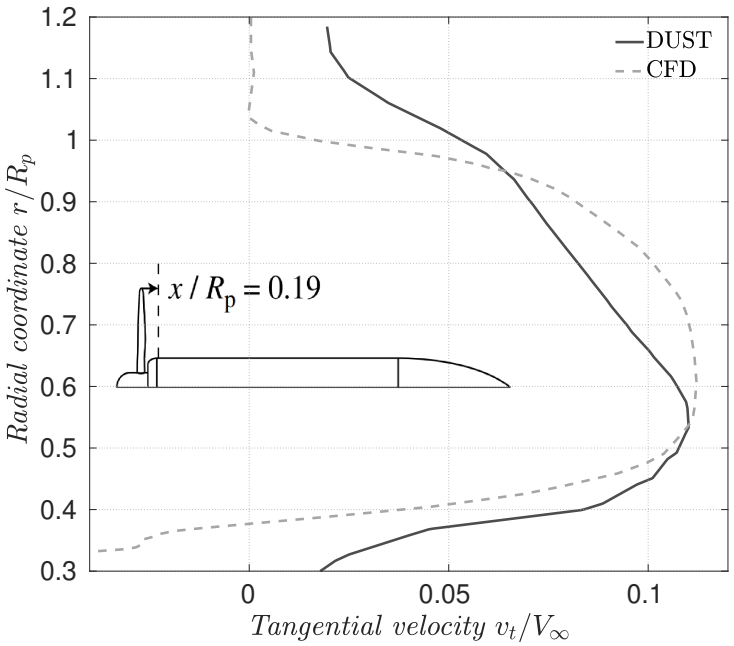

Figure 4.4: Time-averaged tangential velocity at $x/R_p = 0.19$ downstream.

The swirl angle is defined as:

$$\phi = \tan^{-1}\left(\frac{v_t}{u}\right) \tag{4.2}$$

The evolution of the swirl angle is a key factor in understanding the interaction between a

propeller and the nacelle. While the swirl velocity may remain constant, the swirl angle is influenced by the axial velocity, hence it changes in axial direction. The propeller swirl is confined just into the slipstream and in contrast to the axial velocity, the maximum swirl occurs just downstream the radius. Figure 4.5 shows that the swirl angle experiences only a slight reduction when compared to the distribution just downstream of the propeller.

Furthermore, the shape of the swirl angle distribution remains approximately constant. Notably, the most significant deviation occurs when the nacelle contracts. As angular momentum must be conserved, the tapering of the nacelle causes an increase in swirl velocity, resulting in a substantial swirl angle on the center-line. This effect is further amplified by the reduced axial component of the separated flow from the nacelle.

The regions where the swirl angle has the highest values correspond to regions where DUST fails to provide accurate results due to high gradients that result in separation. Thus, these areas will not be examined in detail. However, the slipstream flow is well-represented throughout the slipstream region and exhibits a clear physical significance, which closely aligns with the patterns identified in prior works by Van Arnhen et al. [41].

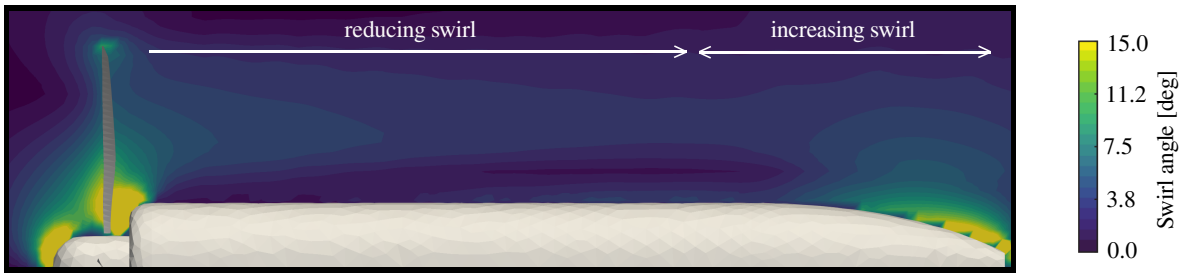

Figure 4.5: Time-averaged swirl angle ϕ.

After examining time-averaged quantities, it is now necessary to consider instantaneous ones (phase-locked). The flow downstream of the propeller is highly unsteady, with vortices that deeply alter the flow field. This aspect was not captured in the previous time-averaged studies, which nonetheless provided strong physical validation of the DUST output.

The associated instantaneous flowfield obtained in DUST is compared with high fidelity results coming from CFD URANS simulations of Stokkermans et Al. [43], the results are presented in Figure 4.6. The hub region contributes majorly to the unsteadiness, while the wake is thin in the region of highest loading, and the flowfield induced by the propeller can be described dominantly by potential flow [45]. The axial velocity outside the slipstream also varies significantly, owing to the presence of tip vortices. The tip

vortices introduce the largest gradients in the flowfield, leading to fluctuations of more than 50% of the freestream velocity. Regions with high gradients, such as the vicinity of the tip-vortex region and the blade wakes, show fluctuation concentrated in the spatial direction, leading to sudden changes in the flowfield. Furthermore, the fluctuations in flowfield quantities vary significantly in the radial direction, while their dependence on the axial location is limited.

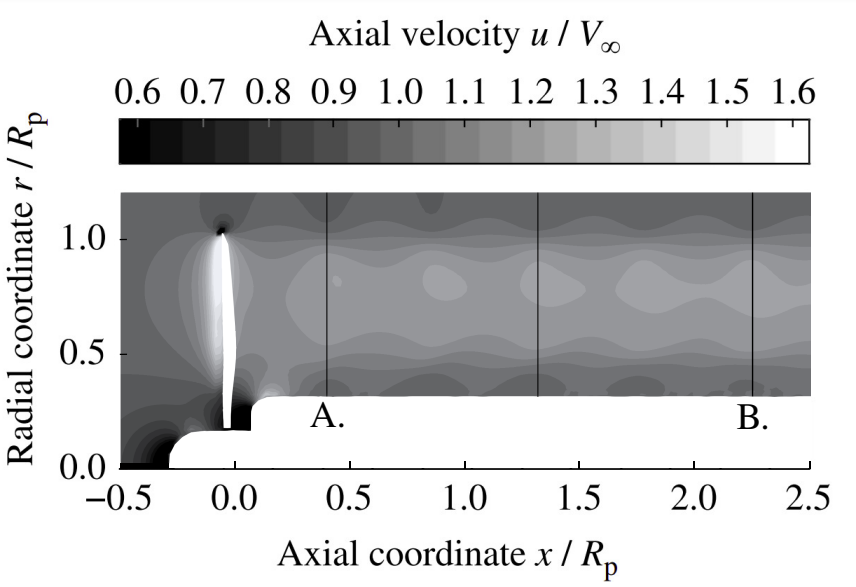

(a) **DUST**

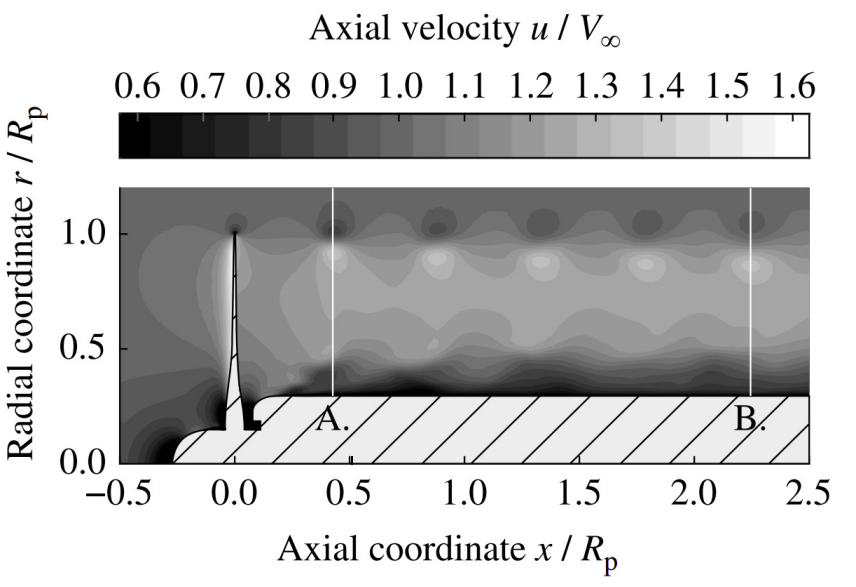

(b) **CFD** [43]

Figure 4.6: Axial-radial contour plots of phase-locked axial velocity.

The comparison with the flowfield results to those obtained from CFD, indicates a high degree of similarity, although some differences exist between the two. Specifically, the vortices captured by DUST are less sharp and have less pronounced gradients in their cores compared to those produced by CFD. Additionally, the boundary layer region near the wall, where the flow velocity rapidly decreases, is not modeled in DUST, resulting in a less significant reduction of axial velocity than in the CFD case. Nonetheless, DUST is able to capture the overall flow development and patterns, with better results obtained in regions closer to its intended application, particularly in the range of $0.3 \leq r/R_P \leq 0.8$. To give more insight to this, normal flow-orthogonal slices centered in three different tip vortices location has been extrapolated, the results are visible in Fig. 4.7 Here the axial non-dimensional velocity is reported along the second and fourth tip vortices. The accuracy of DUST's results is demonstrated in the mid-region $0.5 \leq r/R_P \leq 0.9$, where it closely matches the CFD and slightly underpredicts the experiments of Sinnige et al [40]. However, DUST underpredicts the velocity in the inboard section $r/R_P \leq 0.5$, and the tip vortices are slightly shifted inboard due to the omission of flow blockage caused by the mounting pod. Furthermore, DUST has less accuracy in resolving the tip vortices, resulting in less sharp depiction of instantaneous quantities with large gradients, as observed from the velocity peaks near $r/R_P \approx 1$. Stokkermans et al. [43] also noted that mesh-based CFD has numerical dissipation, which makes it computationally unfeasible to fully resolve the tip vortices. In contrast, DUST's low numerical dissipation enables a coarser resolution of the vortical structure with minimal computational effort, at the expense of losing some detail in the root and tip regions.

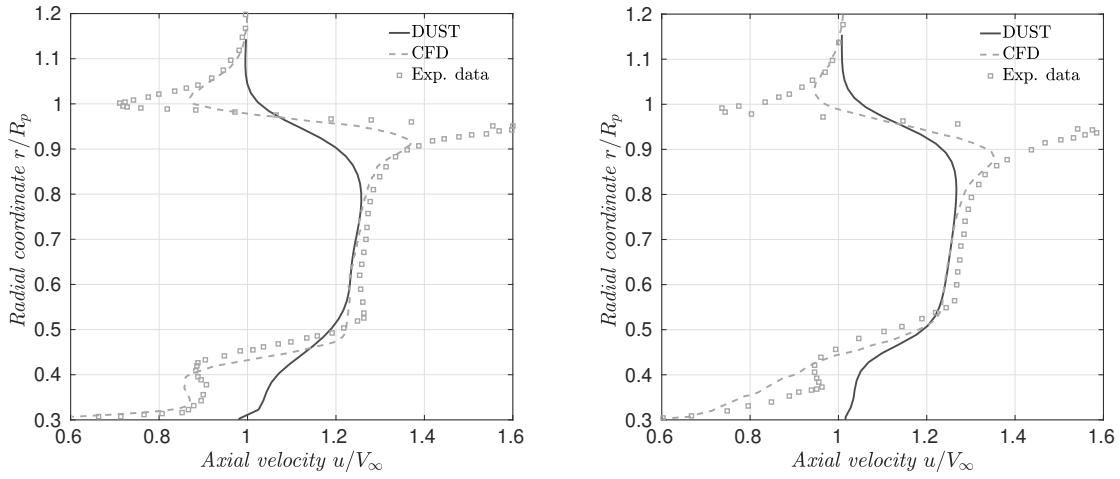

(a) **A** - Second tip vortex

(b) **B** - Fourth tip vortex

Figure 4.7: Instantaneous radial profiles, The URANS CFD reference was performed by Stokkermans et al. [43]

As the slipstream moves downstream, the vortex impingement becomes less pronounced, and the DUST instantaneous axial velocity prediction improves, matching the CFD case more closely, as shown in Figure 4.8, where the two curves are much more similar, even in the tip region.

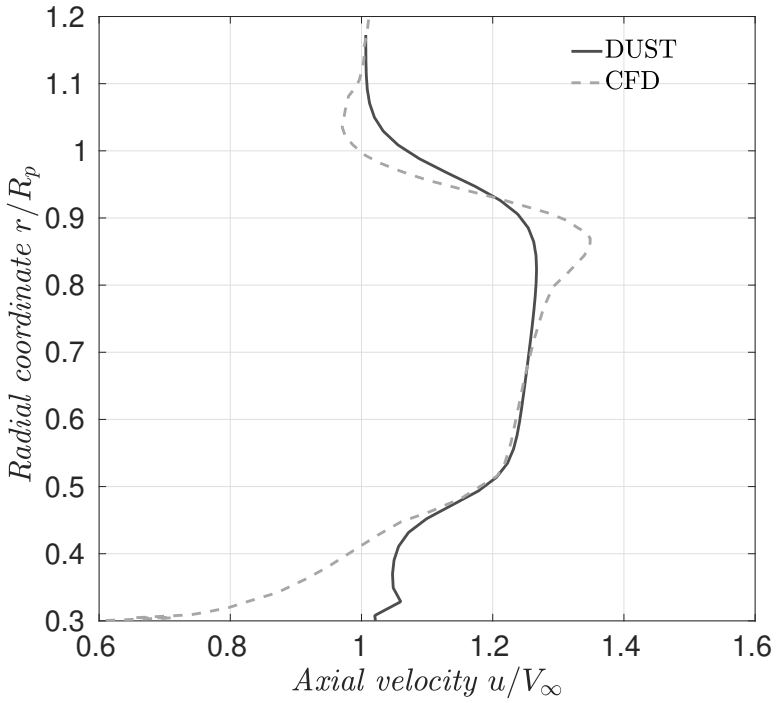

Figure 4.8: Sixth tip vortex. The URANS CFD reference was performed by Van Stokkermans et al. [43]

4.3. Upstream Interaction: propeller's forces after the installation

Looking at Fig. 4.9 it is clear that the isolated propeller, the thrust distribution remains constant along the radial coordinate, except in the hub region where separation is expected to occur due to the circular propeller section at the root region ($r/R_p \leq 0.4$). In the installed configuration, the thrust distribution resembles the one of the isolated case up until $r/R_p \leq 0.6$, then the loading on the blade increases due to non-uniform inflow caused by the presence of the wing and nacelle. The application of an elevator deflection of $\delta_e = +10°$ results in an increase of approximately 9.4% in the time-averaged C_T value, passing from 0.096 to 0.105. This increase is aligned with the CFD prevision done by Van Arnhem [41] which found a 7.6% increase in C_T. This increase is directly related to

a locally different axial velocity and angle of attack compared to freestream conditions, both of which are induced by the presence of the wing.

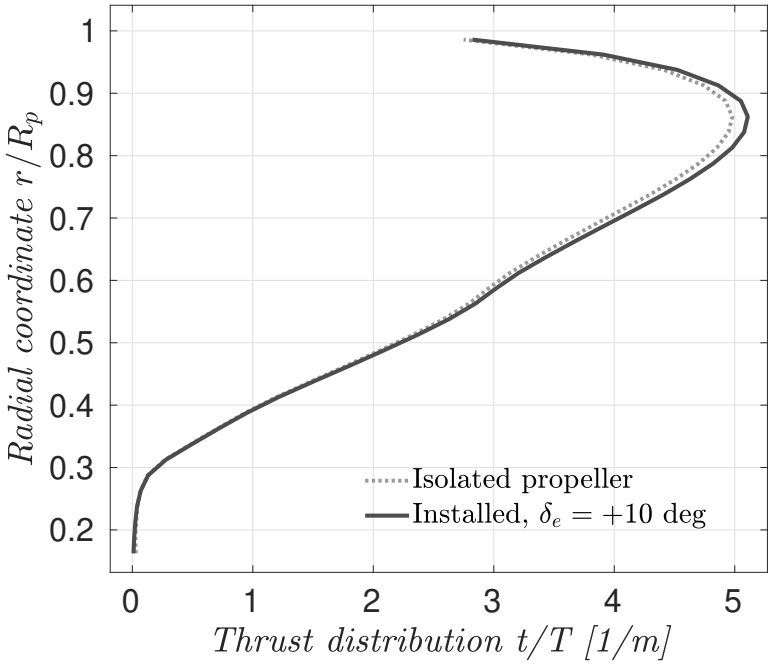

Figure 4.9: Radial thrust distribution for the propeller computed with DUST, installed, $\delta_e = +10$ deg versus isolated configurations.

A time-averaged (over the last full rotation) azimuthal thrust distribution contours for elevator deflections of $\delta_e = +10°$ are shown in Fig. 4.10 which tries to explain this enhancement in thrust once the propeller is installed. The contours reveal that a positive elevator deflection leads to an increase in thrust contribution in the region where the propeller blades are near the wing's leading edge, i.e., $\psi = 0°$. In this region, the wing blockage and the net upwash caused by the wing bound vortex and the trailing vortex system result in an upstream effect. The upwash is in the same direction as the propeller's rotation direction, thereby reducing the local angle of attack of the blade sections. It is thought that the increase in thrust is primarily due to the locally reduced axial velocity caused by blockage from the wing, which results in a decreased effective advance ratio for the blade sections. At $\psi = 90°$ and $\psi = 270°$, the loading is mainly influenced by the wing bound vortex shed by the nacelle. On the pressure side of the wing ($\psi = 90°$), there is a local reduction of inflow velocity to the propeller, while on the wing suction side there is an increase in inflow ($\psi = 270°$), leading to an increase in propeller loading in this region.

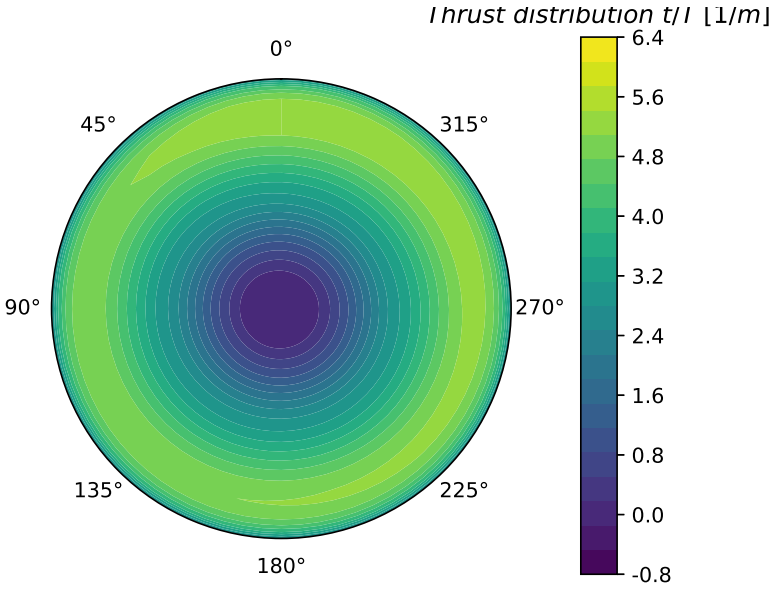

Figure 4.10: Time-averaged azimuthal thrust distribution computed with DUST.

Figure 4.11 shows the CFD results of time-averaged azimuthal thrust distribution obtained at the same operating conditions as the one considered in the DUST case for reference. [45] The comparison reveals an excellent agreement, in so doing providing robust validation for the present study.

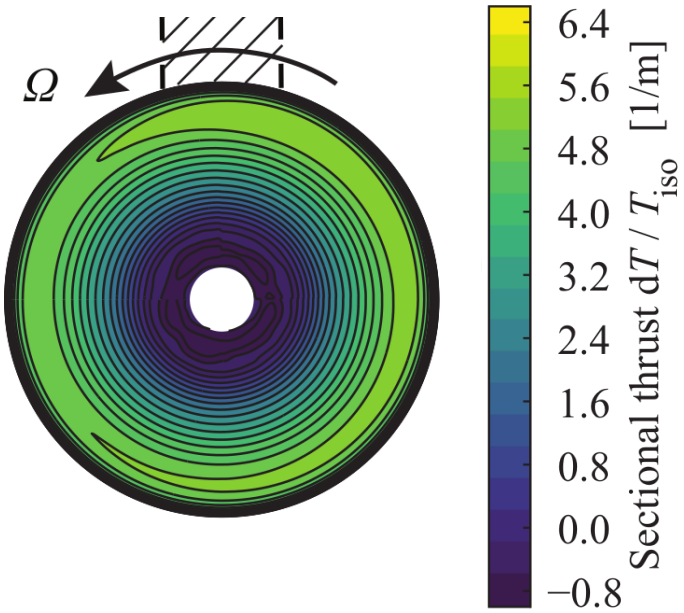

Figure 4.11: Time-averaged azimuthal thrust distribution computed with URANS CFD by Van Arnhem in [45].

C_T - Propeller integration effects				
Configuration	**Model**	C_T **[-]**	ε_{C_T} **[%]**	C_T **gain [%]**
Isolated propeller	DUST	0.096	2.9	-
	CFD	0.091	3.0	-
	Experimental	0.094	-	-
Installed propeller	DUST	0.105	8.6	+9.4
	CFD	0.098	2.1	+7.6
	Experimental	0.096	-	+2.2

Table 4.3: Effects on the thrust coefficient C_T arising from the integration of the propeller into the airframe at $\alpha = 0°$ and $\delta_e = 10°$. The error ε_{C_T} is computed in modulus w.r.t. the experimental data computed by Sinnige et al in [40].

Table 4.3 shows the impact of propeller integration on the airframe, specifically on the thrust coefficient C_T. It is observed that the results from both DUST and CFD simulations for an isolated propeller are in close agreement, although overestimating experimental results by a 3% margin. The significant differences with the experimental results are due to the use of a transition strip at $x/c \approx 0.12$ in the experiments conducted by Sinnige et al. [40], which induced a forced transition. When the propeller is integrated with the hub, wing and nacelle, DUST effectively captures the performance enhancements resulting from the integration, but overestimates these benefits when compared to CFD and experimental data. Nonetheless, the results obtained through DUST are still acceptable for preliminary design stages, where the difference between high-fidelity and mid-fidelity simulations is approximately 7% and 8.6% for experiments. Furthermore, DUST accurately predicts the percentage gain in C_T following the propeller installation, demonstrating a performance increase of +9.4% with respect to the isolated condition, compared to +7.6% obtained from CFD.

4.4. Propeller installation influence on the wing loads

Figures 4.12 and 4.13 displays the complete model at $\alpha = 0°$ with a flap deflection of $\delta_e = +10°$ and a propulsive advance ratio of $J = 0.8$. Analysis of the pressure distribution over the wing indicates that the slipstream of the propeller induces differences in the wing loadings, resulting in upwash and a local increase in lift compared to the propeller-off case. The slipstream effect of the propeller over the wing decreases rapidly when moving away from the slipstream, leading to a smaller interactional effect.

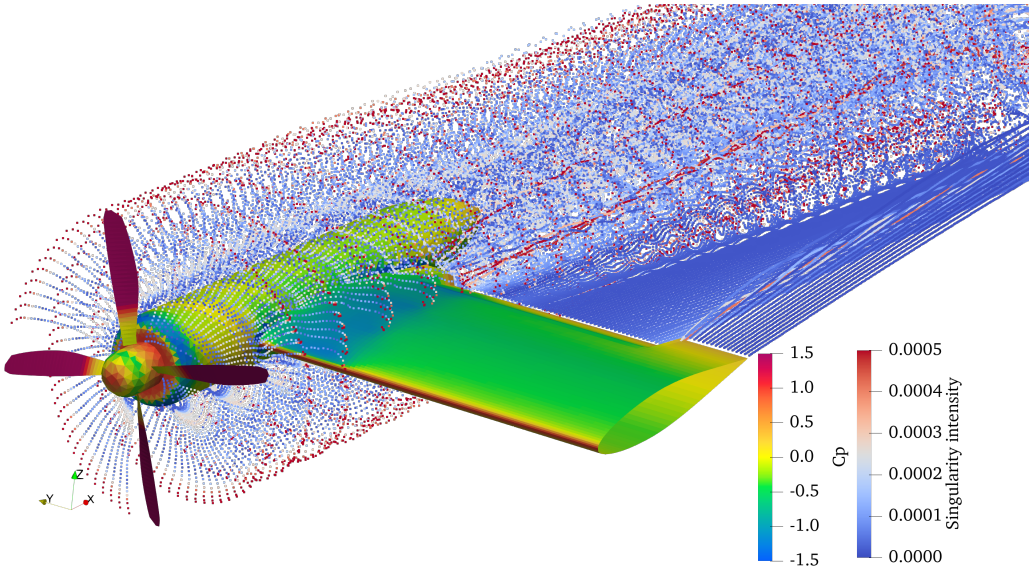

Figure 4.12: Flow visualization at $\delta_e = +10°, \alpha = 0°$ and $J = 0.8$.

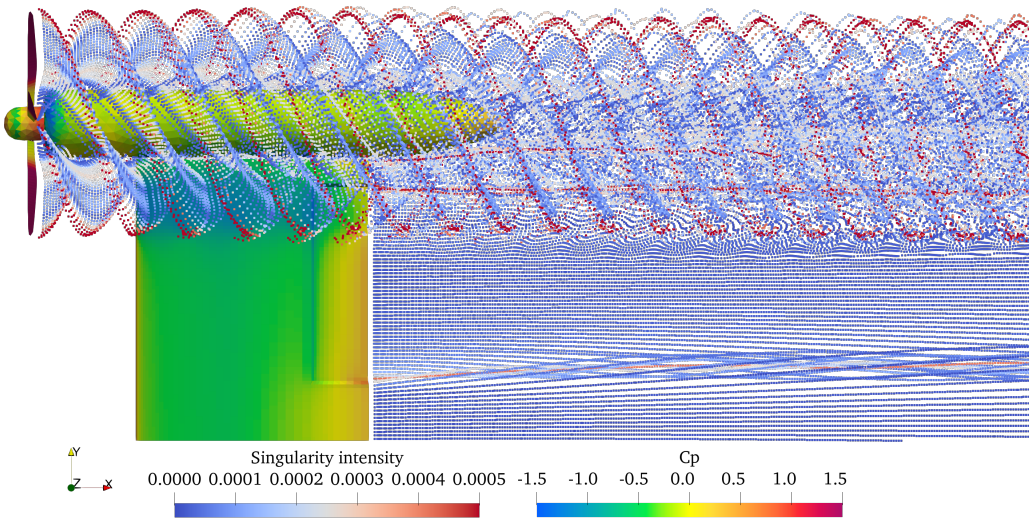

Figure 4.13: Flow visualization at $\delta_e = +10°, \alpha = 0°$ and $J = 0.8$.

Figure 4.14 shows that the wing's lift increasing with inboard-up rotation due to the interaction with the propeller slipstream. This phenomenon is attributed to the difference in upwash experienced by the wing, as illustrated in Fig. 4.15. The results obtained from DUST are in agreement with those obtained from CFD for nearly all spanwise coordinate values η. As described in Sec. 3.2.1, the wing wall was modeled by extending the wing span in the root region and modifying its camber through a 25% chord flap. This modification resulted in a positive C_L even for a null angle of incidence. The effects of the propeller inboard-up rotation are visible between $0.6 \leq \eta \leq 0.8$ and are consistent with those obtained from CFD and experiments.

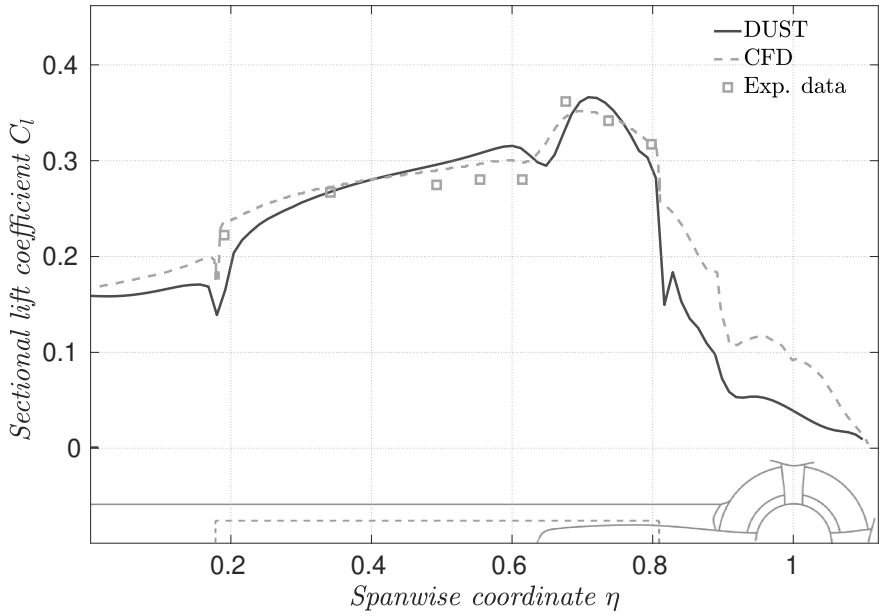

Figure 4.14: Sectional lift coefficient distribution at $\alpha = 0°$ and $\delta_e = 10°$ for the complete model with the propeller on.

The maximum sectional lift is almost identical and slightly shifted outboards, while the DUST prediction for the lift coefficient over the flap deflection zone has a steeper increase compared to the CFD and experimental data. The tip vortices resulting from the junction between the wing and the flap at $\eta = 0.18$ and $\eta = 0.81$ are visible, but they are overestimated. In fact, a steep drop in lift coefficient is observed in those zones. The results for the nacelle are unsatisfactory, although the zero circulation at the tip is preserved. The values are obtained through post-processing extrapolation since DUST cannot provide the sectional loads of bluff bodies as output. However, the main focus of this study is not the flow around the nacelle, where significant discrepancies were expected due to recirculatory motions and highly turbulent flow. Instead, the main goal was obtaining a

good agreement in the wing region $0 \leq \eta \leq 0.9$. The excellent matching between DUST results and CFD/Experimental data demonstrated that the model and the mid-fidelity code can efficiently capture vortex interaction due to flap deflection and the propeller flow field's influence. Therefore, these findings represent a further validation of the model.

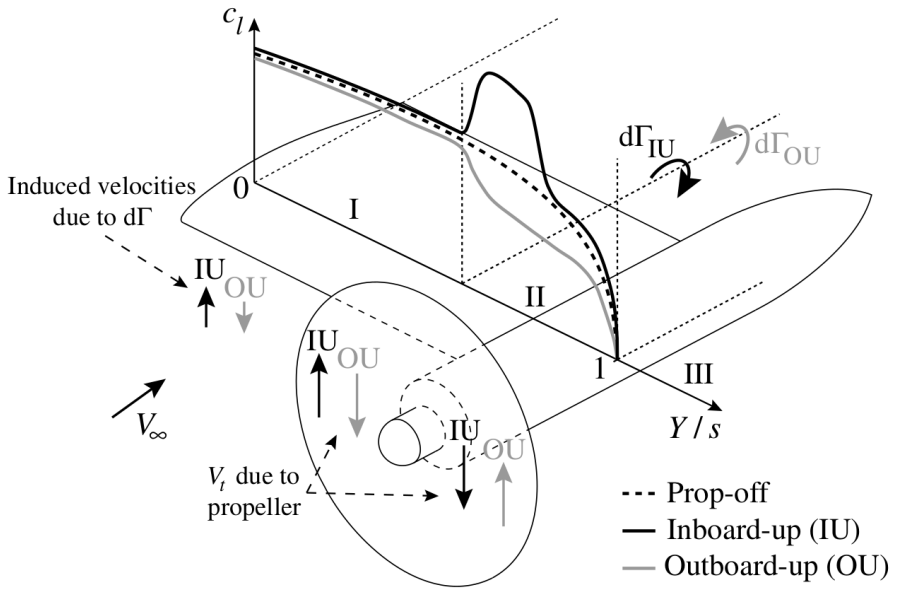

Figure 4.15: Sectional lift distribution modification due to propeller installation. [40]

In the inboard-up rotation case considered in this thesis, the wing experiences higher upwash and dynamic pressure on the spanwise part washed by the slipstream (region II in Fig. 4.15), which enhances the lift compared to the propeller-off case. (see Fig.4.16). On the other hand, with outboard-up rotation, the direction of the propeller swirl is inverted, causing a downwash contribution to the local wing inflow and a resulting reduction in lift compared to the propeller-off case. The interaction effects are more pronounced at higher propeller thrust settings due to the associated increase in swirl and dynamic pressure induced by the propeller. With the propeller on, a steep lift gradient occurs around the slipstream boundary ($\eta \approx 0.6$), leading to vorticity shedding and a modification of the inflow angle on the spanwise part of the wing not immersed in the propeller slipstream (region I in Fig. 4.15). In particular, an upwash occurs with inboard-up rotation, resulting in a local lift increase with inboard-up rotation compared to the propeller-off case, as shown in Fig.4.16, where the prop-off and prop-on conditions are compared and validated.

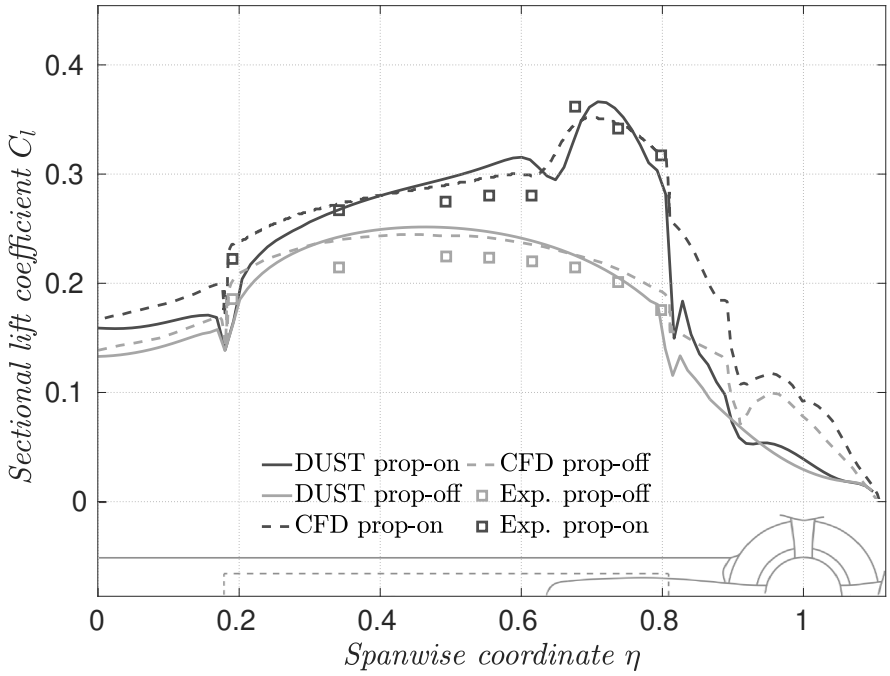

Figure 4.16: Sectional lift coefficient distribution at $\alpha = 0°$ and $\delta_e = 10°$ for the complete model with the propeller on and off.

The spanwise lift gradient becomes steeper with increasing thrust setting, leading to further vorticity shedding and spanwise velocities that distort the propeller slipstream during and after its interaction with the wing [16, 38, 48]. As a result, the local wing performance near the slipstream edge is modified by the spanwise shearing of the slipstream. The increase in lift due to the slipstream interaction with inboard-up rotation (Fig. 4.16) is mainly attributed to an increase in loading on the front part of the profile, which becomes more pronounced with increasing thrust setting. Table 4.4 presents the impact of propeller integration on the airframe lift coefficient C_L. The results obtained from DUST are compared to CFD and experimental data. In the isolated wing test case, DUST shows a good agreement with CFD, predicting the system lift coefficient with just a 1% error between the two outputs. The more significant differences with the experimental results are due to the use of a transition strip at $x/c \approx 0.12$ in the experiments conducted by Sinnige et al. [40], which induced a forced transition.

When the propeller is installed, there is a noticeable lift enhancement, as can be seen in Figure 4.16. The integral results of the system lift coefficients confirm this finding. Nevertheless, DUST underestimates both the CFD and experimental results by 5.4% and 8.6%, respectively. This is because DUST fails to accurately capture the nacelle

C_L - Propeller integration effects				
Configuration	**Model**	C_L **[-]**	ε_{C_L} **[%]**	C_L **gain [%]**
Isolated wing	DUST	0.198	1.0	-
	CFD	0.200	-	-
	Experimental	0.189	5.5	-
Wing with installed propeller	DUST	0.244	5.4	+23.3
	CFD	0.259	-	+29.5
	Experimental	0.257	0.8	+36.0

Table 4.4: Effects on the system lift coefficient C_L arising from the integration of the propeller into the airframe at $\alpha = 0°$ and $\delta_e = 10°$. The error ε_{C_L} is computed in modulus w.r.t. the CFD data computed by Stokkermans et al in [43].

contribution to the system lift coefficient. The discrepancies in the nacelle zone, as seen in Figure 4.16, introduce inaccuracies in the predictions due to recirculation and turbulent flow not being correctly captured by DUST. Despite these limitations, DUST is able to correctly capture the beneficial effect of installing a propeller in wingtip configuration on the airframe, resulting in a +23.3% gain in C_L, which is close to the +29.5% obtained from high-fidelity CFD studies. A more accurate modeling of the nacelle would result in a more precise output, potentially matching the high-fidelity output even more closely.

This beneficial effect arising when the propeller is installed into the airframe is further demonstrated by the pressure distributions provided in Fig. **??** and **??**, which show the results for the pressure distributions, measured and computed, on the model at two different spanwise locations: one at the edge of the propeller slipstream and a second outside the propeller slipstream at J=0.8.

The pressure distribution near the outboard flap edge in Fig. 4.17 reveals the time-averaged effect of the propeller slipstream on the wing loading, as well as the impact of the flap deflection direction. In comparison to the isolated wing case presented in dashed lines in Fig. 4.17, a suction peak near the leading edge appears as a result of the combination of the dynamic pressure rise and swirl in the slipstream. The pressure coefficient at the stagnation point is greater than unity ($C_{P,stag} = 1.5$) due to the section's location in the slipstream, while the freestream dynamic pressure is utilized to determine the pressure coefficient. [43] The DUST output, measurements, and CFD results show good agreement. the largest fluctuations are on the retreating side of the main element, the DUST simulations gives a time-accurate pressure distribution showing a wave-like pattern of increased negative pressure on the suction side of the wing indicating the propeller blade tip vortices' passage. A suction peak is evident in the pressure distribution on both sides of the airfoil at each tip-vortex core, and these suction peaks' locations and

magnitudes match well with the CFD models, confirming the helical tip-vortex system. The vortex shedding from the propeller weakens as it moves away from the propeller and along the slipstream this is seen by the fact that these pressure fluctuations become less pronounced downstream. To get a better understanding and visual representation of these vortices, an iso-surface plot of axial vorticity will be presented later to illustrate the vortices responsible for these fluctuations.

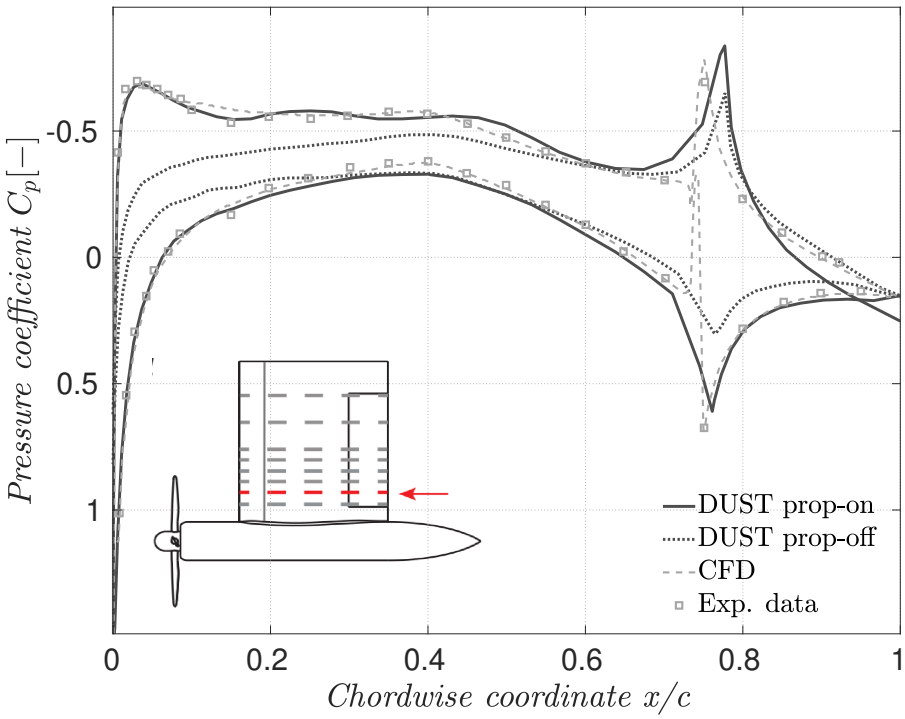

Figure 4.17: Pressure distribution at $\eta = 0.666$, inside the propeller slipstream at $\alpha = 0°$ and $\delta_e = 10°$ with the propeller on.

Moving outside the slipstream of the propeller the peak in the suction side of the wing disappears and no vortical phenomena is present, however the overall area between the lower and upper C_p distribution increases, so the propeller effectively enhances the loading of the wing even in the zones not directly affected by the slipstream. In both situations the peak at $x/c \approx 0.75$ results to be slightly moved backwards towards the trailing edge but as was seen in the grid convergence study, increasing even more the chordwise panelization this inaccuracy could be mitigated. In order to achieve a more accurate simulation of the flow, a high level of attention was paid to a known issue where the curves did not match at the trailing edge. This problem was tackled by considering the rotational speed of the propeller to define the temporal discretization of the simulation. To ensure reasonable detail, a large number of steps were considered for each propeller revolution ($N_{step} = 72$),

resulting in an extremely low time step value (dt=0.0000658). However, using such a fast time step for the wing led to an ill-conditioned first wake panel in DUST, which has a fixed time step for all components.

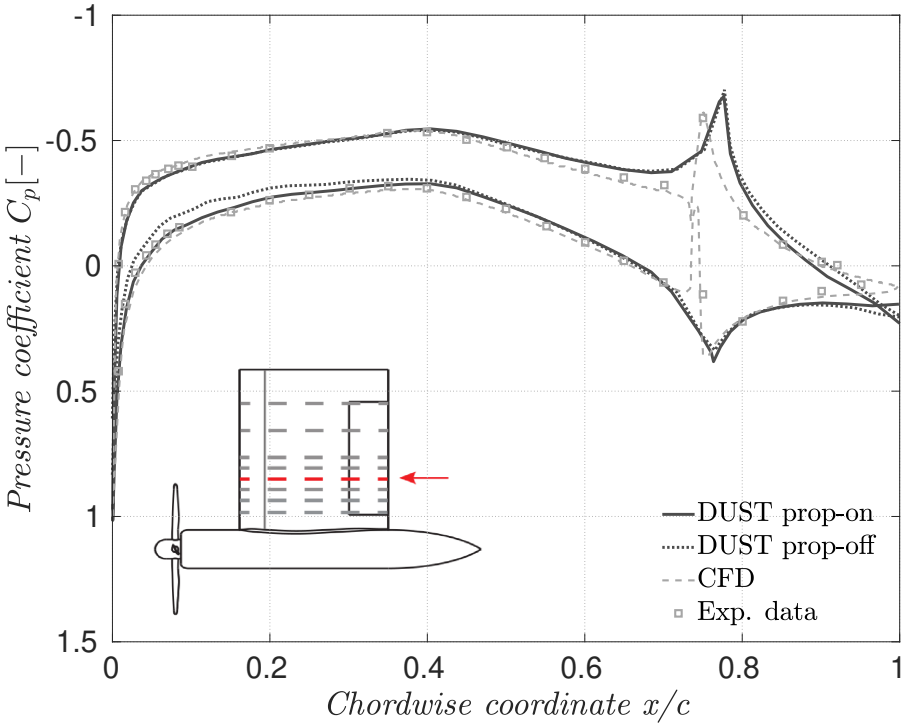

Figure 4.18: Pressure distribution at $\eta = 0.445$, outside the propeller slipstream at $\alpha = 0°$ and $\delta_e = 10°$ with the propeller on.

To address this issue, an iterative scheme was developed to modify the solution and ensure pressure equality at the wing trailing edge. It was also found that an explicit unsteady pressure Kutta condition was required in this particular unsteady-flow with fast time step.

It should be noted that the wake development for lifting surface modeled with panel method is not time-stepping independent and it is a zero-order model, leading to poor accuracy in complex cases such as this one where extremely fast time steps are present. Therefore, an initial approach to solve this issue and make the panelization time independent is presented in the Appendix A. This approach involves the definition of a first-order panel method, where the first panel in the wake is represented by a linear rather than a constant dipole distribution. This has been introduced in other panel method-based programs and has shown good results.

4.5. Interaction between propeller slipstream and wing-tip Vortex

To illustrate the distribution of axial vorticity ω_x in the slipstream, a schematic of axial vorticity of the complete model is shown in Fig. 4.19. The flowfield displays both positive and negative ω_x in the inner region of the slipstream. The positive ω_x is generated by the wing tip and the outboard edge of the elevator, while the negative ω_x is produced by the propeller hub vortices. For positive elevator deflection, all axial vorticity in the inner region is aligned in the same direction, explaining the higher average swirl angle. The contrasting vorticity signs will also be evident in the upcoming Q-criterion iso-surface of axial vorticity ω_x in Section 4.6.

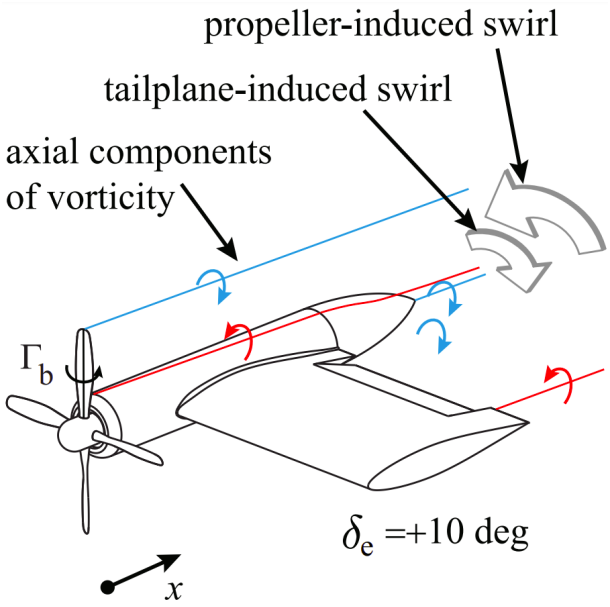

Figure 4.19: Schematic of axial vorticity of the wing and nacelle. [46]

Figure 4.20 displays the distribution of axial vorticity ω_x within the slipstream, in which contours of axial vorticity are shown to depict the flowfield. The inner region of the slipstream contains both positive and negative ω_x . The positive ω_x is produced by the nacelle tip and the outboard edge of the elevator, while the negative ω_x is formed by the propeller nacelle vortices.

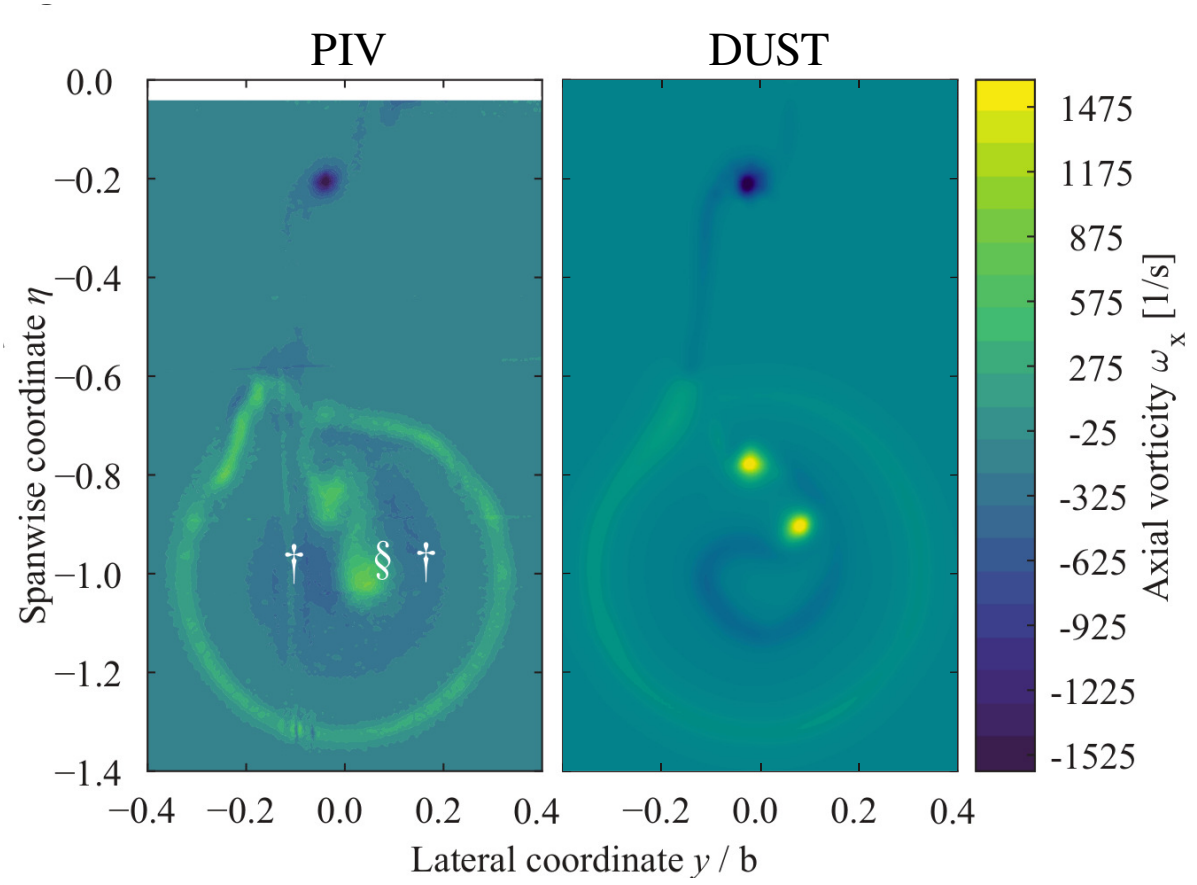

Figure 4.20: Time-averaged axial component of vorticity ω_x obtained in DUST,the slice is at 1.5c downstream the model, the results are compared with those coming from the experimental PIV plane. [45]

The contours reveal an increase in ω_x due to the propeller tip vortices that intersect with the wing. Notably, the location between the two counter-rotating vortices generated by the elevator tip-vortex and the propeller hub-vortices experiences a particularly high swirl velocity. [5]

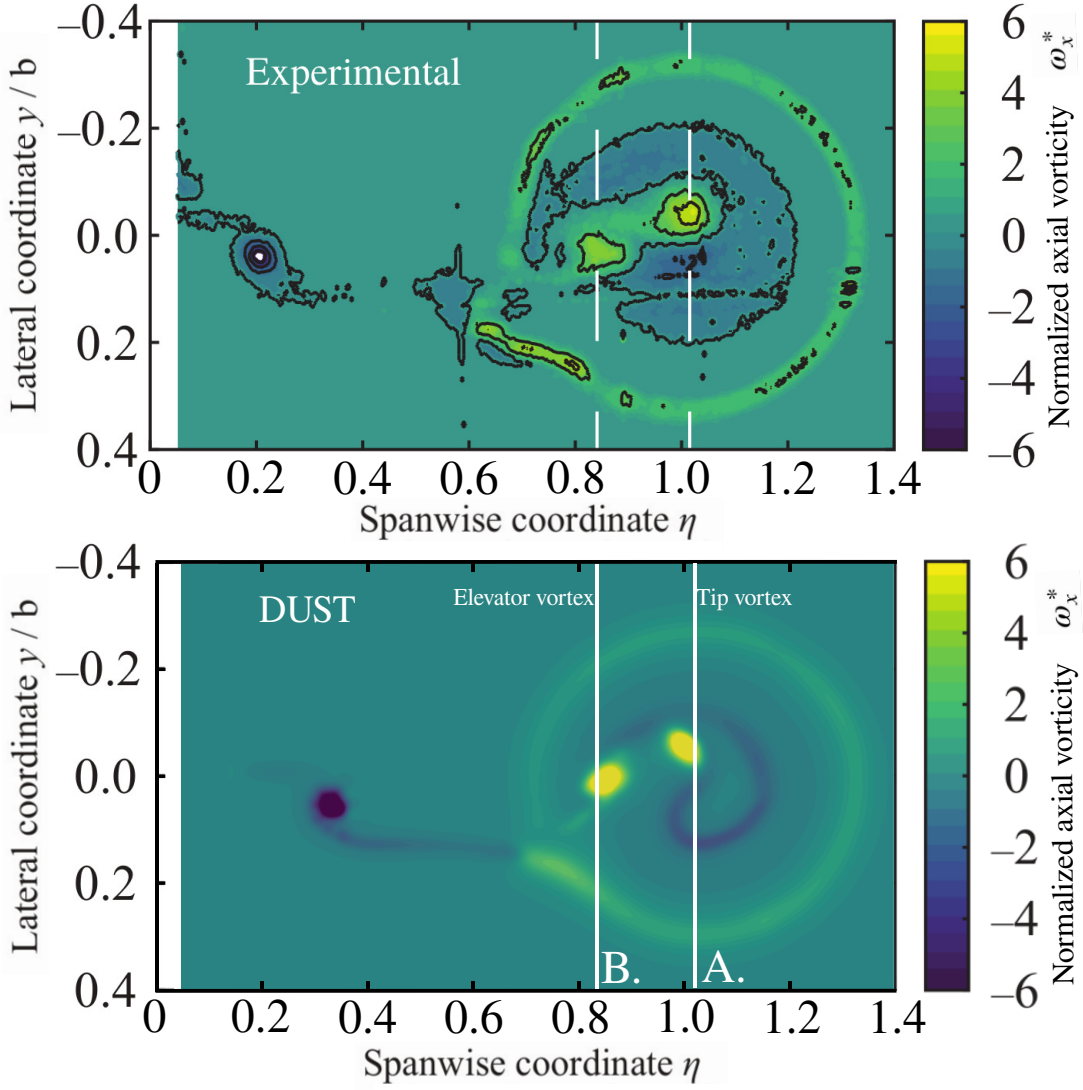

Figure 4.21: Time-averaged axial component of normalized axial vorticity ω_x^* obtained in DUST, the slice is at 1.5c downstream the model, the results are compared with those coming from the experimental PIV plane. [45]

The results presented in Figure 4.21 depict the distribution of normalized vorticity in the wake of the wing, and are compared to experimental measurements obtained using Particle Image Velocimetry (PIV) and reported by van Arnhem et al. [43]. The inboard and outboard elevator edges are observed to shed vortices at $y/b \approx 0.2$ and $y/b \approx 0.8$, respectively, and a tip vortex is observed at $y/b \approx 1$. The rotor slipstream is shown to envelop the tip vortex and undergo distortion by the wing surface, qualitatively agreeing with the experimental observations. Further evidence of quantitative agreement between the simulation and experiment is provided by slices of the vorticity across the elevator

vortex and tip vortex encompassed by the slipstream, as shown in Figures 4.22 and 4.23. This significant similarity between the flow field predicted by the DUST model and the experimental measurements indicates that the interactions between the rotor wake and the wing surface captured by the simulation, which are responsible for lift augmentation, are physically accurate.

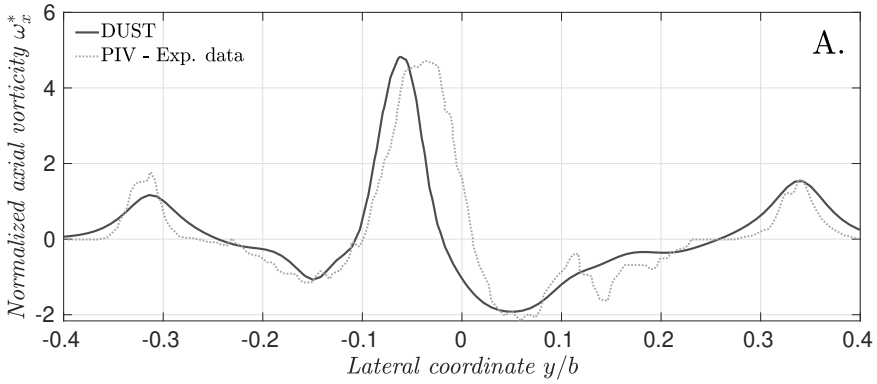

Figure 4.22: Time-averaged axial component of normalized axial vorticity ω_x^* across the Tip vortex plane shown in Fig. 4.21, DUST results are compared with the experimental PIV data. [45]

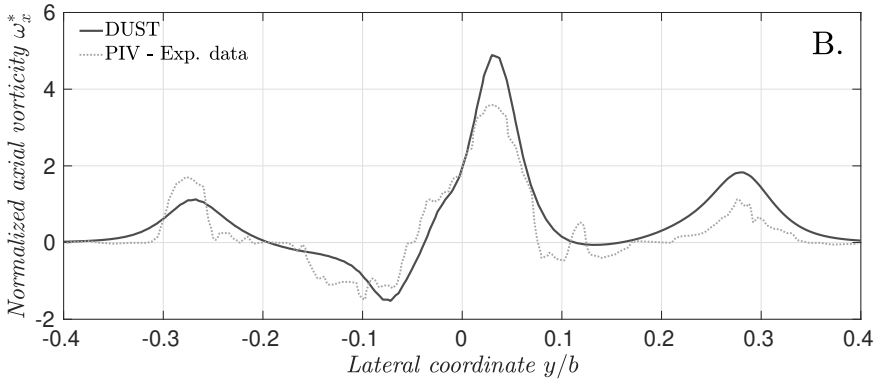

Figure 4.23: Time-averaged axial component of normalized axial vorticity ω_x^* across the elevator vortex plane shown in Fig. 4.21, DUST results are compared with the experimental PIV data.

Fig. 4.24 presents a visualization of the downwash field behind the propeller, which reveals both the load distribution and the swirl recovery by the wing. The DUST simulations show a slightly larger downwash along the wing due to the larger lift force, as compared to the experimental results.

The downwash near the propeller disk (Fig. 4.25b) clearly indicates that the swirl recovery is accurately captured by the DUST simulations.

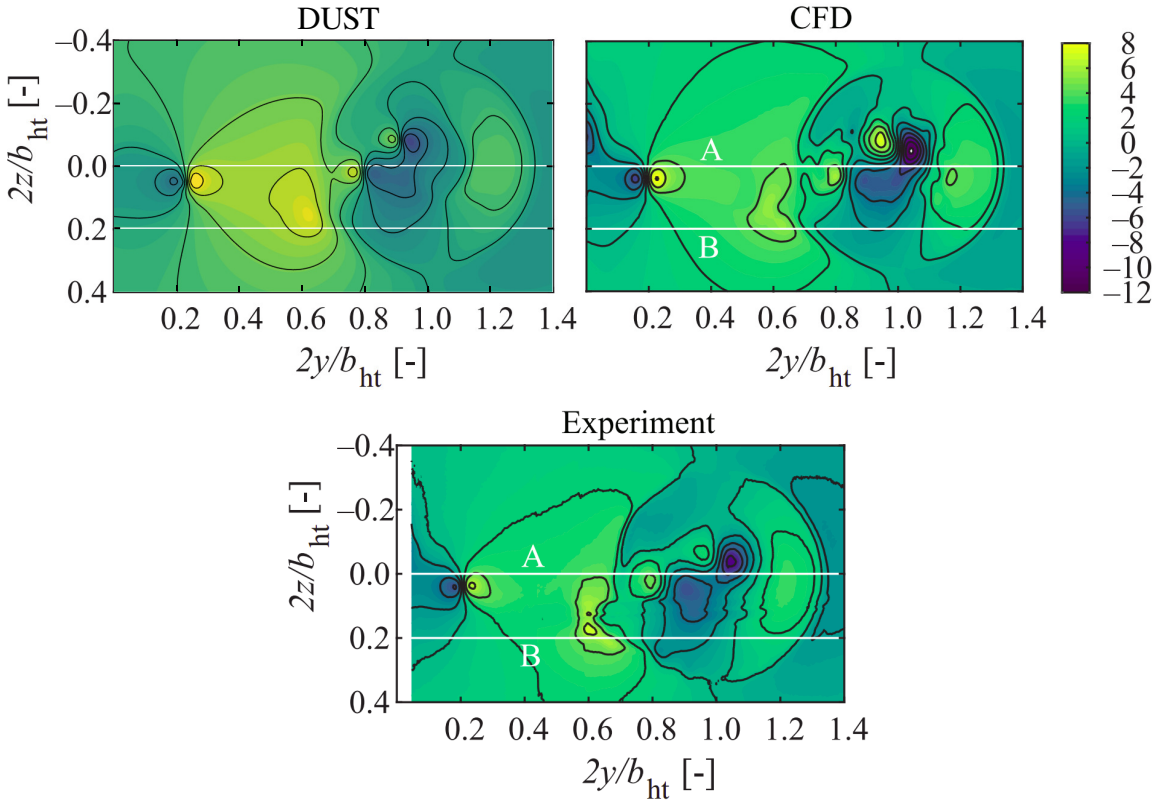

Figure 4.24: Downwash ε vertical slice behind at 1.5c behind the trailing edge of the propeller–horizontal wing model. The flowfield of the full-blade simulations are averaged over one rotation.

Additionally, we observe stronger upwash and downwash near $2y/b_{ht} \approx 1.0$, where the DUST simulations suggest the presence of a stronger vortex originating from the propeller nacelle. This is supported by the load distribution along the blade, which shows a more rapid reduction in thrust in this region, leading to the shedding of a stronger hub vortex. It's worth noting that the sign of this vortex is opposite to that of the tip vortex of the wing, which causes a local over prediction of the down and upwash in this region.

These figures also reveal that the gradients in the flowfield are diffused in the DUST simulation, as seen in Fig. 4.25a. However, the resemblance of the resulting flowfield to most of the details on average, and the adequate capture of the deformation of the slipstream, suggest that the diffusion of the vorticity does not significantly impact the flowfield.

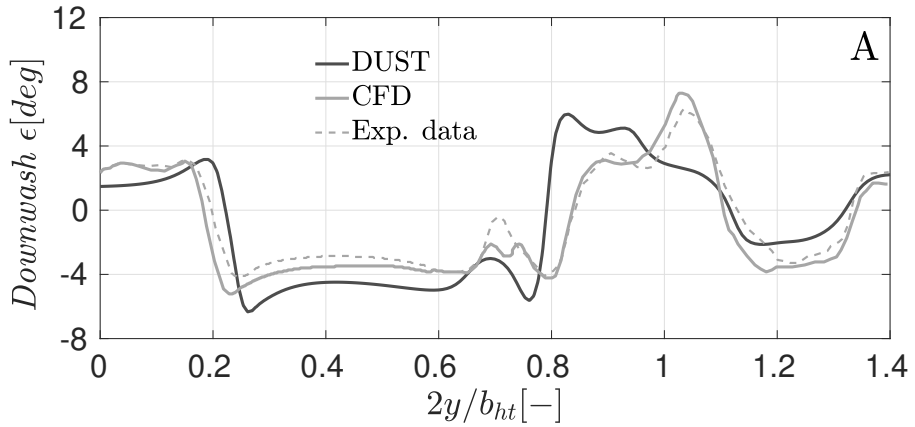

(a) Downwash ε in the A-plane

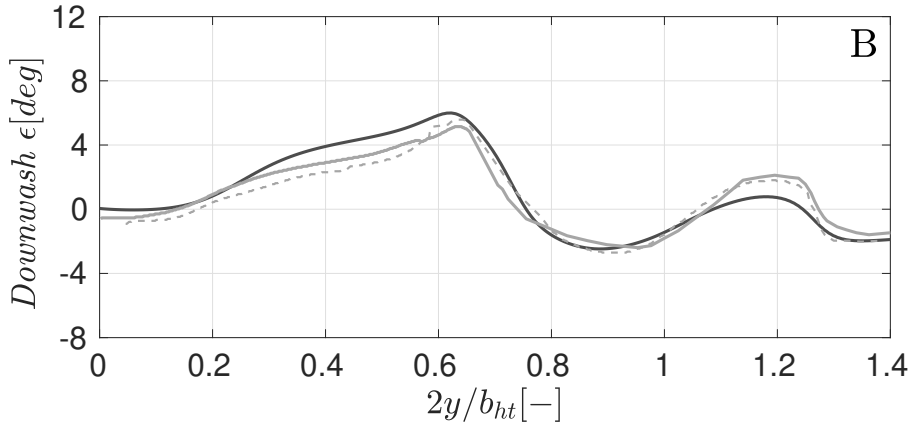

(b) Downwash ε in the B-plane

Figure 4.25: Slices of downwash angle on the two different planes.

The effect of the propeller on the distribution of wing loads is relatively small, as revealed by an analysis of the total-pressure distribution in a plane downstream of the model, as shown in Fig. 4.26 While the contour plot indicates a slightly greater increase in C_{P_t} in the most highly loaded region of the blades in the experiment, this is also evident in the survey lines in Figures 4.27a and 4.27b. The DUST result shows a larger wake originating from the nacelle hub region, resulting in a lower dynamic pressure in the slipstream on average. However, it should be noted that the contour plot is based on only one propeller rotation, and a more accurate depiction would require a much larger number of rotations. The regions of periodic flow show good agreement with the experiment, with the deformation of the slipstream indicative of the interaction between the propeller and wing captured well, and the magnitude and shape of the slipstream also in good agreement.

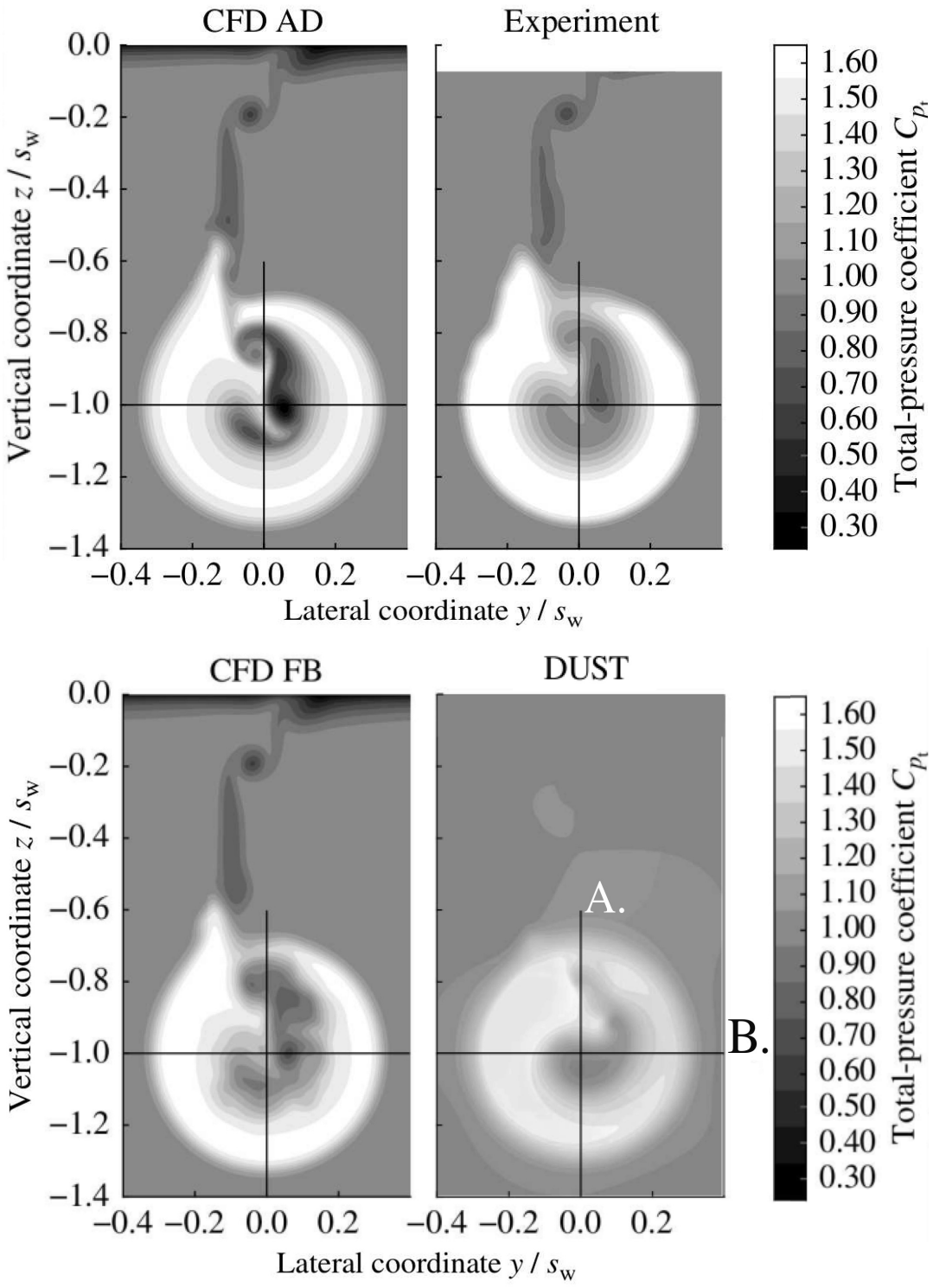

Figure 4.26: Total-pressure coefficient downstream the model

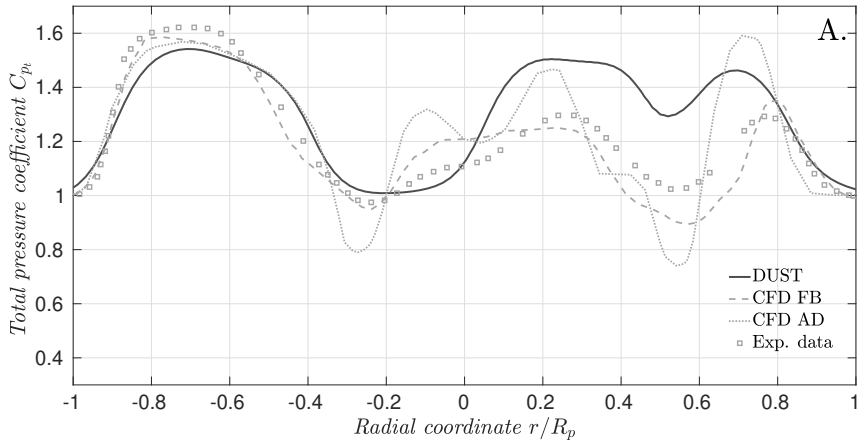

(a) C_{P_t} at $\theta = 0°$ profile

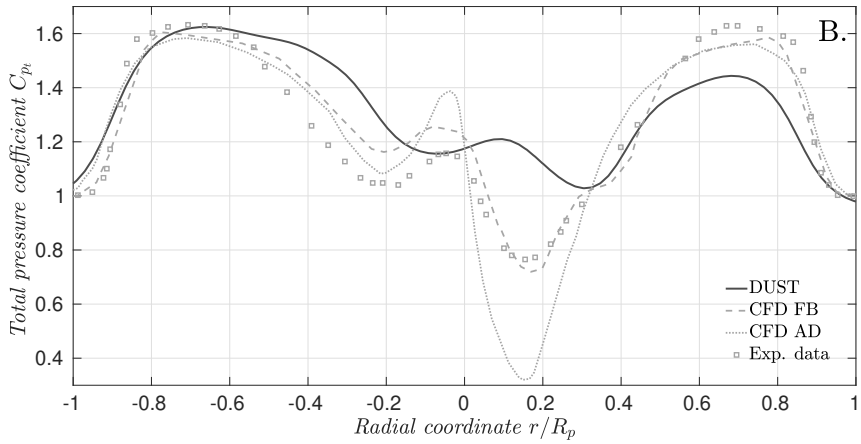

(b) C_{P_t} at $\theta = 90°$ profile

Figure 4.27: Total-pressure coefficient at 1.5c behind the trailing edge of the propeller–horizontal wing model. The flowfield of the full-blade simulations are the average over one rotation, while the experimental results are a time-averaged total-pressure profiles coefficients, $\delta_e = +10°, \alpha = 0°$ and $J = 0.8$.

4.6. Iso-surface flow visualizations

To aid in understanding the confirming the physics and provide a better visualization of the aerodynamic interaction, iso-surfaces of the Q-criterion are presented. Figure 4.28 clearly displays the location where the vortex impinges on the wing. This explains the wave-like pattern of increased negative pressure on the suction side of the chord pressure distribution at $\eta = 0.666$ in the DUST simulations, indicating vortex impingements on the wing surface. As the vortex is convected downstream, vortices became less and less strong.

Figure 4.29 offers further insights into critical vorticity-related features, such as the breakup caused by the wing's wake encounter and the redistribution of vorticity on the wing. Additionally, axial vorticity is represented in Figs. 4.30 and 4.31. It is important to point out that the inboard and outboard flap deflections generate two counter-rotating vortices, confirming the accuracy of the model.

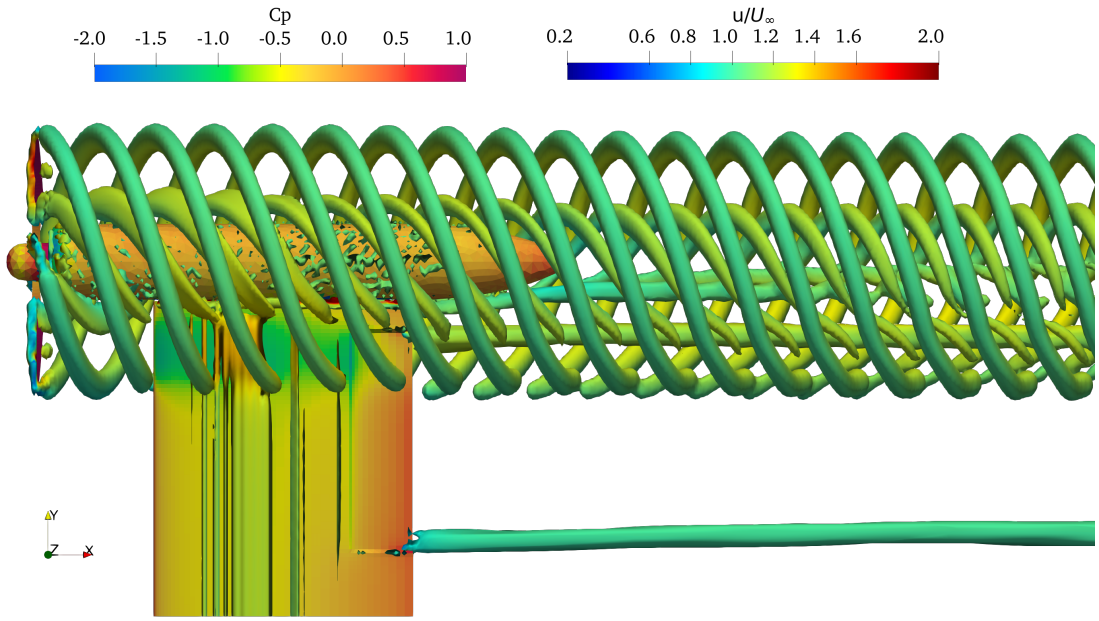

Figure 4.28: Top view - Q-criterion iso-surface of axial non-dimensional velocity u/U_∞ and contours of pressure coefficient on the model surface at $\delta_e = +10°, \alpha = 0°$ and $J = 0.8$ computed with DUST.

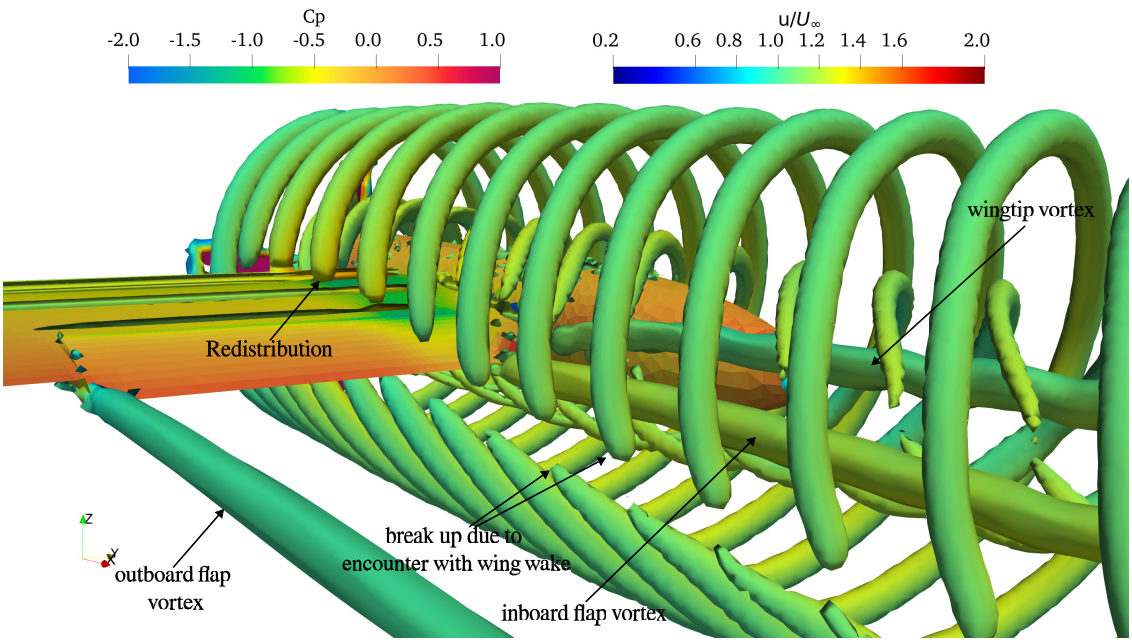

Figure 4.29: Zoom in the wake region, visualization through Q-criterion iso-surface of axial non-dimensional velocity u/U_∞ and contours of pressure coefficient on the model surface at $\delta_e = +10°, \alpha = 0°$ and $J = 0.8$ computed with DUST.

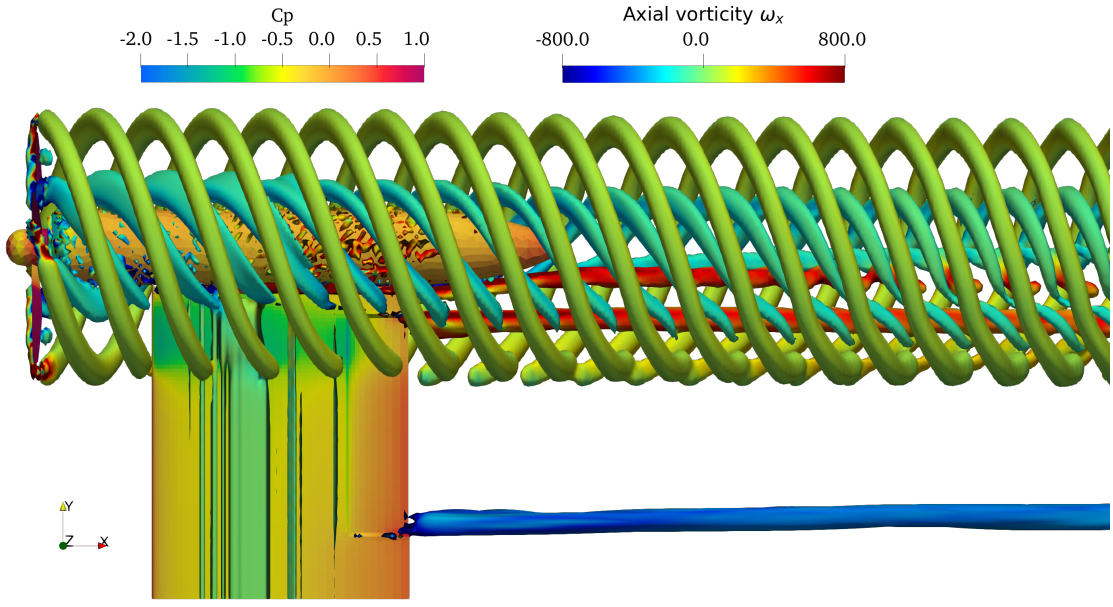

Figure 4.30: Top view - Q-criterion iso-surface of axial vorticity magnitude ω_x and contours of pressure coefficient on the model surface at $\delta_e = +10°, \alpha = 0°$ and $J = 0.8$ computed with DUST.

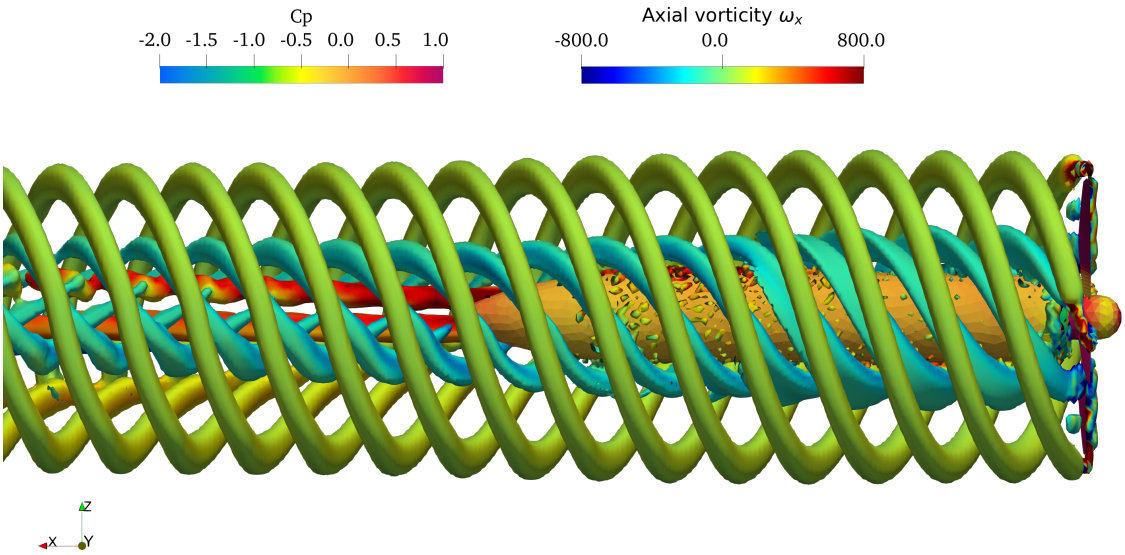

Figure 4.31: Side view - Q-criterion iso-surface of axial vorticity magnitude ω_x and contours of pressure coefficient on the model surface at $\delta_e = +10°, \alpha = 0°$ and $J = 0.8$ computed with DUST.

5 | Conclusions and future developments

This thesis has presented a numerical investigation of the capabilities of a vortex particle method-based aerodynamic solver, namely DUST, to analyze the complex aerodynamic interaction that occurs when a tractor tip-mounted propeller is installed on a wing with a deflected flap. The objective of this work was to establish a benchmark for further validation studies in this area and attempt to answer the still unanswered research questions stated at the beginning of this work.

The study began with an investigation of the isolated propeller to gain a comprehensive understanding of the propeller-induced flow field and propeller forces under various conditions. A grid sensitivity analysis was conducted to examine the effects of time-stepping and grid refinement. The results showed close agreement between the CFD case and the DUST model, with a 2.9% error on the C_T for the isolated configuration, and a good agreement between the performance curves.

A thorough study on the isolated wing was conducted to build a robust model, where a grid sensitivity analysis was done, knowing that no real grid convergence had to be expected due to the fact that a panel method does not solve the flow field in a physical domain, but instead on a mathematical surface. The study aimed to understand how varying the panelization would affect the integral and spanwise/chordwise loadings to gain a more accurate and realistic solution. The results for the isolated wing and nacelle showed a great resemblance to those of CFD and experimental results, with a difference in the total system C_L of about 1% with CFD and 4.7% with experimental results.

The level of integration was increased by mounting the propeller onto the airframe to study the interactional flow arising between the unsteady flow induced by the propeller and the presence of the wing and its wake. Several studies were conducted, and significant importance was placed on comprehensively understanding and explaining the physics of the interaction, allowing for identification of areas where the solver generated optimal and less accurate results. The modification on the propeller slipstream after installation

on the airframe was investigated, and the time-averaged results showed good agreement between the axial and tangential flow velocity fields and curves with CFD. However, the swirl velocity was not accurately captured near the nacelle region since no boundary layer is modeled in DUST, and the solver fails to provide accurate results due to high gradients that result in separation.

In addition, a study on the instantaneous axial velocity made possible a study on the tip-vortices arising from the tip blade passing. They appeared well captured, with a very good agreement in the mid-region, where DUST predictions closely matched the CFD results. However, in the tip regions where the highest gradients are, DUST fails to accurately resolve the tip vortices, resulting in a less sharp depiction of instantaneous quantities with large gradients, as observed from the velocity peaks near $r/R_P \approx 1$ due to the low numerical dissipation which is not capable of smearing down such large gradients. Moving downstream, the vortex impingement becomes less pronounced, and the DUST instantaneous axial velocity prediction improves.

A study was conducted to investigate the upstream effects on propeller performance and understand the differences that would arise after installation on propeller loadings. The radial non-dimensional thrust showed that installation increased propeller efficiency as the thrust curve shifted towards greater values in the r/R_P region where most thrust is produced. Integral values of C_T also confirmed this trend, showing a $+9.4$ % gain compared to the isolated test case. A polar plot of azimuthal thrust distribution confirmed the thrust increment was directed in the region where the suction side of the wing is, in accordance with CFD.

The study also exploited the influence of the propeller over wing performance, conducting numerous test cases on integral quantities that confirmed the capability of DUST to handle complex flow interactions. The system C_L increased by $+23.2$ % , passing from $C_L = 0.198$ for the isolated wing to $C_L = 0.244$, but this value showed slight underestimation due to the incapability of DUST to accurately capture the nacelle contribution to the system lift coefficient. Discrepancies in the nacelle zone introduced inaccuracies in the predictions due to the presence of recirculation and turbulent flow not being correctly captured by DUST. Spanwise sectional lift and chordwise pressure distribution showed great agreement with CFD and experiments, correctly depicting the location of vortex impingements over the wing surface. However, slight differences were found in the trailing edge location, where the first-order unsteady Kutta condition applied in DUST was not sufficient to guarantee the TE pressure matching condition, resulting in a lower pressure recovery and a non-matching pressure curve. It was presented a possible way to solve this issue by implementing a first-order scheme into DUST, a brief digression has been reported in the

Appendix A where a first-order method to solve the Morino integral formulation showed great results solving the issue at the trailing edge.

A study on the interaction of the propeller and slipstream wing-tip vortices showed great agreement with CFD, as DUST accurately captured the axial vorticity distribution and interaction arising from these vortices. However, the main drawback was found in zones where large gradients exist (vortex cores), here the DUST prediction was slightly underestimated. Finally, studies on the downwash angle and total pressure coefficient were conducted to provide a more complete depiction of the slipstream with all interactions, with the results closely matching CFD and experimental data. Possible developments in this field could involve studying the complete airplane setup to verify how the airframe affects the performance and flowfield. A significant focus may also be placed on studying aeroacoustics, and DUST has recently implemented the possibility of addressing this issue. In fact, last year, Guardone A. and Morelli M. [27] published a work on aeroacoustics with a focus on this particular model, further emphasizing the academic interest in such setups.

Looking ahead, one potential future work could be implementing the first-order scheme discussed in Appendix A to address the issue of non-matching pressure at the trailing edge of the configuration, which arises from the highly unsteady inflow experienced by the wing due to the propeller's slipstream.

Overall, this test case offers numerous opportunities to deepen our understanding of it and presents many challenges for DUST to broaden its range of applications.

Bibliography

[1] DUST - an aerodynamics solution for complex configurations, 2021. URL https://www.dust-project.org/.

[2] M. Abou-Zeid, A. P. Akkinepally, and C. A. Haddad. Contributors. In C. Antoniou, D. Efthymiou, and E. Chaniotakis, editors, *Demand for Emerging Transportation Systems*, pages xiii–xiv. Elsevier, 2020. ISBN 978-0-12-815018-4. doi: https://doi.org/10.1016/B978-0-12-815018-4.01002-0. URL https://www.sciencedirect.com/science/article/pii/B9780128150184010020.

[3] A. Abà, G. Guglieri, P. Capone, and F. Barra. Implementation of a comprehensive real-time simulation model of a tilt-rotor aircraft. Master's thesis, Politecnico di Torino, 2020.

[4] Adam Jonas. Flying Cars: Investment Implications of Autonomous Urban Air Mobility. Tech. rep. Morgan Stanley research, 2018. URL https://www.morganstanley.com/ideas/autonomous-aircraft.

[5] E. J. Alvarez, J. Mehr, and A. Ning. *FLOWUnsteady: An Interactional Aerodynamics Solver for Multirotor Aircraft and Wind Energy*. 2022. doi: 10.2514/6.2022-3218. URL https://arc.aiaa.org/doi/abs/10.2514/6.2022-3218.

[6] J. Anderson. *Fundamentals of Aerodynamics*. McGraw Hill, 2011.

[7] A. Anon. Racer high-speed demonstrator passes preliminary design review milestone. *Journal of the American Helicopter Society*, 35(3):43–51, 2019. URL https://www.airbus.com/newsroom/press-releases/en/2018/10/racer-high-speed-demonstrator-passes-preliminary-design-review-m0.html.

[8] T. Berger. Handling qualities requirements and control design for high-speed rotorcraft fixed wing system identification, flight control design, and handling qualities analysis view project f-16 vista system identification-stitched model development view project. *Journal of the American Helicopter Society*, 2019. URL https://www.researchgate.net/publication/338411572.

[9] ELAN HEAD. Lilium eVTOL prototype damaged in ground fire. VerticalMag, 2020. URL https://verticalmag.com/news/lilium-evtol-catches-fire/.

[10] M. Foster. Evolution of tiltrotor aircraft. In *Evolution of Tiltrotor Aircraft*. American Institute of Aeronautics and Astronautics (AIAA), 7 2003. doi: 10.2514/6.2003-2652.

[11] M. Fu, R. Rothfeld, and C. Antoniou. Exploring preferences for transportation modes in an urban air mobility environment: Munich case study. *Transportation Research Record*, 2673(10):427–442, 2019. doi: 10.1177/0361198119843858. URL https://doi.org/10.1177/0361198119843858.

[12] S. Gallay and E. Laurendeau. Nonlinear generalized lifting-line coupling algorithms for pre/poststall flows. *AIAA Journal*, 53(7):1784–1792, 2015. doi: 10.2514/1.J053530. URL https://doi.org/10.2514/1.J05350.

[13] R. D. Hager and D. Vrabel. Advanced turboprop project. 1 1988. URL https://www.osti.gov/biblio/6450714.

[14] H. Hesse and R. Palacios. Reduced-order aeroelastic models for the dynamics of manoeuvring flexible aircraft. In *Reduced-Order Aeroelastic Models for the Dynamics of Manoeuvring Flexible Aircraft*, 06 2013.

[15] R. T. Johnston and J. P. Sullivan. Unsteady wing surface pressures in the wake of a propeller. *Journal of Aircraft*, 30(5):644–651, 1993. doi: 10.2514/3.46393. URL https://doi.org/10.2514/3.46393.

[16] R. T. Johnston and J. P. Sullivan. Unsteady wing surface pressures in the wake of a propeller. *Journal of Aircraft*, 30(5):644–651, 1993. doi: 10.2514/3.46393. URL https://doi.org/10.2514/3.46393.

[17] J. Kerwin, S. Kinnas, J.-T. Lee, and W. Shih. A surface panel method for the hydrodynamic analysis of ducted propellers. *Trans. SNAME*, 95:22, 01 1987.

[18] S. A. Kinnas and C.-Y. Hsin. Boundary element method for the analysis of the unsteady flow aroundextreme propeller geometries. *AIAA Journal*, 30(3):688–696, 1992. doi: 10.2514/3.10973. URL https://doi.org/10.2514/3.10973.

[19] L. Leone, P. Civiletti, P. Costa, and J. Feenstra. Tiltrotor aerodynamic and structural design of the leonardo 609 aircraft. *American Institute of Aeronautics and Astronautics*, 35(3):1–40, 2020.

[20] Loz Blain. Joby crashes one of its two eVTOL prototypes during high-speed testing. NewAtlas, 2020. URL https://newatlas.com/aircraft/joby-crash-evtol/.

[21] Y. Lu, T. Su, R. Chen, P. Li, and Y. Wang. A method for optimizing the aerodynamic layout of a helicopter that reduces the effects of aerodynamic interaction. *Aerospace Science and Technology*, 88:73–83, 2019. ISSN 1270-9638. doi: https://doi.org/10.1016/j.ast.2019.03.005. URL `https://www.sciencedirect.com/science/article/pii/S1270963818317760`.

[22] M. D. Maisel. *The history of the XV-15 tilt rotor research aircraft: from concept to flight*. National Aeronautics and Space Administration, Office of Policy and Plans, 2000.

[23] M. A. McVeigh, W. K. Grauer, and D. J. Paisley. Rotor/airframe interactions on tiltrotor aircraft. *Journal of the American Helicopter Society*, 35(3):43–51, 1990.

[24] G. MITCHELL and D. MIKKELSON. *Summary and recent results from the NASA advanced high-speed propeller research program*. 1984. doi: 10.2514/6.1982-1119. URL `https://arc.aiaa.org/doi/abs/10.2514/6.1982-1119`.

[25] D. Molini. Aerodynamic optimization of the wing extension of an advanced tiltrotor aircraft. Master's thesis, Politecnico di Milano, 2022.

[26] D. Montagnani, M. Tugnoli, A. Zanotti, M. Syal, G. Droandi, et al. Analysis of the interactional aerodynamics of the vahana evtol using a medium fidelity open source tool. In *VFS Aeromechanics for Advanced Vertical Flight Technical Meeting*, pages 436–451. Vertical Flight Society, 2020.

[27] M. Morelli, A. Guardone, and B. Y. Zhou. *Computational Aeroacoustic Analysis of a Wing-Tip Mounted Propeller and High-Lift Device*, chapter 1-5, pages 1–18. doi: 10.2514/6.2022-2939. URL `https://arc.aiaa.org/doi/abs/10.2514/6.2022-2939`.

[28] L. Morino. Helmholtz decomposition revisited: vorticity generation and trailing edge condition. *Computational Mechanics*, 1(1):65–90, 1986.

[29] L. Morino and C.-C. Kuot. Subsonic potential aerodynamics for complex configurations: a general theory. *AIAA Journal*, 12(2):191–197, 1974. doi: doi.org/10.2514/3.49191.

[30] R. Piccinini. Rotor-rotor aerodynamic interactions for evtol aircraft configurations. Master's thesis, Politecnico di Milano, 202o.

[31] S. T. Piszkin and E. Levinsky. Nonlinear lifting line theory for predicting stalling instabilities on wings of moderate aspect ratio. Technical report, GENERAL DYNAMICS SAN DIEGO CA CONVAIR DIV, 1976.

[32] M. A. Potsdam and R. C. Strawn. Cfd simulations of tiltrotor configurations in hover. *Journal of the American Helicopter Society*, 50(1):82–94, 2005.

[33] H. Rosenstein and R. Clark. Aerodynamic development of the v-22 tilt rotor. In *Aircraft Systems, Design and Technology Meeting*, page 2678, 1986.

[34] S. Roy, A. Maheshwari, W. A. Crossley, and D. A. DeLaurentis. Future regional air mobility analysis using conventional, electric, and autonomous vehicles. *Journal of Air Transportation*, 29(3):113–126, 2021. doi: 10.2514/1.D0235. URL `https://doi.org/10.2514/1.D0235`.

[35] A. Savino, A. Cocco, A. Zanotti, M. Tugnoli, P. Masarati, and V. Muscarello. Coupling mid-fidelity aerodynamics and multibody dynamics for the aeroelastic analysis of rotary-wing vehicles. *Energies*, 14, 11 2021. ISSN 19961073. doi: 10.3390/en14216979.

[36] A. Savino, A. Cocco, A. Zanotti, and V. Muscarello. Numerical investigation of wing-propeller aerodynamic interaction through a vortex particle-based aerodynamic solver. *American Institute of Aeronautics and Astronautics*, February 2022. Paper no. HT-FED2004-56887.

[37] N. Singh, G. Bandyopadhyay, and B. Basu. Calculation of potential flow about arbitrary three dimensional wings using internal singularity distributions. *Aeronautical Quarterly*, 34(3):197–211, 1983. doi: 10.1017/S0001925900009707.

[38] T. Sinnige, R. de Vries, B. D. Corte, F. Avallone, D. Ragni, G. Eitelberg, and L. L. M. Veldhuis. Unsteady pylon loading caused by propeller-slipstream impingement for tip-mounted propellers. *Journal of Aircraft*, 55(4):1605–1618, 2018. doi: 10.2514/1.C034696. URL `https://doi.org/10.2514/1.C034696`.

[39] T. Sinnige, T. Stokkermans, N. van Arnhem, and L. Veldhuis. Aerodynamic performance of a wingtip-mounted tractor propeller configuration in windmilling and energy-harvesting conditions. In *2*, 06 2019. doi: 10.2514/6.2019-3033.

[40] T. Sinnige, N. van Arnhem, T. C. A. Stokkermans, G. Eitelberg, and L. L. M. Veldhuis. Wingtip-mounted propellers: Aerodynamic analysis of interaction effects and comparison with conventional layout. *Journal of Aircraft*, 56(1):295–312, 2019. doi: 10.2514/1.C034978. URL `https://doi.org/10.2514/1.C034978`.

[41] T. Sinnige, N. van Arnhem, T. C. A. Stokkermans, G. Eitelberg, and L. L. M. Veldhuis. Wingtip-mounted propellers: Aerodynamic analysis of interaction effects

and comparison with conventional layout. *Journal of Aircraft*, 56(1):295–312, 2019. doi: 10.2514/1.C034978. URL https://doi.org/10.2514/1.C034978.

[42] M. H. SNYDER and G. W. ZUMWALT. Effects of wingtip-mounted propellers on wing lift and induced drag. *Journal of Aircraft*, 6(5):392–397, 1969. doi: 10.2514/3.44076. URL https://doi.org/10.2514/3.44076.

[43] T. C. A. Stokkermans, N. van Arnhem, T. Sinnige, and L. L. M. Veldhuis. Validation and comparison of rans propeller modeling methods for tip-mounted applications. *AIAA Journal*, 57(2):566–580, 2019. doi: 10.2514/1.J057398. URL https://doi.org/10.2514/1.J057398.

[44] M. Tugnoli, D. Montagnani, M. Syal, G. Droandi, and A. Zanotti. Mid-fidelity approach to aerodynamic simulations of unconventional vtol aircraft configurations. *Aerospace Science and Technology*, 115:106804, 2021.

[45] N. Van Arnhem. *Unconventional Propeller-Airframe integration for transport aircraft configurations*. PhD thesis, Delft University of Technology, 2022.

[46] N. van Arnhem, T. Sinnige, T. Stokkermans, G. Eitelberg, and L. Veldhuis. Aerodynamic interaction effects of tip-mounted propellers installed on the horizontal tailplane. In *2*, 01 2018. doi: 10.2514/6.2018-2052.

[47] N. van Arnhem, R. de Vries, R. Vos, and L. L. Veldhuis. *Aerodynamic Performance of an Aircraft Equipped with Horizontal Tail Mounted Propellers*, chapter 1, page 1. 2019. doi: 10.2514/6.2019-3036. URL https://arc.aiaa.org/doi/abs/10.2514/6.2019-3036.

[48] L. Veldhuis. *Propeller Wing Aerodynamic Interference*. MDPI, 2005. ISBN 9789090195377. URL https://books.google.it/books?id=Cr9CmwEACAAJ.

[49] L. Viterna and R. Corrigan. Fixed pitch rotor performance of large horizontal axis wind turbines. *Large Horizontal-Axis Wind Turbines*, -1:69–85, 01 1982.

[50] M. Wentrup, J. Yin, P. Kunze, T. Streit, J.-H. Wendisch, T. Schwarz, J.-P. Pinacho, K. Kicker, and R. Fukari. An overview of dlr compound rotorcraft aerodynamics and aeroacoustics activities within the cleansky2 nacor project. 05 2018.

[51] G. S. Winckelmans. *opics in Vortex Methods for the Computation of Three- and Two-Dimensional Incompressible Unsteady Flows*. PhD thesis, California Institute of Technology, 1. URL https://resolver.caltech.edu/CaltechETD:etd-11032003-112216.

[52] T. Wood and M. Peryea. Reduction of tiltrotor download. *Journal of the American Helicopter Society*, 40(3):42–51, 1995.

[53] J. Yin and S. Ahmed. Helicopter main-rotor/tail-rotor interaction. *Journal of the American Helicopter Society*, Vol. 45:293–302, 10 2000. doi: 10.4050/JAHS.45.293.

[54] A. Zanotti, A. Savino, M. Palazzi, M. Tugnoli, and V. Muscarello. Assessment of a mid-fidelity numerical approach for the investigation of tiltrotor aerodynamics. *American Institute of Aeronautics and Astronautics*, April 2021. Paper no. HT-FED2004-56887.

A | Appendix A

In this section, the issue of the non-matching pressure at the trailing edge encountered in the development of this work is addressed. A feasible solution is proposed to be implemented in DUST to suppress this inaccuracy and enlarge the situations in which the mid-fidelity method is capable of giving strong physical results.

The riformulated numerical scheme exploted in this section was first proposed by Kinnas et al in [18]. The high aspect ratio TUD-PROWIM propeller produces a highly unsteady slipstream that interacts with the wing profile located downstream. This causes the wing to experience an unsteady inflow velocity that is composed of both the asymptotic velocity V_∞ and the periodic slipstream of the propeller. As a result, the Kutta condition needs to be reformulated, and an explicit Kutta condition is necessary to accurately model the system.

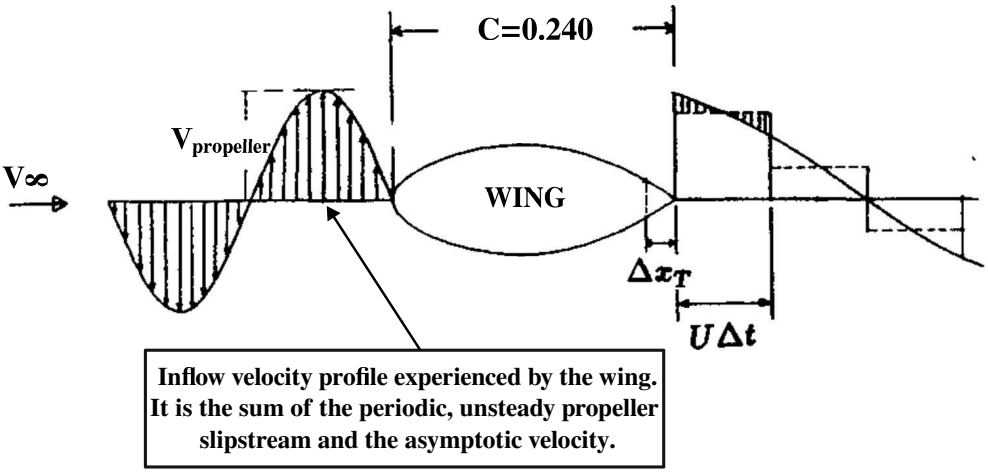

Figure A.1: Schematic representation of the inflow flow experienced by the wing.

In addition to the challenges mentioned earlier, another complication arises due to the high rotational speed of the propeller. The propeller and the wing have different timescales, with the former experiencing a much higher rotational speed, up to V_{tip} of around 158 m/s, while the latter experiences speeds around 40 $\pm$ 15 m/s. As a result, the first wake panel of the wing has a high aspect ratio, which is crucial for accurate representation and

evolution of the wake in panel methods. However, the solution is shifted in time, resulting in a purely mathematical representation of the wake in a few adjacent wake panels near the trailing edge. These suboptimal conditions render the numerical formulation for the Kutta condition implemented in DUST insufficient to achieve accurate results in the TE region, where a non-matching pressure between the suction and pressure side is present.

In DUST the pressure p at every point x on the wing and for each time step n is computed from the potentials on the wing by applying the unsteady-flow Bernoulli's equation with respect to the propeller system:

$$\frac{p}{\rho} + \frac{q^2}{2} + \frac{\partial \phi}{\partial t} = \frac{p_\infty}{\rho} + \frac{q_\infty^2}{2} \tag{A.1}$$

In addition, the high rotational speed of the propeller posed another complication. The propeller and the wing have different time scales, with the propeller experiencing extremely high rotational speeds reaching up to V_{tip} of about 158 m/s, while the wing experiences speeds in the order of 40 $\pm$ 15 m/s. This difference results in a high aspect-ratio for the first wake panel of the wing, which is vital in the correct representation and evolution of the wake in panel methods. However, this leads to suboptimal conditions for a numerical scheme, as the solution is computed in just a few adjacent wake panels to the trailing edge and then shifted in time, creating the wake in a purely mathematical way. [37]

Due to these suboptimal conditions, the numerical formulation for the Kutta condition implemented in DUST was found to be insufficient to achieve accurate results in the trailing edge region of the wing subjected to such an high unsteady inflow. here a non-matching pressure between suction and pressure side was present.

In order to ensure pressure equality at the wing trailing edge at each time step, Kinnas et al. in 1992 proposed an alternative approach to deal with this kind of highly unsteady inflow in [18]. In his work an iterative Newton-Raphson scheme was implemented to adjust the circulation around each strip of the lifting surface. An explicit pressure Kutta condition was also found to be required, as the numerical Kutta condition was found to be inadequate in the steady-flow BEM for propellers.

Moreover, the method was discovered to be highly sensitive to the size of the time step, Δt, when a constant-strength dipole distribution was utilized in the first wake panel. [17] The results were observed to be very dependent on the ratio of the length of the first wake panel $U\Delta t$ to the length of the trailing-edge panel Δx_t. This dependency on the time step is an undesirable characteristic for any unsteady-flow BEM. However, replacing the

constant-strength panels in the wake with a linear distribution resolved the issue, as the results became independent of the time step. The poor performance of the constant-wake dipole panel is attributed to the fact that the potentials induced on the trailing-edge panels by the saw-tooth dipole distribution on the first wake panel become larger with larger time steps and slope of the dipole distribution at the trailing edge (i.e., frequency). [18]

Standard numerical implementation

To solve the Morino [29] integral formulation (reported in Eq. 2.16 in Chapter 2) numerically, DUST discretizes the propeller and wake surface into quadrilateral panels and approximates the doublet or source distributions on each panel using constant strength distributions. This discretized version of the integral formulation is then applied at the center of each propeller panel and at each time step, which is determined by dividing the time interval t into increments of size Δt, resulting in $n = \frac{t}{\Delta t}$ time steps. The resulting equation is a Fredholm integral equation of the second kind with respect to ϕ. [18]

$$\sum_{j=1}^{N_P} a_{i,j}\phi_j^k(n) + \sum_{m=1}^{N_{spanwise}} \sum_{l=1}^{N_W} W_{i,m,l}\Delta\phi_{m,l}(n) = \sum_{j=1}^{N_P} b_{i,j}\sigma_j(n); \qquad i = 1, N_P \tag{A.2}$$

Where N_P is the number of panel, N_W is the number of wake panels and $N_{spanwise}$ is the number of panels in the spanwise direction. $a_{i,j}$ and $b_{i,j}$ are the influence coefficients and are defined as the potentials induced at panel i by a unit strength dipolo/cource distribution located at panel j. The wake influence coefficient $W_{i,m,l}$ is defined similarly. σ_j is the source strength that can be retrieved directly from the boundary condition as following, hence it does not represent a further unknown.

$$\sigma_j(n) = -\vec{U}_{i,n}(x_j, y_j, z_j, n\Delta t) \cdot \vec{n_j} \tag{A.3}$$

The wake contribution is modeled by imposing the condition that the material derivative with respect to the fluid velocity of the potential jump must be equal to zero. This condition is used to generate a new solution each time starting from the solution computed at the trailing edge. Applying the Kutta condition ensures that the pressure jump in the wake is equal to zero. This is achieved by imposing that the potential jump across the wake after a certain time t is the same as the one obtained at the trailing edge with a suitable shift in time. The value of the potential jump at the trailing edge is obtained

using the following relation:

$$\Delta\phi_{TE}(r,t) = \phi^{+}_{TE}(r,t) - \phi^{-}_{TE}(r,t) \tag{A.4}$$

Where $\phi^{+}_{TE}(r,t)$ and $\phi^{-}_{TE}(r,t)$ are the values of the potential at the upper and lower side of the trailing edge. A more coincise formulation for Eq. A.2 is here reported, here the explicit dependence of the wake from the trailing edge value of $\Delta\phi$ is reported:

$$\sum_{j=1}^{N_P} a_{i,j}\phi_j(n) + \sum_{m=1}^{N_{spanwise}} W_{i,m,1}\Delta\phi_{m,1}(n) = RHS_i(n) \qquad i = 1, N_P \tag{A.5}$$

In the linear system description, all known quantities computed in the prior time-step are moved to the right-hand side (RHS(n)) to form a system of n equations that require the potential to be computed at each iteration. This scheme is currently implemented in DUST and uses an iterative method to solve the system of equations A.2. The value of the potential $\Delta\phi_{m,1}$ at the first wake panel can be obtained by using Eq. A.6.

$$\begin{aligned} &\Delta\phi_{m,1} = \frac{\Gamma_m(n) + \Gamma_m(n-1)}{2} \\ &with: \qquad \Gamma_m(n) = \phi^{+}_{m}(n) - \phi^{-}_{m}(n) \end{aligned} \tag{A.6}$$

With $\Gamma_m(n)$ denoting the circulation around the wing strip m at the time step n and $\phi^{+}_{m}(n)$ and $\phi^{-}_{m}(n)$ the potentials at the upper and lower trailing-edge panel, respectively, at the wing strip m. What has been exploited up till now is how the actual formulation implemented in DUST solve the morino integral formulation for a lifting body. As anticipated this is not enough in the previously digressed cases hence a reformulated version is here eploited:

Reformulated numerical scheme

The reformulated version proposed by Kinnas et al. [18] is presented below as a possible solution to the non-matching pressure issue encountered in DUST when dealing with highly unsteady inflows at the trailing edge. This numerical scheme is designed to address the problems encountered at the trailing edge by approximating the dipole sheet on the first wake panel with a linear distribution, rather than a constant one. This modification is necessary to make the results of the unsteady DUST formulation less dependent on the size of the time step. In this case, the system of equations in Eq. A.2 will be modified as

follows:

$$\sum_{j=1}^{N_P} a_{i,j}\phi_j(n) + \sum_{m=1}^{N_{spanwise}} T^L_{i,m}\Gamma_m(n) = \overline{RHS}_i(n) \qquad i = 1, N_P$$

$$with:$$
$$\overline{RHS}_i(n) = RHS_i(n) - T^R_{i,m}\Gamma_m(n-1) \qquad i = 1, N_P \tag{A.7}$$

When examining a single wing strip and its wake, one may assume the presence of a dipole distribution on the first wake panel that is linear along the chordwise direction. [18] The dipole strength, denoted by μ at time step n, can be expressed as follows:

$$\mu(s) = \Gamma(n) + \frac{\Gamma(n-1) - \Gamma(n)}{\Delta x_w} s \tag{A.8}$$

where Δx_w is the chordwise length of the first wake panel, and s is the chordwise distance from the wing trailing edge. $\Gamma(n)$ and $\Gamma(n-1)$ are the circulations at time steps (n) and (n-1). The influence, I_P , of the first wake panel at any point P in the flowfield can be expressed in the following integral form:

$$I_P = \int_A w(s,r)\mu(s)dsdr \tag{A.9}$$

The expression for I_P involves the surface area A of the panel described by the coordinates r and s, and the influence w of a unit strength dipole normal to the surface of the panel at location (r, s). Utilizing equation A.8, I_P can be represented as:

$$I_P = T^L\Gamma(n) + T^R\Gamma(n-1) \tag{A.10}$$

where:

$$T^L = \int_A w(s,r)[1-\bar{s}]dsdr$$
$$T^R = \int_A w(s,r)\bar{s}dsdr \tag{A.11}$$

Where $\bar{s} = s/\Delta x_w$

Solving the riformulated Eq. A.7 at each time step, a system of N_P linear equations with respect to the N_P unknown potentials on the panels of the wing is obtained. Equation A.7 can also be written in the following matrix form:

$$[A][\phi^*] + [T][\Gamma^*] = [RHS] \tag{A.12}$$

To obtain the values of Γ^*, the non-linear system of equations A.14 must be solved, which involves computing the relative pressure jump $[\Delta p^*]^{(k)}$ corresponding to the values of $[\phi^*]^{(k)}$ obtained from solving the linear system. Since this is a non-linear system, it requires an iterative approach, and in this work, the Newton-Raphson scheme is employed for obtaining the values of Γ^*.

$$[A][\phi^*]^{(k)} = [RHS]^{(k)} - [T][\Gamma^*]^{(k)} \tag{A.13}$$

$$\begin{cases} [\Gamma^*]^{(k+1)} = [\Gamma^*]^{(k)} - [J^{(k)}]^{-1}[\Delta p^*]^{(k)} \\ \\ [\phi^*]^{(1)} = [\phi] \\ [\Gamma^*]^{(1)} = [\Gamma] \end{cases} \tag{A.14}$$

$$where: \qquad J_{i,j}^{(k)} = \frac{\partial \Delta p_i^{*(k)}}{\partial \Gamma_j^{*(k)}} \tag{A.15}$$

Additionally, it is worth noting that a more efficient modified Newton-Raphson method can be applied as the values of the Jacobian do not change significantly after each iteration. [18] This enables the linear system to be solved in a more efficient manner, as the Newton-Raphson method can be utilized without the need for computing and inverting the Jacobian at each time-step, which is the most computationally costly part of the entire process.

List of Figures

List of Tables

List of Symbols

Variable	Description
a	speed of sound $[ms^{-1}]$
b	wing span [m]
c	local blade chord [m]
C	mean wing chord [m]
c_d	sectional drag coefficient $= \frac{d}{\frac{1}{2}\rho_\infty V_\infty^2}$ [-]
c_l	sectional lift coefficient $= \frac{l}{\frac{1}{2}\rho_\infty V_\infty^2}$ [-]
c_m	sectional pitch coefficient $= \frac{m}{\frac{1}{2}\rho_\infty V_\infty^2 c}$ [-]
C_D	drag coefficient $= \frac{D}{\frac{1}{2}\rho_\infty V_\infty^2}$ [-]
C_L	lift coefficient $= \frac{L}{\frac{1}{2}\rho_\infty V_\infty^2}$ [-]
C_M	pitch coefficient $= \frac{M}{\frac{1}{2}\rho_\infty V_\infty^2 c}$ [-]
C_P	pressure coefficient $= \frac{P-P_\infty}{\frac{1}{2}\rho_\infty V_\infty^2 c}$ [-]
$C_{P,t}$	total pressure coefficient $= \frac{P_t-P_\infty}{\frac{1}{2}\rho_\infty V_\infty^2 c}$ [-]
$C_{P,stag}$	pressure coefficient at stagnation point$= \frac{P_{stag}-P_\infty}{\frac{1}{2}\rho_\infty V_\infty^2 c}$ [-]
C_q	torque coefficient $= \frac{Q}{\rho_\infty n^2 D_p^5}$ [-]
C_t	thrust coefficient $= \frac{T}{\rho_\infty n^2 D_p^4}$ [-]
D	wing drag force [N]
D_p	propeller diameter [m]
J	advance ratio $= \frac{v_\infty}{nD_p}$ [-]
L	wing lift force [N]
M	wing pitching moment [Nm]
M_∞	freestream Mach number [-]
n	propeller rotational speed [rps]
N	blade normal force [N]
N_{STEP}	propeller time discetiziation [-]
p	pressure [Pa]

Q	propeller torque [Nm]
r	radial coordinate along the blade [m]
R_p	propeller radius [m]
Re	Reynolds number [-]
S	span coordinate [m]
T	propeller thrust [N]
u, v, w	velocity in Cartesian system $[ms^{-1}]$
V_a	axial flow velocity $[ms^{-1}]$
V_t	tangential flow velocity $[ms^{-1}]$
V_{tip}	rotor tip velocity $[ms^{-1}]$
V_∞	freestream velocity $[ms^{-1}]$
X, Y, Z	freestream coordinate system [m]

GREEK LETTERS

α	angle of attack [deg]
Γ	circulation $[m^2s^{-1}]$
δ_e	elevator deflection angle [deg]
ε_{C_T}	$error_{\%}$ of the thrust coefficient [-]
ε_{C_L}	$error_{\%}$ of the lift coefficient [-]
ε_{C_l}	$error_{\%}$ of the sectional lift coefficient [-]
ε	downwash angle [deg]
η	normalized spanwise choordinate = $\frac{S}{0.326}$ [-]
η_p	propeller efficiency = $\frac{V_\infty}{nD_p}$ [-]
ρ_∞	freestream air density [kg/m^3]
ψ	blade azimuthal angle [deg]
ϕ	swirl angle [deg], velocity potential [-]
ω	vorticity $[s^{-1}]$
ω^*	Normalized vorticity = $\frac{\omega D_p}{V_\infty}$ [-]

ABBREVIATIONS

CFD	computational fluid dynamics
$URANS$	Unsteady Reynolds Averaged Navier–Stokes
AD	actuator disk

Acknowledgements

I would like to express my sincere gratitude to Professor Alex Zanotti whose guidance, support, and expertise have been invaluable throughout this project, I am truly grateful for your mentorship. I would also like to acknowledge and thank Alessandro Cocco and Alberto Savino. Their expertise, guidance and dedication were crucial to the success of this work. I am deeply grateful for your insights, feedback and time.